LONG-TIME CONFINEMENT OF TOROIDAL ELECTRON PLASMA IN SMARTEX-C

By

LAVKESH LACHHVANI

PHYS06201404001

Institute for Plasma Research, Gandhinagar

A thesis submitted to the
Board of Studies in Physical Sciences

In partial fulfillment of requirements
for the Degree of

DOCTOR OF PHILOSOPHY

of

HOMI BHABHA NATIONAL INSTITUTE

December 2018

Homi Bhabha National Institute[1]

Recommendations of the Viva Voce Committee

As members of the Viva Voce Committee, we certify that we have read the dissertation prepared by LAVKESH LACHHVANI entitled "Long-Time Confinement of Toroidal Electron Plasma in SMARTEX-C" and recommend that it may be accepted as fulfilling the thesis requirement for the award of Degree of Doctor of Philosophy.

Chairman – Prof. Sudip Sengupta		**Date:** 14/01/2020
Guide/Convener–Prof. Prabal Kumar Chattopadhyay		**Date:** 14/01/2020
Examiner - Prof. Harishankar Ramachandran	R Ramachandran	**Date:** 14/1/2020
Member 1- Prof. Rajaraman Ganesh		**Date:** 14/1/2020
Member 2- Dr. Joydeep Ghosh	Ghosh	**Date:** 14/1/2020
Member 3- Dr Daniel Raju		**Date:** 14/1/2020
Technology Advisor- Dr. Sambaran Pahari		**Date:** 14/01/2020

Final approval and acceptance of this thesis is contingent upon the candidate's submission of the final copies of the thesis to HBNI.

I/We hereby certify that I/we have read this thesis prepared under my/our direction and recommend that it may be accepted as fulfilling the thesis requirement.

Date: 14/01/2020

Place: Gandhinagar

14.01.2020

Signature

Guide

[1] This page is to be included only for final submission after successful completion of viva voce.

Homi Bhabha National Institute

Ph.D. Thesis Evaluation Report

1. **Name of the Constituent Institution:** Institute For Plasma Research
2. **Name of the Student:** Lavkesh T. Lachhvani
3. **Enrolment No.:** PHYS06201404001
4. **Title of the Thesis:** Long-time Confinement of Toroidal Electron Plasma in SMARTEX-C
5. **Name of the Board of Studies:** Physical Sciences

Recommendations

Tick one of the following:

1. The thesis in its present form is commended for the award of the Ph.D. Degree. ✔
2. The thesis is commended for the award of the Ph.D. degree. However, my suggestions for improving the thesis may be considered at the time of the viva voce examination and if the viva voce board deems it appropriate, the same may be incorporated in the thesis based on the discussions during the viva voce examination. The revised thesis need not be sent to me. ☐
3. The thesis should be revised as per the suggestions enclosed. I would like to see the revised thesis incorporating my suggestions before I give further recommendations. ☐
4. The thesis is not acceptable for the award of the Ph.D. degree. ☐

Date: (Signature):

21.03.2019

Thomas Sunn Pedersen

Thomas Sunn Pedersen
Director of Stellarator Edge and Divertor Physics,
Max-Planck Institute for Plasma Physics, and
Professor of Physics, University of Greifswald, Germany

Homi Bhabha National Institute

Ph.D. Thesis Evaluation Report

1. **Name of the Constituent Institution:** Institute For Plasma Research
2. **Name of the Student:** Lavkesh T. Lachhvani
3. **Enrolment No.:** PHYS06201404001
4. **Title of the Thesis:** Long-time Confinement of Toroidal Electron Plasma in SMARTEX-C
5. **Name of the Board of Studies:** Physical Sciences

Recommendations

Tick one of the following:

1. The thesis in its present form is commended for the award of the Ph.D. Degree. [X]
2. The thesis is commended for the award of the Ph.D. degree. However, my suggestions for improving the thesis may be considered at the time of the viva voce examination and if the viva voce board deems it appropriate, the same may be incorporated in the thesis based on the discussions during the viva voce examination. The revised thesis need not be sent to me. [ ]
3. The thesis should be revised as per the suggestions enclosed. I would like to see the revised thesis incorporating my suggestions before I give further recommendations. [ ]
4. The thesis is not acceptable for the award of the Ph.D. degree. [ ]

Date: 8/8/19

H. Ramachandran
(Signature):

HARISHANKAR RAMACHANDRAN
Name of Examiner:
And affiliation IIT Madras

Please give your detailed report in the attached sheet. You may use additional sheets, if required.

Version approved during the meeting of Deans held during 29-30 Nov 2013

Contents

List of Figures

7

Discussion and Future Scope

Experimental study of confinement and transport of electron plasma in tight aspect ratio partial toroidal trap, SMARTEX-C, has been carried out. The prime objective of identifying and removing the road-blocks towards long time confinement has been achieved and confinement time as long as $\sim 100\,\mathrm{s}$ has been obtained. This has allowed us to investigate the existing transport theories. All new and significant results obtained in thesis work are summarized below. Scope of future research work has been outlined and discussed in the following section.

7.1 Summary of Experimental Results

- In order to perform long-time confinement experiments transport driven by electron-neutral collisions should be minimized and hence trap has been upgraded to achieve better vacuum. Base pressure of $6.0 \pm 1.0 \times 10^{-10}$ mbar and operating pressure with filament 'ON' condition, vacuum of the order of $1.5 \pm 0.5 \times 10^{-9}$ mbar has been achieved. This has been achieved by addition of Cryo-pump which helped primarily in removal of water-vapor, Non-Evaporable Getter pump for removal of light gases such as H_2 and He, electro-polishing of the vacuum vessel, controlled baking of vacuum vessel and improving pumping port conductance. Magnetic field plays an important role in the confinement of electron plasma. Magnetic field strength of the system has also been upgraded. SMARTEX-C can be operated in B-field range of 200 Gauss to 1×10^3 Gauss, and pulse duration can be varied from 100 ms to 60 s. Trap components have been re-designed for minimum asymmetries in the mechanical arrangement to minimize the asymmetry induced transport. Spatial resolution of capacitive probes have been enhanced by reducing the size and quantity.

- Simple yet powerful way of interpreting the capacitive probe signal to ascertain the charge cloud dynamics has been developed. Expression for image current for point-like charge cloud making orbital motions has been derived using Green's reciprocation theorem. Numerical computation of signals for point charge trajectory has been carried out. It allows to infer the position of the charge cloud, shape and extent of the trajectory with the aid of capacitive probe signal and experimentally obtained total charge and velocity. Though the technique is presently rather heuristic, this has primarily helped us to establish that the dynamics of the trapped charges akin to an unstable diocotron mode. The technique if suitably extended presents us with an opportunity to investigate the vortex dynamics in SMARTEX-C in a non-destructive way.

- Instabilities are investigated and destabilizing mechanism has been identified in SMARTEX-C. Delineation from resistive wall instability and electron neutral collision driven instability has been carried out by comparing the growth rates. Destabilized electron plasma observed in SMARTEX-C is identified as transient ion resonance instability where ions are continuously formed due to electron impact ionisation and also leave the trap due to axial fields. Characterization of the instability onset time, growth rate, and peak diocotron mode amplitude have revealed many interesting features. Some of these are in good agreement with the theoretical predictions of transient ion resonance instability, while others represent classical ion resonance instability where ions are permanently trapped. Complete control over the observed instability has been achieved by tweaking the governing parameters and a very quiescent electron plasma in equilibrium has been obtained.

- To diagnose the quiescent electron plasma, externally launched diocotron waves have been used as a diagnostic tool. Capacitive probes are used as the launch electrodes and linear $m = 1$ mode is launched. As the linear $m = 1$ diocotron mode frequency is proportional to electron plasma density, the launched diocotron mode frequency gives the density of electron plasma. Technique has been perfected such that only small amplitude linear diocotron oscillations are launched. Launching of diocotron modes at different time instances give the temporal evolution of electron plasma density and this has been used to obtained the confinement time.

- Achievement of quiescent electron plasma at equilibrium has led towards the long-time confinement and provides an opportunity to investigate the transport properties of the electron plasma in the partial toroidal trap. Temporal evolution of electron plasma density is obtained using diocotron launch technique and time required to reach the $1/e^{th}$ of the initial electron plasma density is defined as confinement time. Confinement time has been scaled with magnetic field and is observed to be independent of B field.

- Observed confinement time has been compared with loss rate due to magnetic pumping transport for toroidal electron plasma. It may be noted that existing theory is applicable for large aspect ratio geometries. The theory of magnetic pumping transport has been generalised for arbitrary aspect ratio torus and new results predict even lower confinement time of electron plasma in SMARTEX-C (for an assumed temperature of 1 eV). Observed confinement time exceeds this theoretically predicted confinement time. In other words, present experimental results on confinement suggests that MPT does not really define the theoretical limit for confinement at least in partial toroidal traps.

7.2 Future Scope of Work

- Temperature Diagnostics : Plasma density and temperature are the fundamental parameters of any plasma that are necessary to characterize the plasma and also govern the collective properties. It is firmly believed that electrostatic potential energy is the dominant energy component in NNP and consequently kinetic energy of the plasma would be fairly low implying T_e to be few eV. Temperature diagnostics with good accuracy is very crucial in accurately defining the theoretical limit of confinement time and confirm the role of temperature in MPT and also for validation of the transport theory. Measurement of temperature $T_{\parallel}$ and $T_{\perp}$ will also establish the fact whether well trapped toroidal electron plasmas can approach thermal equilibrium like their cylindrical counterparts.

- Charge density profile measurement: To firmly establish the transport mechanism of partial toroidal trap like SMARTEX-C, it is important to obtain the temporal evolution of spatial density profile. One can design the vertical strips of charge collector or 2-D charge collector assembly behind the collector grid to obtain the line integrated radial density profile by dumping the charge cloud on these strips. The major concern could be the signal to noise ratio of the diagnostics as the total charge itself being very tenuous. Charge integrating capacitor or use of I to V converter with very high gain at high bandwidth might be a solution worth attempting. Imaging of entire poloidal cross-section of the trap with the help of phosphor screen aided by a Micro Channel Plate (MCP) would be the ideal solution, but it requires a careful design and suitable choice of phosphor material.

- Investigation of charge cloud/vortex dynamics: As discussed in Chapter 4, the single point-charge cloud trajectory is unable to explain the data from multiple capacitive probe. The amplitude as well as phase information for initial turbulent phase is left unexplained. This has been intuitively solved by taking two point charges and signatures consistent with multiple capacitive probes have been obtained. The analysis therefore needs to be extended to complex charge configurations. Further, including data from all the probes in our analysis can be of help to infer the complete dynamics and shall be validated in future using phosphor screen based imaging diagnostics. Formation of single vortex from hollow circular charge profile through turbulent inverse cascade is an interesting phenomena and can be understood using imaging diagnostics.

- Detailed characterization of Ion Resonance Instability : Clear signatures and trends of ion-resonance instabilities are observed and it has been shown in the Chapter 5 that the normalized peak growth rates follow the trend of transient ion resonance instability with many of the observed features in good agreement with theory. Some of the observed features (finite onset-time of instability) though are in agreement with that of classical ion-resonance instability. A threshold ion density appears to trigger the instability in accordance with the classical theory of ion-resonance. However, measurement of ion current (the ions leaving along the magnetic field to collector grid) shall confirm the amount of trapped/untrapped ions and define the threshold. Direct estimation of displacement 'D' either from capacitive probe data or from destructive charge collection diagnostics shall confirm the kind of growth of the instability (exponential/linear). Temperature diagnostics shall help in determining the electron impact ionization cross section with accuracy and identify whether temperature remains constant as pressure is varied and growth rates are estimated. Peak growth rate and its dependency on temperature, broadness of the resonance curve (Q-factor) with B-field are some of the important features that shall be further investigated.

- Toroidal arc length variation : It has been experimentally observed that partial toroidal traps are able to trap electron plasmas for confinement times longer than the ones predicted by magnetic pumping transport theory. Can the violation of theoretical prediction be due to the 'partial' nature of the trap? End grids can introduce the asymmetric electric fields at the edges and oscillate the electron plasma length. The length of the flux tube may also change significantly during poloidal rotation due to the small aspect ratio. All of this may trigger the rotational pumping transport. To establish the effect of end grids and confirm with the theory one can change the coarseness of the end grids or change the grid to rectangular hollow electrode and compare the observed confinement time with theory. In addition to this, to investigate the role of rotational pumping transport and observe the plasma length effects on confinement time, toroidal arc length can be varied and scaling of confinement time with toroidal arc length should be investigated. Experiments of confinement in full-torus with retractable filament shall also be of interest to investigate the MPT theory in full torus and role of trapped ions in complete torus on confinement of electron plasma.

- Aspect ratio variation : It is a well known fact that, cylindrical traps can confine the electron plasma for very long confinement time extending up to few days. To connect the physics of toroidal electron plasma to that of cylindrical trap, one can vary the aspect ratio of the trap by incrementally increasing the radius of inner-wall (or, alternately reducing the radius of outer-wall).

Thesis Summary

Name of the Student: Lavkesh T. Lachhvani

Name of the CI/OCC: Institute for Plasma Research **Enrolment No.: PHYS06201404001**

Thesis Title: Long-time Confinement of Toroidal Electron Plasma in SMARTEX-C

Discipline: Physical Sciences **Sub-Area of Discipline:** Plasma Physics

Date of viva voce: 14/01/2020

Nearly 100 sec confinement of electron plasma in a tight aspect ratio partial torus with a purely toroidal magnetic field is reported in this PhD thesis. This is nearly two orders higher than previously reported confinement time in similar devices elsewhere. Moreover, weak dependence of confinement on magnetic field, a distinguishing feature of Magnetic Pumping Transport, proposed theoretically is shown experimentally for the first time.

So far, it has been well-known that single component plasmas (a collection of pure electrons or ions), can simultaneously remain well-confined and be in thermodynamic equilibrium when trapped with a homogenous B field. Precise manipulation, control and reproducible experiments were therefore possible in linear traps which made such plasmas a potent tool for investigating a large number of basic phenomena, impacting a diverse range of fields such as fluid dynamics, condensed matter, astrophysics, atomic physics and antimatter-physics.

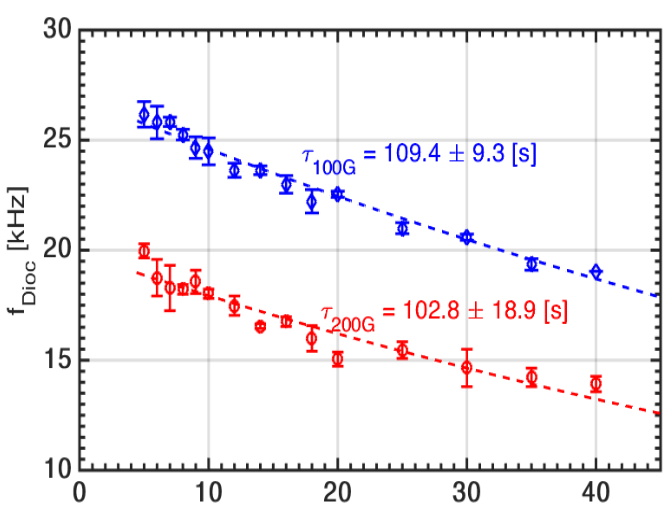

Figure 1 Observed diocotron mode frequency on capacitive probe along with exponential fit showing confinement time of 100 ± 10 s for low magnetic fields of 100 and 200 Gauss, at low pressure of 5.0 x 10^{-9} ± 1.0 x 10^{-9} mbar and injection energy VInj = 250 V.

Even though equilibrium and stability of charged clouds are theoretically ensured with a purely toroidal B field, confinement has remained, notoriously elusive. All efforts so far to tame a cloud of electrons in such traps, had resulted in a maximum life-time of 1-3 seconds. The challenges can be gauged from the fact that the last result was reported almost a decade ago. The biggest impediment, as has been suggested, is the magnetic pumping transport that is unavoidable due to the inhomogeneity in B field, though direct evidence of such transport had never been reported. In this context, the unprecedented confinement along with unmistakable evidence of magnetic pumping transport reported in this letter leads to interesting comparisons with existing transport theory and lifetime predicted thereof.

Such plasma in a tight aspect ratio device can become a test-bed for many fundamental studies such as, hydrodynamic behavior with compressible effects, transport of charged particles under arbitrary degree of neutrality in toroidal geometry (relevant to fusion community), formation of electron-positron pair plasmas of relevance to astrophysical community.

1

Introduction

1.1 What is Non-Neutral Plasma(NNP)?

Non-Neutral Plasmas (NNP) is a collection of charged particles of single species [1]. In contrast to conventional quasi-neutral plasmas [2] which are characterized by $\frac{e\Phi}{T} \sim 1$, NNP owing to its non-neutrality are characterized by the large $\frac{e\Phi}{T} >> 1$. This property sets them apart from quasi-neutral plasmas. In other words, compared to quasi neutral plasmas, non-neutral plasmas possess very large electrostatic potential energy in units of thermal energy. Examples of such plasmas that have been realised in experiments are electron plasmas [3], ion plasmas [4], positron plasmas [5] and anti-proton plasmas [6]. NNP is much easier to confine for very long times in a simple cylindrical apparatus by means of static electric and magnetic fields. Uniform magnetic field (B) along the axis of azimuthally symmetric cylindrical electrodes provide radial confinement: the self electric field (E) of the un-neutralised charge cloud immersed in the axial uniform B gives it an azimuthal $E \times B$ drift resulting in a dynamic force equilibrium. Appropriate potentials on concentric end-electrodes confine the plasma along the z-axis of the cylindrical trap [3]. Confinement is assured by conservation of canonical angular momentum [7]. Confinement of electron plasmas in cylindrical Penning-Malmberg (P-M) traps have been observed for few days [8–10]. The limit on the confinement time comes from external torque provided through mechanisms such as finite-wall resistance [11], electron-neutral collisions [8] or static asymmetries in the trap fields [9, 12–14]. Such asymmetry arises due to errors in fabrication of electrodes or misalignment of the magnetic field axis with the trap geometrical axis. In principle, plasmas with single sign of charge can be confined forever [15] with rotating wall technique [16], where dissipated torque is balanced by external means.

Another important property distinguishing NNPs is that these plasmas can come to state of thermal equilibrium while they are confined [1,17] through electron-electron collisions [18]. Quasi-neutral plasmas can not be confined by static electric and magnetic fields and also be in a global thermal equilibrium (they can be in local thermal equilibrium only). When quasi-neutral plasma is confined there is always free energy, and these sources of free energy tend to drive instabilities. That is why the confinement of neutral plasmas is notoriously difficult [19]. In contrast, a plasma with a single sign of charge that is confined in a state of thermal equilibrium has no free energy and is guaranteed to be stable and quiescent in the absence of any external dissipation. Such excellent confinement properties of NNP allow controlled and reproducible experiments. In-depth understanding has been developed by carrying out investigations on equilibrium [1], stability [20–22], transport [23, 24], waves [25, 26] observed in NNP. This has allowed a wide range of basic plasma physics studies [27] as well as applications of it [28, 29] in many areas of physics. Some of the many basic plasma physics phenomena investigated include 2-D vortex dynamics of incompressible fuids [30–33], cryogenic transition to Coulomb crystals [34], frequency standards [35], and on application front like positron and anti-proton traps for formation of anti-Hydrogen atoms [36], Free Electron Lasers (FEL), high power microwaves [37] and atomic and molecular physics [38] to name a few.

1.2 Why Study Toroidal NNP?

The excellent confinement of electron plasmas in cylindrical traps and the rich collective effects naturally fuel investigation into confinement of such single species plasmas in other geometries and magnetic field topologies. Once again, it is curiosity driven basic research that has been primarily pushing the frontiers of research into toroidal electron plasmas. Confinement of non-neutral plasma in toroidal geometry and investigating the effects of arbitrary degree of non-neutrality under controlled conditions [39], for example, can aid understanding of transport in neutral plasmas which is of profound interest to the fusion community. In recent times, creation of electron-positron pair plasma has been of immense interest [40,41] and toroidal traps appear to be the best candidate as it does not require any end potentials. The physics of a magnetized pair plasma is yet to be investigated experimentally. In addition to this, just like cylindrical electron plasmas in homogeneous magnetic field has served as excellent test-beds for carrying out incompressible fluid dynamics experiments [30,32], toroidal electron plasma in the presence of an in-homogeneous magnetic field may mimic compressible fluids and has remained an attractive proposition [42] for some time, that merits further investigation. Historically, several applications of toroidal electron plasmas were also proposed. For example, formation of a deep potential well by an electron cloud trapped in toroidal geometry was viewed as a source of highly stripped ions [43], heavy ion particle accelerator [44], electrostatic thermonuclear fusion reactor [45,46], or as a shielding mechanism for space vehicles from solar radiation [47].

Toroidal traps offer the challenges of ∇B and curvature drift coming naturally due to toroidicity and provides the opportunity to understand the toroidal effects on the equilibrium [48], stability [49], dynamics, confinement and related transport of NNP. Experiments of non-neutral plasma in purely toroidal magnetic field [50] had established the existence of toroidal equilibrium and proved that curvature and ∇B drift to be unimportant. Yet, stability of the equilibrium was overwhelmed mostly by non-toroidal effects arising from build-up of ions driving the ion resonance instability [51] and the confinement of the plasma was mostly limited to [50, 52, 53] few hundreds of microseconds. It may be noted here that electron plasma experiments conducted in toroidal geometries were mostly carried out in large aspect ratio traps. To study the effect of strong toroidicity, theoretical and experimental investigations of electron plasmas in a tight(small) aspect ratio trap (fat torus), SMARTEX(SMall Aspect Ratio Toroidal Electron plasma eXperiment) were initiated at Institute for Plasma Research in $\sim$ 1990. A small aspect ratio trap having purely toroidal magnetic field was developed and successful operation of the trap was established. These experiments were carried out in full torus and cross-field injection techniques were implemented. Potential contours using Langmuir probe in high impedance mode were obtained demonstrating the existence of equilibrium [54, 55]. The equilibrium was observed to be shifted inwards as predicted by theory [56]. Effect of external radial electr field on electron plasma was investigated [57, 58]. Confinement times of the order of few 100 μs was observed. Poor confinement was attributed to insufficient electron injection, and/or presence of ions leading to ion-driven instabilities.

The minimum underlying requirement for investigation of basic plasma phenomena or applications based on toroidal non-neutral plasmas, is an excellent confinement of NNP in toroidal geometries for very long-times. Even though investigations of electron plasmas in toroidal geometry (with purely toroidal B-field [48,50]) chronologically precede cylindrical traps, the toroidal traps have been plagued with poor confinement properties [50,55,57]. This is in contrast to what is observed in cylindrical traps and has been a bane and a major impediment towards achieving the stated objectives. It is therefore important to debate what has limited the confinement is such traps.

Purely toroidal magnetic field configuration even while in stable toroidal equilibrium, is theoretically predicted to have limited confinement properties due to magnetic pumping transport (MPT) (although direct evidence of MPT is yet to be reported). Proposed by O'Neil and Crook [59], MPT arises due to $E \times B$ drifts of the plasma in a spatially in-homogeneous toroidal magnetic field. As the electrons transit from the inboard (high field) to outboard (low field), adiabatic in-variance of single particle magnetic moment ($\mu = m{v_\perp}^2/2$) and angular momentum ($J_\parallel = mv_\parallel r$) lead to fluctuations in the particle kinetic energy. Due to unequal variations in $\tilde{v}_\perp$ and $\tilde{v}_\parallel$, the parallel temperature increases more than the perpendicular temperature. As these equilibrate through electron-electron collisions, net heating of the plasma occurs at the expense of electrostatic potential energy. The latter implies expansion of the plasma. The resulting radial transport is assumed to fundamentally limit the confinement in purely toroidal magnetic field configuration. A dimensional analysis of flux rate carried out [60] gives the transport time scale to be dependent on the major radius R_0 of the trap and plasma temperature T_e as $\tau_{mp} = 0.02R_0(cm)^2\sqrt{T_e(eV)}$. Till early 2006, the best confinement times reported from toroidal traps were orders of magnitude less than those predicted by magnetic pumping transport theory.

Major breakthrough was achieved with the partial toroidal traps (or "C" shaped traps) developed in the last decade or so. Combining the trapping techniques of cylindrical traps with that of toroidal geometry have led to successful trapping. In a partial toroidal trap the toroidal symmetry is broken, the Penning-Malmberg trap arrangement of cylindrical geometry is implemented in toroidal geometry. The successful implementation of the concept was demonstrated by Stoneking et al [61] at Lawrence University(LU) in large aspect ratio torus with the aid of radial electric field. Initial results of electron plasma in LNT-I demonstrated the confinement to be 18 ms and was stated to be limited due to the presence of ions [62]. In late 90's, the SMARTEX trap was converted to a C-shaped trap (SMARTEX-C) and concept of the partial toroidal electron plasma was introduced by Pahari et al [63]. This allowed a breakthrough and successful confinement of electrons for several milliseconds (extending for the entire duration of the pulsed toroidal B-field) were reported from SMARTEX-C [63]. Confinement was achieved without any aid of the radial electric field unlike in large aspect ratio torus. Electron injection along the magnetic field lines helped to build sufficient density in plasma to make $E \times B$ rotations and provide necessary rotational transform to sustain the plasmas for longer times. Rich electrostatic activities were monitored and observation of a $k_\perp$ mode was also reported. The mode appeared analogous to $m = 1$ diocotron mode in cylindrical machines but was seen to grow in amplitude with appearance of higher harmonics. Energy shifted predominantly to $m = 2$ harmonic suggesting a shaping of the cloud. Plasma was believed to be destabilized due to the presence of ions right from the birth of it. Instability was growing rapidly, saturating and decaying leading to the loss of electron plasma. In spite of its success, an accurate estimate of the confinement time in SMARTEX-C was challenged due to the pulsed nature of B field along with presence of instabilities.

Interestingly, around the same time, upgraded trap LNT-II with stronger magnetic field, Ultra-High Vacuum of $\sim 5 \times 10^{-9}$ mbar and reduced fabrication error reported excellent improvement in confinement time – from several milliseconds [62] to few seconds [64]. While this was less than the limit posed by MPT theory it was of the same order of magnitude. At this point it was perhaps reasonable to assume that toroidal traps were nearing the limits proposed by transport theories. It is in this perspective that the proposed work in this thesis assumes importance.

1.2.1 Toroidal NNP in different magnetic topologies

An interesting aside but not entirely irrelevant to the context of this thesis is perhaps the fact that apart from purely toroidal magnetic field configuration of closed field lines, electron plasmas in other B-field configurations have also been explored in recent times. These include magnetic surfaces in stellerator i.e. Columbia Non-Neutral Torus (CNT) [65] and Compact Helical Stellerator (CHS) [66] and in levitated dipole magnetic field of magnetospheric like configuration in the Ring Trap -1 (RT-1) [67]. Confinement of electron plasma in stellarator was observed to be of the order of $\sim 100\,\mathrm{ms}$ in CNT [68] limited, once again, due to the presence of ion-driven instabilities in the device. Magnetospheric like configuration (levitated dipole magnet) in RT-1 had confined electron plasma exceeding $300\,\mathrm{s}$ [67,69]. Here too, sudden appearance of rapidly growing ion-driven instability is believed to be destroying the confinement in RT-1.

These promising results along with partial success in SMARTEX-C and long-confinement achieved in LNT-II, together have led to a renewed interest in the toroidal electron plasmas and largely defined the scope of the thesis.

1.3 Motivation & Scope of Thesis

The scope of the present thesis is to take ahead the experiments in SMARTEX-C and work towards improving the confinement time. With its small aspect ratio, toroidal effects are expected to be pronounced in SMARTEX-C, and the trap, we believe, is uniquely poised to investigate the effects of strong toroidicity on confinement and transport. While earlier work in SMARTEX-C had demonstrated the possibility of long time confinement, several bottlenecks had to be removed. It essentially meant the trap had to be upgraded in several respects, namely, the vacuum conditions had to be improved and strength and duration of the toroidal magnetic field had to be increased. The diagnostics and data-acquisition and control had to be addressed too to keep up with the demands of a long-time confinement. Next, the capacitive probe diagnostics had to be interpreted with much more certainty so that the dynamics of the plasma could be well understood. This was achieved by numerically solving for image current on the probes due to an oscillating trapped charged particle and heuristically comparing it with the observed probe data. Having understood the evolution of the charge cloud dynamics in stable and unstable regimes it was possible to zero in on the possible dynamics, namely, the instability responsible for loss of confinement. It was then required to identify the parameter regime where instabilities could be controlled. A stable, quiescent plasma, with no perceptible electrostatic activity that could be detected by the capacitive probes, was bound to be challenged with regards to its diagnostic. So externally launched modes had to be developed and perfected as diagnostics. With steady state confinement and well-diagnosed plasma it was possible to push the limits of confinement. It was also possible to investigate and compare the confinement times vis-a-vis those prescribed by the existing transport theories. The thesis comprises of all these efforts and results.

Thesis is organized as follows: Chapter 1 introduces the NNP and the importance of research to understand the physics of transport/confinement in non-neutral as well as neutral plasmas. Relevance of toroidal electron plasmas, the importance of confinement and transport mechanisms that limit the confinement are discussed and motivation behind the present thesis work is presented.

Chapter 2 discusses the theoretical background of cylindrical NNP, its equilibrium, stability and transport. Diocotron mode, its frequency dependency on the charge content, length of the plasma and correction due to non-linear effects are also reviewed. As the diocotron mode is a negative-energy mode, destabilizing mechanisms (collisional and non-collisional dissipative processes) and corresponding theoretical growth rates are discussed. Experimental results supporting the theoretical developments as reported in the literature have been reviewed wherever necessary. Various possible transports, due to internal mechanisms and external forces are discussed. Next, literature review has been carried out in the context of toroidal electron plasmas. Theoretical development of the physics of toroidal electron plasmas, namely, its equilibrium, stability and transport is presented followed by experimental observations as reported in various magnetic topologies. Observed confinement times in these geometries and their possible explanations are discussed particularly in the perspective of present thesis work.

Chapter 3 describes the existing experimental system and the upgrades carried out to achieve our stated objective of long-time confinement. Magnetic field strength of 9×10^2 Gauss having pulse length of 2.5 s with High Current DC Power Supply and operating pressure of $1.5 \pm 0.5 \times 10^{-9}$ mbar are some of the noteworthy achievements. Up-gradation of capacitive probe diagnostics for improved spatial resolution of the observed mode, reproducible total charge measurements through dump-diagnostics, and development of externally launched diocotron modes to obtain the confinement time are significant diagnostic developments. In addition, FPGA based trigger-control system for trap operation and high speed multi-channel (24 nos) PXI based data acquisition system(with optimized bandwidth and record length) were integrated. All of these proved extremely helpful in carrying out and analyzing data from confinement experiments that extended for several ten's of seconds.

Chapter 4 explores the dynamics of electron plasma in SMARTEX-C using capacitive probe data. Capacitive probe diagnostics is non-invasive and due to its well-developed theory for cylindrical traps, plays an important role in diagnosing the dynamics of single species plasmas. To aid our interpretation of capacitive probe data for toroidal electron plasmas we extended the analytical tool developed by Kapentanako's et al [70]. An expression for image current was obtained for our geometry and numerically solved for various electron charge cloud trajectories. A heuristic approach was adopted and the results from numerical exercise were correlated with experimental data to suggest possible charge cloud dynamics during the stable and unstable regime. It primarily confirmed the presence of an unstable diocotron mode in SMARTEX-C that led to loss of confinement. Model was further extended to interpret data from multiple capacitive probes hinting at presence and merger of multiple vortices, at least during the initial phase of evolution. All of these suggested an interesting and hitherto unexplored regime of vortex dynamics in toroidal geometries (i.e. in the presence of in-homogeneous B field).

Chapter 5 presents our investigations into possible reasons of instability and rules out the role of neutrals and resistive-wall in energy dissipation that may drive the growth of instability. Rather, presence of ions is found to be an important destabilizing factor. Scaling of the growth rate with pressure, magnetic field and different gases confirmed that resonance with ions trapped in the electron potential well is the primary mechanism that drives the diocotron mode unstable. The scaling also suggested means to arrest the growth of instability and helped us to obtain the operating parameter regime where quiescent electron plasma can be obtained in SMARTEX-C. Observed growth rates match with those suggested by transient ion resonance instability, a distinct possibility in a partial torus with end-potentials.

Chapter 6 presents the detailed results of experiments to achieve long-time confinement of toroidal electron plasma in SMARTEX-C following the mitigation of instabilities. Confinement time in all such cases is obtained by externally launching the diocotron mode in the trapped plasma and relating the observed frequency evolution of small amplitude diocotron oscillations to the evolution of stored charge. Multiple inject-hold-launch cycles were carried out to ascertain the time evolution of density. Experiments suggested an exponential decay of the plasma with 1/e decay time extending to as much as $\sim 100\,\mathrm{s}$ (at 2×10^2 Gauss at an operating pressure of $1.5 \pm 0.5 \times 10^{-9}\,\mathrm{mbar}$). Controlled experiments in such a steady state, well-confined plasma also gave us the opportunity to test one of the well-known transport theory proposed by O'Neil and Crook [59] that gives theoretical estimates of flux loss due to rotation of flux tubes in an in-homogeneous magnetic field. Since the theoretical estimates were proposed for a large aspect ratio trap, we found it pertinent to re-derive and generalise it for an arbitrary aspect ratio and compare the relevant time scales with those observed in SMARTEX-C. Experimental results depart from Magnetic Pumping Transport theory (MPT) in one respect. The observed confinement exceeds time-scales suggested by MPT by one and half order of magnitude, for assumed electron temperature of $1\,\mathrm{eV}$. Interestingly, the observed transport is independent of magnetic field which is a distinguishing feature of MPT. Although accurate temperature measurements are awaited, a rough estimate has been obtained experimentally and it is also argued that the temperature of $1\,\mathrm{eV}$ is a reasonable estimate. The result assumes significance since MPT was presumed to limit the confinement in toroidal devices and therefore opens up a new area that merits further theoretical and experimental investigation.

Chapter 7 finally concludes the thesis with a summary of important results and discussion on the scope of future work.

2

Non-Neutral Plasma - Background

This chapter reviews the theoretical and experimental investigations of NNP in cylindrical and toroidal traps in the context of the present thesis work. Theoretical background to NNP is provided in introductory section which includes the equilibrium, stability and confinement properties of these plasmas in cylindrical trap geometry and supporting experimental evidences and results. In the following section, physics of the stable diocotron mode is discussed and its stability properties are investigated in the presence of resistive boundary, background neutrals and oppositely charged ions. The next section discusses the theoretical framework of toroidal NNP and experimental efforts in toroidal traps with different magnetic field configurations.

2.1 Brief Review of Theory and Experiments of NNP in Cylindrical Traps

2.1.1 Equilibrium

Using cylindrical co-ordinates (r, θ, z), we first consider the simplest example of NNP. It is an infinitely long, constant density cylindrical column of electrons immersed in an uniform axial magnetic field $B^{ext} = B_0\hat{z}$ (Figure 2.1). It is assumed that there no ions are present, there is no drift along the magnetic field, plasma is cold $T = 0$, and diamagnetic effects are negligible. The equilibrium of the system can be examined by the equation of motion of charged particles in steady electric and axial magnetic field. Mutual repulsion of the same sign charged particles would give a repulsive electric (Coulomb) force that would expand the charge cloud continuously in the r direction. This self electric field and externally applied uniform magnetic field would cause an $E \times B$ drift that would impart the cloud with an azimuthal velocity $v_{e\theta}$. This azimuthal rotation will provide a centrifugal force which would add to the electrostatic repulsive force. However, $v_{e\theta}$ would also cause a radially inward magnetic force ($v_{e\theta} \times B$). All the forces acting upon electron are shown in Figure 2.2.

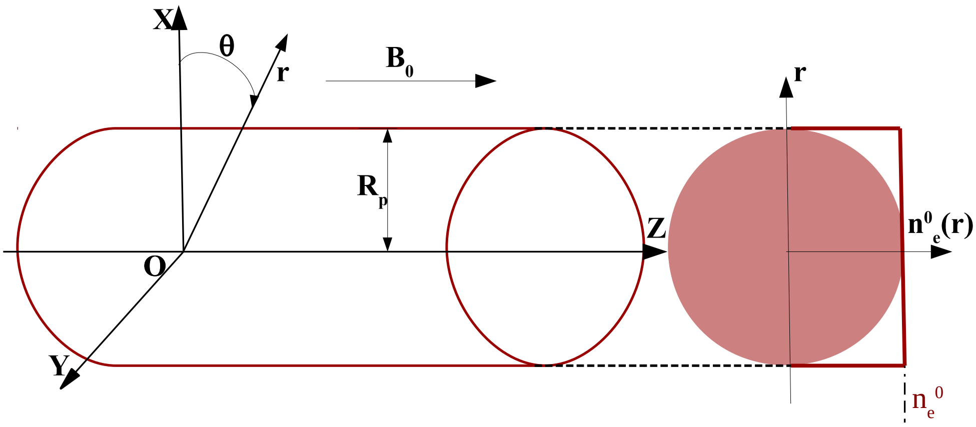

Figure 2.1: Constant density electron column immersed in uniform axial B-field.

The radial force balance equation for an electron in a circular orbit in steady state will be given by:

$$\frac{-m_e v_{e\theta}^2}{r} = -eE_r^o - ev_{e\theta}^o B_0 \tag{2.1}$$

where $v_{e\theta}{}^o$ is the azimuthal velocity of an electron, E_r^o is the equilibrium radial electric field, m_e and $-e$ are electron mass and charge. The radial electric field is given by Poission's equation:

$$\frac{1}{r}\frac{\partial}{\partial r} r E_r^0 = -\frac{en_e^o(r)}{\epsilon_0} \tag{2.2}$$

For constant density profile, Poisson's equation can be integrated to obtain the $E_r^o = -\frac{ren_e^o}{2\epsilon_0}$ for $0 < r < R_p$, which can also be represented as $E_r^o = -\frac{m_e}{2e}\omega_{pe}^2 r$, where $\omega_{pe}^2 = \frac{n_e e^2}{m\epsilon_0}$. We can use electron cyclotron frequency $\omega_{ce} = \frac{eB}{m_e}$ and angular rotation frequency defined as $\omega_e = \frac{v_{e\theta}^o}{r}$ along with Equation 2.2 to rewrite Equation 2.1 as follows:

$$-\omega_e^2 = \frac{\omega_{pe}^2}{2} - \omega_e \omega_{ce} \tag{2.3}$$

The solutions of this quadratic equation 2.3 are as follows:

$$\omega_e^{\pm} = \frac{-\omega_{ce} \pm \sqrt[2]{\omega_{ce}^2 - 2\omega_{pe}^2}}{2} \tag{2.4}$$

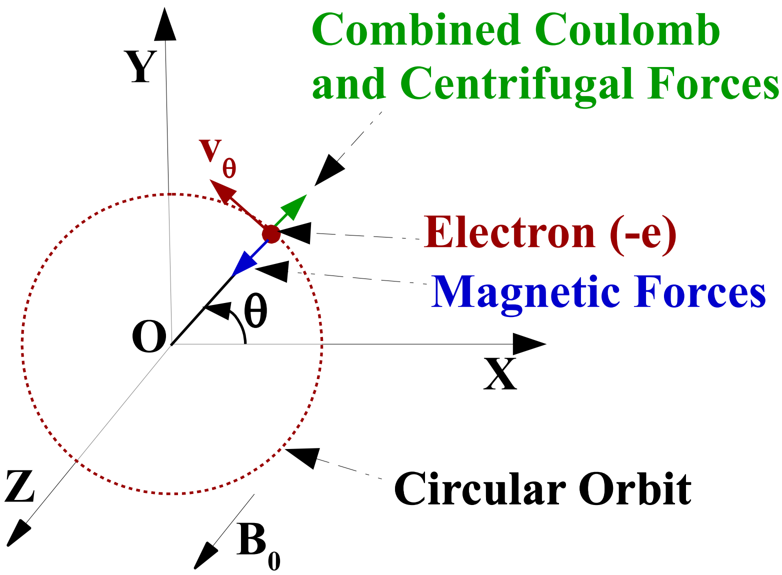

Figure 2.2: Radial force balance for an electron making circular orbit,. The outward radial forces (Coulomb and centrifugal) are being balanced by inward Lorentz force.

Existence of two equilibrium rotation frequency is not surprising. If the plasma column were electrically neutral, then $E_r^0 = 0$ and the equilibrium rotation frequencies would be $\omega^- = 0$ or $\omega^+ = \omega_{ce}$, which corresponds to electrons at rest or electrons gyrating around the axis of symmetry at cyclotron frequency. One shall note that ω_e is independent of r and thus cloud rotates as rigid rotor which is resulting as a special case of uniform density profile. Solutions of slow and fast rotation frequencies are plotted as a function of ratio $\frac{\omega_{pe}^2}{\omega_{ce}^2}$ as shown in Figure 2.3. The maximum value of $\frac{\omega_{pe}^2}{\omega_{ce}^2}$, also known as the self-field parameter q, is 1. Since ω_{pe} is $\propto$ density (n) and ω_{ce} is $\propto$ magnetic field (B), it is implied that for a certain B, the density cannot exceed beyond a certain n such that the 'defocussing force' always remains less than the 'focussing force'. This limit is also known as the 'Brillouin density limit'. The ratio $q = \frac{\omega_{pe}^2}{\omega_{ce}^2}$ is generally small and follows that electron motion is generally a balance between the electric and magnetic forces, and inertial forces are negligible. In other words, it is a ratio of ''gyroradius' to the scale size of electric field and is a rough measure of the 'adiabaticity' of the system. From a theoretical standpoint it makes the guiding center approximation valid. Electron plasma as a whole drifts in the azimuthal direction with a drift velocity $v_{e\theta} = E \times B/B^2$ in the guiding center approximation.

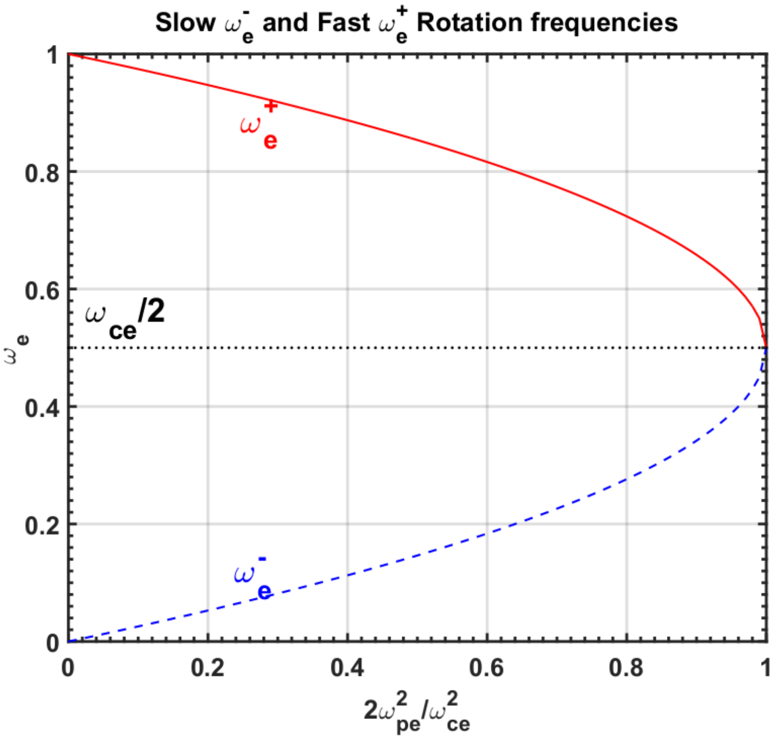

Figure 2.3: Allowed slow ω_e^- and fast ω_e^+ rotation frequencies of NNP.

It describes an incompressible flow and when used in continuity equation

$$\frac{\partial n}{\partial t} + \vec{v} \cdot \nabla n + n \nabla \cdot \vec{v} = 0 \tag{2.5}$$

where, $\Delta \cdot \vec{v} = 0$ term vanishes due to incompressibility, density is seen to evolve with time due to convection only.

$$\frac{\partial n}{\partial t} = \frac{-E \times B}{B^2} \cdot \nabla n \tag{2.6}$$
$$\frac{\partial n}{\partial t} = \frac{\nabla \Phi \times B}{B^2} \cdot \nabla n \tag{2.7}$$

where, Φ is electrostatic potential. Thus potential and density are coupled to each other and to solve for these we invoke the Poisson's equation:

$$\nabla^2 \Phi = -\frac{ne}{\epsilon_0} \tag{2.8}$$

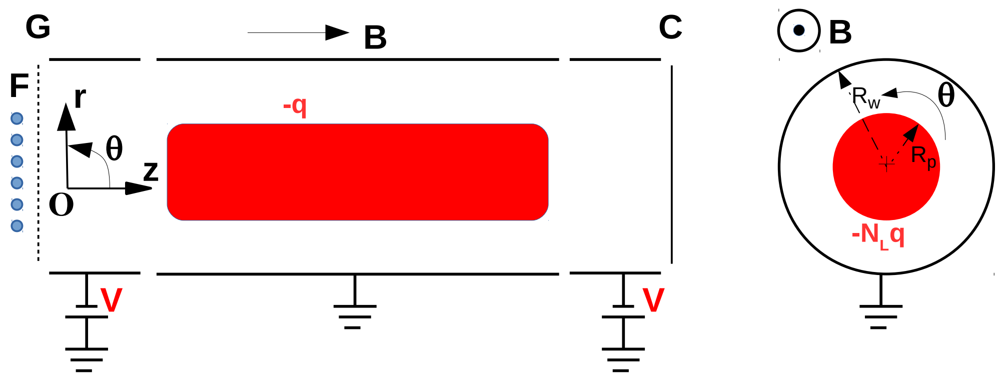

Figure 2.4: Schematic arrangement of electrodes in cylindrical Penning-Malmberg trap. F-Filament, G-Grid, C-Collector

These equations being mass independent, low frequency dynamics can be described by the coupled Equations 2.6 and 2.8. It describes the dynamics of massless, incompressible fluid governed by combination of $E \times B$ drifts and Poisson's equation. Experimentally one can produce such plasmas in cylindrical geometry popularly known as 'Penning-Malmberg' trap. Design and arrangement of the electrodes is shown in Figure 2.4. Thermionic source(F) of electrons is used to fill the trap by pulsed injection through grid (G) and electric and magnetic fields are used to confine them. End electrodes biased at $-V$ potential provide the axial confinement to the electrons and axial magnetic field provides the radial confinement. Collector (C) is used to measure the total number of charges at any instant of time by dumping them. Investigation of properties of pure electron plasma in cylindrical trap were carried out for the first time by Malmberg et al [3] in 1975.

2.1.2 Confinement Theorem

Most interesting feature of the NNP is that, e-e collisions do not degrade the confinement as long as symmetry of the experiment is maintained [7]. Like particle collisions in the pure electron plasma trap do not cause any transport of the plasma out of the trap. Total energy of the system remains invariant in time as well as with axis of symmetry. This implies that, total Hamiltonian of the system H follows the relations:

$$\frac{\partial H}{\partial t} = 0 \tag{2.9}$$

$$\frac{\partial H}{\partial \theta} = 0 \tag{2.10}$$

Equation 2.10 suggests that canonical angular momentum of the system remains conserved. One can write out the canonical angular momentum of the i^{th} particle as,

$$P_{\theta i} = m r_i v_{\theta i} + e r_i A_{\theta i} \tag{2.11}$$

Any collision between two like particles will conserve the total angular momentum of the two particles and so the total angular momentum of all the particles will remain constant even if there are electron-electron collisions. Total canonical angular momentum of all the particles can be written as follows:

$$\sum_{i=1}^{N} P_{\theta i} = \sum_{i=1}^{N} (m r_i v_{\theta i} + e r_i A_{\theta i}) = const. \tag{2.12}$$

where, $A_{\theta i}$ is the vector potential corresponding to the externally applied magnetic field $B_0 \hat{z}$. Vector potential $A = Br/2\hat{\theta}$ in cylindrical geometry. If magnetic field is sufficiently strong, contribution of mechanical part of canonical angular momentum can be ignored. Thus conservation of canonical angular momentum simply reduces to

$$P_\theta = \sum_{i=1}^{N} P_{\theta i} \simeq \frac{eB}{2} \sum_{i=1}^{N} r_i^2 = const. \tag{2.13}$$

This equation 2.13 constrains the radial positions of the electrons. Hence, inter-particle collisions do not drive the plasma towards the wall and so the electron plasma is perfectly confined as long as the axisymmetry is maintained [71]. One can now compare with conventional neutral plasma, where radial particle transport towards the wall is driven by collisions between ions and electrons. Momentum exchange rate between unlike species is determined by electron-ion collision frequency ν_{ei} and the difference between electron and ion velocity. If only one species exist, it is impossible for momentum to be exchanged between unlike species. This theoretical fact has also been observed experimentally by Malmberg et al [8, 72] at UCSD, where confinement time of the order of many hours/weeks is routinely observed. It has also been observed experimentally that electron-electron collisions drive electron plasma towards thermal equilibrium [18] and thus NNP confined in cylindrical traps can simultaneously remain confined and be in thermal equilibrium.

2.1.3 Diocotron Modes

Low frequency linear waves supported by trapped charged particles in Penning trap named 'Diocotron waves' (diocotron means 'to chase' in Greek) were first observed experimentally with hollow electron beam inside a conducting cylinder. The hollow beam of charged particles propagating in a wave-guide along the magnetic field is unstable and breaks into small pieces and these pieces are 'chasing each other' due to shear in the angular flow velocity and thus it was named as 'Diocotron instability'. One can assume infintely long plasma column described by a 2-D model. Density perturbations in general has the form $\delta n = \delta n(r) \exp i(m_\theta \theta + k_z z - \omega t)$; we describe $m = 1$ and $k_z = 0$ mode only. In its simplest form, as seen in cylindrical machines, the small amplitude (linear) $m = 1$ diocotron mode [1, 21] is a center-of-charge motion, resulting from a charge cloud displaced from its equilibrium position undergoing stable $E' \times B$ drift about the axis of the trap, due to electric fields (E') from non-uniform distribution of image charges on the grounded trap-walls.

Figure 2.5 represents 2-D cut view of the plasma column with line density n_L of electrons, displaced from the axis by displacement D. The wall of radius R_w can be replaced by equal and opposite image charge rod located at distance S from the axis such that the potential at $r = R_w$ becomes constant, i.e. $\Phi(r, \theta) = const.$

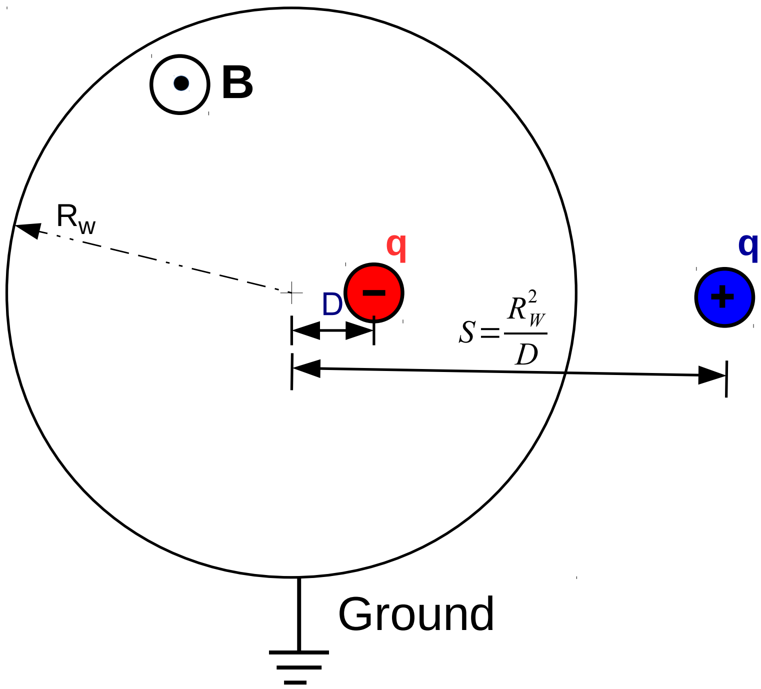

Figure 2.5: Image charge model of infinitely long cylindrical charge rod for Diocotron mode

Cylindrical symmetry brings the simplicity if we place the image charge at same azimuthal angle θ as the actual charges. Potential $\Phi(r,\theta)$ from two infinitely long oppositely charged rods can be expressed as follows:

$$\Phi(r,\theta) = -\frac{n_L q}{2\pi\epsilon_0}\left[\ln\sqrt{r^2+D^2-2rD\cos\theta} - \ln\sqrt{r^2+S^2-2rS\cos\theta}\right] \tag{2.14}$$

$$\Phi(r,\theta) = -\frac{n_L q}{2\pi\epsilon_0}\ln\left[\frac{r\sqrt{1+\frac{D^2}{r^2}-2\frac{D}{r}\cos\theta}}{S\sqrt{1+\frac{r^2}{S^2}-2\frac{r}{S}\cos\theta}}\right] \tag{2.15}$$

By choosing the appropriate constants $\frac{S}{R_w} = \frac{R_w}{D}$, one obtains the distance of image charge $S = \frac{R_w^2}{D}$. This gives the potential on the walls to be

$$\Phi(R_w,\theta) = \frac{n_L q}{2\pi\epsilon_0}\ln\left(\frac{D}{R_w}\right) \tag{2.16}$$

that is constant. The electric field due to an infinitely long line charge having line charge density $\lambda = n_L$ can be expressed using Gauss's law as

$$E(r) = \frac{n_L q}{2\pi\epsilon_0 r} \tag{2.17}$$

This can be used to obtain the electric field at the trap centre due to line image charge at distance 'S' as follows:

$$E(r=0) = \frac{n_L q}{2\pi\epsilon_0 S} = \frac{n_L q D}{2\pi\epsilon_0 R_w^2} \tag{2.18}$$

The $E \times B$ drift velocity of the charge cloud in this image charge electric field would be $v_d = \frac{E'}{B}$, and if displacement 'D' is assumed to be small enough $D \ll R_w$, then small amplitude infinite length Diocotron mode frequency is;

$$f_{dio}^{\infty} = \frac{v_d}{2\pi D} = \frac{n_L q}{4\pi^2\epsilon_0 B_z R_w^2} \tag{2.19}$$

These modes are detected through wall probes that are placed on the walls of the trap (capacitve probes) and are capacitively coupled to the plasma. A useful property of the diocotron mode as shown by the linear theory, is the dependency of the mode frequency upon the line density rather than on the radial density distribution. This fact has been exploited as a non-destructive diagnostic of electron plasmas whereby the frequency of the launched $m = 1$ diocotron mode has been used to estimate the line density of the plasma [25]. Cylindrical non-neutral plasmas have utilised such oscillations observed on capacitive probes (wall patches) to investigate the waves and transport activity [25], excitation of waves to diagnose & manipulate [73] and investigate dynamics [74–76] of non-neutral plasma.

One has to be careful during experiments, as the formula is valid for infinite length and small amplitude oscillations. Under following circumstances, diocotron mode frequency shifts a) finite amplitude of diocotron mode b) finite $\frac{L_p}{R_p}$ ratio c) finite temperature of the electron plasma.

2.1.3.1 Finite Amplitude shift in Diocotron mode

As the mode amplitude grows and displacement 'D' becomes large, the plasma column distorts into an elliptical cross-section and the frequency of the diocotron mode increases [10, 77]. Increase in frequency is given as follows:

$$f_{dio} = f_{dio}^{\infty} + f_{dio}^{\infty}\left(\frac{1-2(\frac{R_p}{R_w})^2}{[1-(\frac{R_p}{R_w})^2]^2}\right)\left(\frac{D}{R_w}\right)^2 \tag{2.20}$$

Thus as the mode becomes nonlinear, the mode frequency becomes dependent on the displacement of charge cloud from trap center and has also been utilized to find the displacement in several cylindrical trap [78–80] experiments.

2.1.3.2 Finite Length shift in Diocotron mode

For plasmas trapped in cylindrical Penning-Malmberg trap, the electrostatic confining potentials at the trap ends pushes the plasma in the axial direction, resulting in a radial force on the off-axis plasma. This force comes from the two components a) radial component of the confining potential F_c b) image charge force F_i. Now, these combined forces act on the actual plasma and make the plasma to rotate at higher drift velocity and increases the diocotron mode frequency as calculated by Fine et al [81] given as

$$\frac{f_{dio}}{f_{dio}^{\infty}} = \frac{F_{tot}}{F_{i,\infty}} = 1 + \left[\frac{j_{01}}{2}\left(\underbrace{\frac{1}{4} + \ln\left(\frac{R_w}{R_p}\right)}_{\text{Electrostatic Pressure}} + \underbrace{\frac{k_B T 4\pi\epsilon_0}{n_L q^2}}_{\text{Kintetic Pressure}}\right) - 0.671\right]\left(\frac{R_w}{L_p}\right) \tag{2.21}$$

The electrostatic pressure term as well as kinetic pressure terms pushes on the end confining potential and increases the diocotron mode frequency. Finite length of the image charge reduces the force and hence reduces the mode frequency and the particular constant 0.671 comes from the specific shape of the vacuum potential of the cylindrical electrodes. These corrections are necessary while estimating the line density from the measured diocotron mode frequency. For short and low density plasmas, the radial components of the confinement potential becomes dominant than the image charge term, in this regime, the 'diocotron mode' is called 'magnetron mode'. Interestingly, in this regime, the mode frequency is independent of the amount of the charge. The frequency of the mode becomes as follows [81]:

$$f_{Mag} = \frac{-E_r}{2\pi D B_z} = \frac{1}{2\pi D B_z}\left[\frac{\partial\phi_c}{\partial r} + \frac{\partial\phi_i}{\partial r}\right]_{r=D} \tag{2.22}$$

Here, ϕ_c is end confining potential and ϕ_i is image charge potential at $r = D$. For trap length L_p and confining potential V_c one gets the following mode frequency:

$$f = \frac{1}{2\pi B_z}\left[\underbrace{1.15\frac{V_c L}{R_w^3}}_{\text{Magnetron}} - \underbrace{1.0027\frac{Q}{R_w^3}}_{\text{Diocotron}}\right] \tag{2.23}$$

2.1.3.3 Higher-order Diocotron modes

The image charge model of the $m = 1$ mode is intuitive to understand but the mathematical treatment therein is limited for $m = 1$ only. For higher order modes, standard linear perturbation theory needs to be developed for the diocotron mode as given by Davidson [1]. It also discusses about the sufficient condition for the stability, i.e. the equilibrium is stable only if $\frac{\partial n}{\partial r} \leq 0$, or if the density is a monotonic density profile. It therefore turns out that diocotron waves are surface waves and dispersion relation of diocotron waves becomes

$$f = f_e[m_\theta - 1 + (R_p/R_w)^{2m_\theta}] \tag{2.24}$$

where m_θ is the azimuthal mode number, $f_e = \frac{n_L q}{4\pi^2 \epsilon_0 B_z R_p^2}$ is the common angular velocity with which electrons rotate about the axis as a solid body, R_p is plasma radius and R_w is the conducting cylinder radius [1, 60, 82].

2.1.4 Diocotron Instability

Electron plasma system is in a maximum energy state and stable diocotron waves are observed in the linear regime of the perturbation. The energy analysis of the mode suggests it is a negative energy mode. It can be driven unstable by any mechanism which takes away energy from the system. Such mechanisms can be electron-neutral collisions, presence of oppositely charged ions, resistive wall etc. Such mechanisms causes the mode amplitude to grow and it is called diocotron instability. Description of the diocotron instability driven by various mechanisms is discussed in this section.

2.1.4.1 Negative Energy Mode

The image charge model intuitively explains why Diocotron mode is a negative energy mode. When electron plasma makes a small displacement 'D' away from the equilibrium, it moves closer towards the image charges (that are chosen to make the boundary(wall) equipotential) and therefore the electrostatic energy of the system reduces. An anlogy often cited is the stored electrostatic energy between isolated parallel plate capacitor [83]. When the distance between two plates is reduced capacitance increases (since the capacitor remains isolated, charge Q remains constant). Since the stored energy $W = \frac{CV^2}{2} = \frac{Q^2}{2C}$, increase in capacitance reduces the total stored energy W.

Ignoring any kinetic energy, net electrostatic energy required to displace the electron column by distance 'D' in the image charge electric field can be shown as

$$W_{ElectroStatic} = \int_0^D Q \cdot E_i dx = \int_0^D q n_L L_p \frac{-n_L q x}{2\pi\epsilon_0 R_w^2} dx \tag{2.25}$$

$$= -\frac{(n_L q)^2}{4\pi\epsilon_0} \frac{D^2}{R_w^2} L_p < 0 \tag{2.26}$$

Since the energy required is negative, it implies that diocotron mode can be destabilized by dissipation of energy [82].

2.1.4.2 Resistive Wall Destabilization

As discussed in Sub-section 2.1.3, in the absence of any wall resistance or collisions, the $m = 1$ diocotron mode of an infinitely long plasma is marginally stable. However, finite sensing impedance that is must to record the diocotron mode amplitude, always offers a finite wall resistance to the plasma. Physically, resistive wall dissipates the electrical potential energy of the electron plasma, and the diocotron mode being negative energy mode, it makes stable diocotron mode unstable and the mode grows. The decrease in the electrostatic energy causes the displacement of the charge cloud. The feedback of displacement and energy dissipation continues and mode grows to large amplitudes, causing the plasma to move closer to the wall. Resistive wall destabilization was predicted and experimentally observed by

White et al [11]. The dissipative power P can be given as

$$P = \frac{I^2}{2} Re[Z] = \frac{I^2}{2} \frac{R}{1 + (\omega RC)^2} \tag{2.27}$$

where, I is the current, ω is the $m = 1$ mode frequency, R is wall-resistance and C is the capacitance. Mode growth rate is proportional to the power dissipated P. It can be calculated by energy conservation and is given as

$$\gamma_{RWD}^{cyl} = \frac{4\epsilon_0}{\pi} \frac{\omega^2 L_s^2 \sin^2(\frac{\Delta\theta}{2})}{L_p} \left(\frac{R}{1 + (\omega RC)^2} \right) \tag{2.28}$$

Here, L_s and $\Delta\theta$ are length of the wall-sector and angular size respectively. Initially for a given trap capacitance C, the mode growth increases with the increase in R. The growth rate will modify according to the geometry of the trap, capacitance being a geometric quantity. It will offer maximum growth for a particular combination of RC and will diminish with further increase of resistance. So interestingly, growth rate can be reduced by increasing the term $(\omega RC)^2 \gg 1$ i.e. by increasing R and C. Practically however, the impedance of the measuring circuit is adjusted such that it offers the lowest resistance to the current that is flowing through the wall/capacitive probe subjected to minimum signal level detection.

2.1.4.3 $e - n^0$ collision driven destabilization

It had been shown theoretically that, when electron plasma interacts with background neutral gas through elastic $e - n^0$ collisions with frequency ν_{en}, where $\nu_{en} \ll \omega_{ce}$, diocotron mode becomes unstable. $m = 1$ diocotron mode frequency is given by $\omega_0 = 2\pi f_{dio}^{\infty}$ and growth rate of the instability is given by $\gamma = \frac{\nu_{en}}{\omega_{ce}} \omega_0$. This suggests that, if all other destabilizing mechanisms are kept under control, then measurement of frequency of diocotron mode induced due to electron-neutral collisions may be used to directly infer the background neutral pressure owing to its linear relationship of the growth rate with ν_{e-n} [84]. Surprisingly in the experiments, the instability due to electron-neutral collisions excited the mode in very narrow pressure range [85] and got damped at higher pressure rather than making the mode unstable [86]. The mode damping rates were observed to be dependent on line charge density and magnetic field strength.

2.1.4.4 Ion Resonance/Driven Destabilization

Presence of a finite number of oppositely charged ions in the pure electron plasma can make it unstable. The instability is named as 'ion-resonance instability' and is studied theoretically by Levy et al [51] for trapped ions in the electron plasma potential well. As the name suggests the instability originates from the individual ion motion resonating with the bulk electron plasma's diocotron motion. During this process ions draw the energy from the plasma and the mode being a negative energy mode becomes unstable. The gradual displacement of the electron column from the trap's center takes place and mode grows. Condition for the growth is favourable when the frequency of the off-axis electron column ($m = 1$ mode frequency) matches or comes close to that of the ions making oscillations in electron potential well. Ions oscillate in the trap potential well with a frequency of $\Omega_i = \sqrt{\frac{n_e(1-\alpha)q^2}{m_e\epsilon_0}}$. Ions have formed in the trap due to electron-impact ionization of the background residual gas. Growth rate $\gamma^{ions}_{trapped} \propto \sqrt{\alpha}\omega_{Dio}$ is proportional to the Diocotron frequency which is close to ion plasma frequency ω_{pi}. It is given as $\omega_{pi} = \sqrt{\frac{n_i q^2}{m_i\epsilon_0}}$, where n_i is ion plasma density and m_i is the ion mass and α is fractional neutralization. Fractional ionisation is given as $\alpha = \frac{n_i}{n_e} = n_n < \sigma v > \tau$, where n_n is neutral density, σ is electron-impact ionization cross-section (averaged over the velocity distribution function) and τ is the time period for which ionization process has taken place. The ion oscillation frequency Ω_i is derived under the assumption that the electron plasma has a flat radial density profile, and creates a parabolic potential well with a unique ion oscillation frequency ignoring the effect of B field. The instability triggers (mode grows) as a threshold number of ions build up in the plasma well. Maximum growth occurs when frequencies are approximately equal. This classical model of ion resonance instability was developed for the trapped ions in the electron potential well, and was observed in the early experiments [50]. Dispersion relation of the instability is like two stream instability and stability boundaries were derived in the parameter space α the fractional neutralization and the magnetization parameter $\lambda = \frac{\omega_{ce}^2}{\omega_e^2} = \frac{2\epsilon_0 B^2}{m_i n_e}$. Narrow resonance curve is predicted in the magnetic field parameter space. Such an exponentially growing ion-resonance instability was supposed to be the dominant loss mechanism in toroidal electron plasma experiments [50, 52, 55]. Theoretically it is recommended to operate in stable parameter space of $\alpha - \lambda$ to avoid the instability.

The linearized macroscopic cold-fluid model including the role of strong self-electric field describes the instability as rotating two-stream instability due to differential rotation between the electrons and ions in equilibrium which was given by Davidson and Uhm [87]. Owing to the energy transfer from electron cloud to ion cloud, the mode becomes unstable and amplitude of the wave grows. In the presence of strong self-electric fields, for cases when fractional ionization α is significant, the dominating modes are found to be $m > 1$, whereas for very low fractional ionization $\alpha \ll 1$, $m = 1$ mode is the most destabilized mode and growth rates match up to that given by Levy et al. Influence of finite Larmor radius ($r_{Li} \sim R_p$) on the ion-resonance instability was also investigated using hybrid Vlasov-fluid model by Davidson et al [88]. It was found that finite Larmor radius can have stabilizing effect on $m \geq 1$ when self-electric field is relatively weak.

If the ions remain un-trapped in the electron plasma by some means, the very basic nature of the instability still remains the same but its features deviate from the classical ion resonance instability discussed so far. For example, in the cylindrical P-M traps the end potential can allow the ions to escape in the 'z' direction (axial) along the magnetic field lines. These ions still destabilizes the plasma as the ion creation process is continous. Experimentally it was observed [20,79] that several of the features were not in agreement with the classsical theory [51]. For example, the classical instability was supposed to have an exponential growth while the observed instability in cylindrical trap was linear in nature. Theory predicted narrow region of parameter space for resonance, while the plasma was seen to be driven unstable over a broad parametric region. Instability also had no threshold condition for ion build-up rather it was observed to occur at any population of ions. Growth rate of the instability was found to be linearly proportional to the ion plasma density not proportional to $\sqrt{n_i}$ as predicted by classical theory. Some of these features were explained by accounting for the transient nature of the ions and was renamed as 'transient ion-resonance instability' by Fajans [89].

The theoretical analysis was mainly non-linear and the evolution equation of displacement was obtained. Conservation of canonical angular momentum of the system was utilized to obtain the change of angular momentum of electron plasma to that of ions originating at random position and having random transit times.

Continuous production of ions changes the electron column's energy and canonical angular momentum. As ions move through electron plasma, the ion energy and momentum changes. As the total energy and canonical angular momentum of the system is conserved, when these ions escape out of the trap, the difference of energy gained by the ions must be transferred to the electron column. This change in electron column energy depend on the individual ion initial condition, which shall be averaged to obtain the net average change. The change is always positive and hence the instability grows. The growth of the instability is thus obtained by averaging of the ion motion over the initial conditions. Growth rate of the instability for these un-trapped ions is given by Eq. 24 of Ref. [89] as $\gamma_{un-trapped}^{ions} \approx \frac{\nu^+ r_p^4}{(1-r_p^2)\lambda}$, here $r_p = \frac{R_p}{R_w}$ is normalized plasma radius and ν^+ is the ion production rate. Theory predicts a linear growth rate for experimental plasma density profile and a broad density profile. Experiments carried out at University of California, San-Diego (UCSD) demonstrated the destabilization of the electron plasma with trapped as well as un-trapped ions and has shown the exponential behavior of the growth [90]. They also demonstrate the linear growth in previous experiment which is ascribed to the cooling of electron plasma (after RF field is 'OFF') and hence reduction in the ion production rate causing the slowed exponential instability. The growth rate was dependent upon the ion production rate.

The importance of ion-resonance instability cannot be understated. The instability is important for anti-matter community as they use electron plasma to cool anti-protons for anti-Hydrogen production in double well configuration [91]. Hence it is very necessary to understand the stability regime of operation and avoid the occurrence of the instability in cylindrical as well as in toroidal experiments for long-time confinement experiments.

Numerical Analysis of IRI

Numerical analysis of ion-resonance instability for the effect of slow and fast azimuthal motion of equilibrium was carried out by H. C. Chen and it was found that fast rotational equilibrium is stable whereas the slow rotation of the cloud was found to be unstable to the finite fraction of ions [92]. Ion resonance instability has been recently investigated in numerical experiments (using PIC code) in its linear and non-linear phase. Dynamics and energetics of the instability has been studied and discussed in detail in [93]. Exponential growth rate of the instability in its linear mode obeys the linear analytical model of ion-resonance instability developed by Davidson and Uhm [87]. Owing to the energy transfer from electron cloud to ion cloud, phenomena such as wave-breaking of the poloidal mode on the ion cloud and pinching of the poloidal perturbations on the electron cloud was observed in the non-linear phase of the instability. The effect of elastics collisions and excitation between electron and background neutral on the ion resonance instability was investigated using simulation based on 2-D PIC with MCC code [94]. Axial bounce motion of electrons was also introduced to mimic the electrostatic end-plugs used in cylindrical Penning-Malmberg trap. Effect of non-ionizing e-n collisions is separately investigated here and it was found that such collisions can't trigger the instability in the electron cloud independently. However, in an ongoing instability indirect effects can contribute towards increase in growth rate via feedback process of dynamically changing electron density and fractional density of ions.

2.1.5 Transport

Particle, angular momentum and heat transport in the plasma across a magnetic field is one of the most fundamental problems of plasma confinement. It is well-known that in the absence of any external torque, NNP can stay confined forever as the total canonical angular momentum remains conserved. Transport of the NNP will occur only due to any external physical mechanism that provide torque to the plasma. Any such additional torque shall lead towards an expansion of the mean plasma radius $\langle r^2 \rangle$. This can occur due to electron-neutral collisions [8, 95], externally launched wave [96, 97], and asymmetry induced by end potentials [98, 99], applied asymmetries [100] or field errors (electrostatic [13, 98, 101] / magnetostatic [102, 103]). Nonlinear effects can also contribute to the transport through field errors and excite plamsa modes and exert torque on the electron plasam column [104]. Transport in NNP due to such external mechanisms is referred as 'Externally Induced Transport'. Any other rearrangement which conserves the mean square radius is termed as 'Internal Transport'.

It has been observed experimentally that at high pressures, transport is governed by electron-neutral collisions and obey the theoretical scaling, $\tau_m \sim P^{-1}B^2$

scaling, where τ_m is the time required for the initial central density to reach half of its value. Transport in this regime of operation is driven by mobility rather than diffusion where plasma radius is very large compared to its Debye length ($r_p > \lambda_D$). At high pressures, effects such as field errors are found to be negligible. At pressures $P \leq 1 \times 10^{-7}$ mbar, the scaling breaks and observed confinement times are shorter by 2 orders of magnitude than predicted by theory. To understand the mechanism responsible in this regime, dependency of transport time scale on plasma length was examined and was found to scale as L^{-2}. This scaling is found to be consistent even when field asymmetries are reduced. This transport is driven by global field errors in the confining geometries due to marginally trapped particles in the field asymmetries [105]. Experiments of transport due to applied asymmetries are also carried out and underlying mechanisms enhancing the transport due to field errors has been identified.

Transport due to asymmetric confining end potentials is found to be dominant when plasma gets displaced from the trap center, i.e. when $m = 1$ diocotron mode is excited. This can cause oscillation in plasma length (the axial compression) and cause the heating of electron column via electron-electron collisions (the collisional dissipation). This transport mechanism is called 'rotational pumping transport' and is proportional to electron-electron collision frequency and weakly dependent on the B-field through Coulomb logarithm [98, 99].

Internal transport in the NNP is driven by like particle collisions. It is of prime importance to understand how like-particle collisions transport heat, particles and angular momentum. Collisions within like particles lead to rearrangement that can drive the electron plasmas towards thermal equilibrium. This has been shown theoretically [23,24] as well as has been proved experimentally [18]. The characteristic time scale τ_{eq}, required for the particle transport to reach the equilibrium, was observed to follow the $1/B$ field scaling. This is in contrast to the 'classical transport theory', which predicts $1/B^2$ scaling. The classical theory describes transport in terms of the short range velocity scattering of particles. In $r_c > \lambda_D$ regime, where r_c is Larmor radius and λ_D is Debye length, elementary radial diffusion step size is r_c and time step is ν_{e-e} collision frequency and transport scales as $D^{class} \sim \nu_{e-e} r_c^2$. Here collisions occur in the impact parameter range of $\lambda_D < b < r_c$. Though experimentally observed transport does not follow the behavior. This is primarily due to the fact that in NNP impact parameter of collisions falls in the $r_c < b < \lambda_D$

regime, whereas classical transport theory considers only short-range collisions with impact parameters falling in $\lambda_D < b < r_c$ range. New guiding center theories of like-particle collisional transport considers these un-shielded long-range collisions [106, 107] and gives new transport time scales where elementary radial step is λ_D for energy and momentum; this agrees well with experimental measurements. In addition to this, particles can also exchange energy by absorption and emission of weakly damped plasma waves over a spatial scale of plasma dimension, R_p. This wave transport was also recognized as dominant transport process where plasma radius $R_p > 100\lambda_D$ for heat transport and $R_p > 1000\lambda_D$ for momentum transport [106].

Damping

In addition to the transport, all of these mechanisms if they give energy to the mode also damp the plasma modes observed in the NNP. Exponential damping of the diocotron modes can occur through electron-neutral collisions, rotational pumping transport, spatial Landau like resonances [108] and trapped particles mediated [105] processes. Electrostatic diocotron modes $m \geq 2$ gets damped in the electron plasma by Landau like damping mechanisms at r_s radial location, as self rotation frequency $f_R(r)$ matches with the wave frequency f_m at this radial location. $m = 1$ mode is marginally stable as the critical resonance radius is at R_w. The observed mode damping is exponential. Algebraic mode damping of diocotron waves is also observed when halo of particles forms around plasma column. This damping is different from spatial Landau like damping process and occurs when particles get trapped in cat's eye like structure; damping is associated with sudden particle loss as plasma crosses r_s.

Transport associated with all these damping mechanisms is important to understand the overall transport associated with NNP in other trap geometries such as toroidal systems.

2.2 Theory and Experiments of NNP in Toroidal Traps

As cylindrical traps offer remarkable confinement properties for NNP, and confine plasmas almost indefinitely, question might arise why one should study NNP in toroidal configurations. One can think of the following reasons justifying the investigation of NNP in toroidal magnetic field topologies. Toroidicity can make the particle orbits complicated and thereby introduce new physics. For example, strong toroidicity may bring in a lot non-linearity which is interesting in its own merit. A quiescent, long-lived, well confined non-neutral plasma in toroidal geometry can allow for high precision plasma physics experiments. For example, one may slowly bleed in the opposite charge species, and study the transition from non-neutrality to neutrality with all its complexity. Another interesting advantage of toroidal traps is that with its purely magnetic configuration, one can aspire to confine both signs of charged particles simultaneously. This feature makes such traps ideal for producing hitherto unexplored exotic pair plasmas such as electron-positron and proton-antiproton (anti-hydrogen) plasmas, which are of very fundamental interest to plasma physics, astrophysics and antimatter or particle physicists [109, 110].

2.2.1 Theoretical Background of Toroidal NNP

Present section discusses the theoretical framework that describes the behavior of non-neutral plasmas in a purely toroidal magnetic field. Equilibrium, stability and transport processes are discussed in the context of the present thesis work.

Equilibrium and Stability

For purely toroidal magnetic fields, the simplest equilibrium model of the electron cloud was outlined by Daugherty and Levy [48]. K. Avinash [56] reviewed the equilibrium in terms of balance of forces including plasma diamagnetism. Both of these suggested the possible existence of equilibrium. In other words non-neutral plasma can be confined in the purely toroidal magnetic fields without any help of externally applied rotational transform unlike neutral plasmas in tokamaks. In the absence of drifts, potential surfaces will coincide with drift surfaces. However, presence of curvature and ∇B drifts along with centrifugal drift, cause the shifting of the drift surfaces away from the potential surfaces. Presence of image charges on the conducting boundary causes the plasma to shift inward (towards major axis of the torus) and balances this drift. The inward shift is of the order of $\sim \epsilon q$, where $\epsilon = \frac{a}{R_0}$ is inverse aspect ratio of the torus with a as minor radius and R_0 as major radius of the torus and $q = \frac{\omega_{pe}^2}{\omega_{ce}^2} \ll 1$ (ω_{pe} is plasma frequency and ω_{ce} is cyclotron frequency). It is a cold ($T = 0$), one fluid model in which the electron fluid velocity is determined by the $\vec{E} \times \vec{B}$ velocity. Partial differential equation governing the two-dimensional equilibrium of non-neutral plasma in a purely toroidal magnetic field is derived in the limit $q \to 0$. Set of fluid equations used are as follows:

$$n_e q\vec{E} + \vec{J} \times \vec{B} = 0; \vec{E} = -\nabla\Phi \tag{2.29}$$
$$\vec{\nabla} \times \vec{B} = \mu_0 \vec{J} \tag{2.30}$$
$$\nabla^2\Phi = \frac{n_e q}{\epsilon_0} \tag{2.31}$$
$$\vec{\nabla} \cdot \vec{B} = 0 \tag{2.32}$$

where n_e and $\vec{J}$ are plasma and current densities respectively, $\vec{E}$ and $\vec{B}$ are electric and magnetic fields, Φ is electrostatic potential. Here, inertia is neglected and kinetic energy of the plasma is assumed much smaller than electrostatic potential energy, hence we neglect the plasma pressure term in the equation of motion. We use the cylindrical co-ordinate system (R,ϕ,Z), where ϕ is a toroidal angle and toroidal symmetry implies $\frac{\partial}{\partial\phi} = 0$. Taking dot product of Equation 2.29 with $\vec{J}$, gives

$$\vec{J} \cdot \nabla\Phi = 0 \tag{2.33}$$

Using Ampere's law, one can get the R and Z components of the current density as

$$J_R = -\frac{1}{\mu_0}\frac{\partial B_\phi}{\partial Z} \tag{2.34}$$
$$J_Z = \frac{1}{\mu_0 r}\frac{\partial (rB_\phi)}{\partial r} \tag{2.35}$$

Equations 2.33 and 2.34 implies rB_ϕ to be an arbitrary function of potential

$f(\Phi)$. Considering R component of the equation of motion Eq. 2.29

$$n_e q \frac{\partial \Phi}{\partial R} - J_z B_\phi = 0 \tag{2.36}$$

substituting for J_z, B_ϕ and using Poisson's equation one obtains

$$\nabla^2 \Phi = \frac{1}{\mu_0 \epsilon_0} \frac{f(\Phi)}{R^2} \frac{\partial f(\Phi)}{\partial \Phi} \tag{2.37}$$

Equation 2.37 is a Poisson's equation with nonlinear charge distribution or modified Daugherty-Levy equation including diamagnetic corrections of the toroidal field, although diamagnetic term is negligible for low density plasmas. Solution of Equation 2.37 can provide equipotential surface in the zeroth order, inward shift as first order correction. This shift leads to the higher induced charges on the inboard side which attracts the electron plasma and hence allowing for force balance. In the absence of conducting cylinder, this can be balanced by external electric field. Effect of the externally applied electric field on the equilibrium and required electric field to shift the equilibria to the geometric centre was calculated [58]. Toroidal corrections to the $l = 1$ diocotron mode frequency of the order of $\sim \epsilon^2$ were obtained and applied electric field was also found to reduce the $l = 1$ cylindrical diocotron mode frequency [111]. The study was approximated by the simple circuit model and internal plasma dynamics was ignored as well as any shape effect of the plasma were also not taken into account.

Stability of the equilibria was analyzed by O'Neil et al [49] and a sufficient criteria for the stability of the equilibrium was derived. Frequencies of interest were ordered ($\omega_{ce} \gg \omega_T \gg \omega_E$) such that the cross-field transport can be described by toroidal-averaged drift dynamics, where $\omega_T = \frac{\bar{v}}{r}$ is toroidal rotation frequency. It was found that a stable plasma equilibrium state is possible for which electrostatic energy is a local maximum in comparison to all the other neighboring states that are accessible under general constraints of the toroidal average drift dynamics. The state is found to be stable to small amplitude perturbations as energy of the system is conserved. The system evolves in a space of allowable states on a constant energy contour, and shrinks to the point when energy is maximum and no further change is possible. The stability theorem was developed using variational principle and a state with maximum local electrostatic energy was obtained for which any first-order variation vanishes and second-order variation is negative.

Magnetic Pumping Transport

It has been theoretically shown that toroidal curvature of the magnetic field, via electron-electron collisions drive the slow cross field transport of electron plasma [59]. It is believed that frequency ordering $\omega_{ce} \gg \omega_T \gg \omega_E \gg \nu_{e-e} \gg \tau^{-1}$ is followed. Transport mechanism may be understood by considering a single flux-tube inside the toroidal electron plasma. As the plasma undergoes poloidal $E \times B$ drift (rotation due to self E-field) around the plasma center, the length of the flux tube as well as the magnetic field strength oscillates. Two adiabatic invariants $\mu = \frac{mv_\perp^2}{2B}$ and $J_\parallel = (2\pi)^{-1} \oint mv_\parallel dl$ demand cyclic variations of $T_\parallel$ and $T_\perp$. This oscillating variation of the quantities being unequal (as $\tilde{v_\perp} \neq \tilde{v_\parallel}$) relaxation between the two causes a slow heating of the plasma. Heating draws the energy from the electrostatic potential well and plasma radius expands. The transport is called magnetic pumping transport and is also observed in tokamaks where it slows down the poloidal rotation [112]. The transport flux rate, derived using heuristic arguments or kinetic treatment (drift-kinetic Boltzmann equation), in the large aspect ratio limit is as follows

$$\Gamma_{MPT} = \frac{1}{2}\nu_{\perp,\parallel} n(r) \frac{2T}{-e\partial\Phi/\partial r}[(r/R_o)^2] \tag{2.38}$$

here, $\nu_{\perp,\parallel}$ is electron-electron collisional equi-partition rate. The transport time scale can be obtained by performing scaling (dimensional) analysis following Stoneking's procedure [60] by dividing particle inventory with surface integral of the flux equation as follows:

$$\tau_{mp} = \frac{n_{av} 2\pi^2 a^2 R_o}{\Gamma_{MPT}\pi^2 a R_o} \tag{2.39}$$

Here, n_{av} is volume averaged electron density, and using $\nu_{\parallel,\perp} \sim n/T^{3/2}$ and $\partial\Phi/\partial r \sim nea$, transport time scale can be written as

$$\tau_{MPT} = 0.02 \cdot R_0[\text{cm}]^2 \sqrt{T_e[eV]} \tag{2.40}$$

This makes the transport time scale independent of minor radius and magnetic field. Confinement time in toroidal traps is presumed to be limited due to magnetic pumping transport limit.

Next section discusses about experiments carried out in toroidal geometries on closed magnetic field lines(purely toroidal B-field), magnetic field surfaces formed by different techniques(dipole, stellarator) and open magnetic field lines(partial torus with purely toroidal magnetic field lines). Important experimental results along with confinement time observed in these configurations are highlighted.

2.2.2 Experimental Background of Toroidal NNP

This section reviews the NNP experiments in the different magnetic topologies which can be constructed in a toroidal geometry. Apart from the open-ended magnetic field line configuration with electrostatic end plugs (*i.e.* cylindrical Penning - Malmberg trap; the most successful one), other kinds of equilibria of NNP are possible on closed magnetic field lines with purely toroidal magnetic field [113] and on magnetic surfaces [114]. As stated earlier, toroidal geometry can be a motivation to explore confinement of multiple species of different charges leading to anti-matter and exotic plasmas [41] or can be used to create plasmas with arbitrary degree of non-neutrality or to trap high energy particles [39].

Historically the experiments date back to early 70's when NNP in toroidal configurations with pure toroidal magnetic field of closed field lines were considered as a promising application for producing high-Z ion source [43], heavy ion beam accelerator [115], inertial fusion [46], heating neutral plasmas using relativistic electron beam [53] etc. Experiments of collective focusing ion accelerator using magnetically confined electron cloud were also conducted for accelerating ions [116, 117] in bumpy toroidal magnetic field. These experiments were mainly focused towards trapping of charged particles with high-energy for heavy ion acceleration. But the limited confinement time of few $10\,\mu$s to few $100\,\mu$s remained a bane and such plasmas couldn't be utilized to turn any of the applications a reality. Experiments of electron plasmas in these large aspect ratio traps [50, 53, 118] are reviewed later along with important results.

In the late 90's experiments on electron plasmas were initiated in a small aspect ratio torus at Institute for Plasma Research, India. Equilibria, stability and transport properties of toroidal electron plasmas where investigated in the small aspect ratio regime. Radial electric fields, self-generated by NNP or augmented by external means, and their role in confinement in toroidal configurations [54] was a part of theoretical and experimental investigations. These experiments in small aspect ratio traps [55, 57] are discussed and important results are described in this section.

In last two decades or so, a few more novel experiments of NNP in toroidal geometry have emerged. Toroidal geometries that use closed magnetic flux surfaces, like in tokamak and stellarators, have always been popular for confining neutral plasmas. Magnetic flux surfaces in toroidal configuration can also be achieved using ring conductor (dipole magnet), either mechanically supported in the vacuum chamber or by levitated superconducting ring magnets. Experiments of electron plasmas on magnetic surfaces in Proto-Ring Trap(Proto-RT) [119] and Ring Trap-I (RT-I) [67] are such examples of producing laboratory magnetospheric configuration. Electron plasma confinement time exceeding $> 300\,\mathrm{s}$ has been achieved in RT-I [69]. A helical device can also be an alternate option/approach to produce closed magnetic surfaces with external winding. Compact Helical Stellarator (CHS) [120] and Columbia Non-Neutral Torus [65] (CNT) experiments are such examples with different stellarator configurations. Important results from these novel experimental devices are also summarized.

Introducing the electrostatic potential end-plugs in a continuous torus by breaking the toroidal symmetry and confining electrons in a partial torus ('C' shaped trap) is like creating a toroidal Penning trap for NNP. Implementation of this novel concept in a large aspect ratio toroid (LNT [61]) and in the small aspect ratio regime (SMARTEX-C [121]) was sucessfully demonstrated in the early 2000. These experiments with purely toroidal B field have open field lines and have provided a breakthrough in confining electron plasms in toridal geometries. Gradual improvement in confinement time have been reported from these toroidal traps leading to a steady state confinement for about a sec [60, 122]. The reported confinement time approaches the limit set by the magnetic pumping transport theory. Our thesis attempts a similar trapping in a small aspect ratio regime and investigates the confinement time in the context of existing transport theories.

Closed Field-line Configuration: Full Torus

Initial toroidal non-neutral plasma experiments had demonstrated existence of the equilibrium of toroidal electron plasma without the aid of any rotational transform [50]. The experiments in toroidal configuration were aimed to create electron cloud for a promising application, namely for producing a high-Z ion source [43], heavy ion beam accelerator and for using it as an electrostatic shield from space radiation for satellites [47]. Large aspect ratio toroidal device was used to create the electron plasma using an inductive charging technique. The confinement time of the electron plasma was observed to be of the order of $60\,\mu$s. The observed equilibrium was found to be unstable, ion build-up being primarily responsible. These ions get formed by injected electrons through electron impact ionization of residual neutral gas. It was found that until ions build-up to $\sim 10\%$ of the electron plasma density, no instability would emerge. The electron plasma potential well gets shallower with the loss of charged particles out of the toroidal trap during the rapid growth of the instability and explains the limited containment of electron cloud in the toroidal apparatus.

Other experiments carried out in full-torus [53, 118] were aimed at producing high energy relativistic electron beam or high density toroidal electron rings for heating and confinement of neutral plasmas. Mohri et al had created relativistic electron beam using field-emission with density of $1 \times 10^{8}\,\mathrm{cm}^{-3}$ having an energy of 450 keV for containment time of $20\,\mu$s. Once again, confinement time was observed to be limited by the presence of the ion-resonance instability. Clark et al had produced a high density electron cloud using a different injection scheme than inductive charging. Electron cloud produced had a potential depth of 300 kV implying a density of $\sim 1 \times 10^{10}\,\mathrm{cm}^{-3}$ for approximately $200\,\mu$s of confinement time and here also ion driven instability was believed to destabilize the electron cloud and destroy the confinement.

Small aspect ratio toroidal experiments at IPR, produced electron plasma using inductive charging scheme in full torus with purely toroidal magnetic field [54, 55, 123]. Equi-potential contours were measured using high-impedance Langmuir probe in the poloidal plane confirming the inward shift of the charge cloud in toroidal magnetic field. Toroidal symmetry of the charge cloud was also confirmed. Elliptical and triangular deformations in the potential contours were also observed. It proved the existence of the equilibrium even on tight aspect ratio of ~ 1.3 and equilibrium lasted longer than any other drift time scales in the system. The observed confinement time though was limited to few 100 μs. Interesting similarities and differences between toroidal charge ring and toroidal current filaments in neutral plasmas (held in tokamaks for thermonuclear fusion research) have been brought out by the authors [54, 55]. Capacitive effects observed in NNP is analogous to inductive effects, image charges are replaced by image currents, inward shift is replaced with outward shift, zeroth order DC electric field is replaced with vertical B-field and vortex formation in charge cloud is similar to that of magnetic island formation. In similar way, one can also compare magnetic re-connection in neutral plasmas with vortex merger phenomena in NNP and the role of resistivity in neutral plasma is played by viscosity in non-neutral plasma. To overcome the instability and remove the ions, an additional inner-wall is introduced. It can be used to apply external electric field to remove the ions from the trap as well as to observe its effect on confinement time. It was predicted theoretically that external radial electric field can overcome the toroidal drifts and prevent the particle losses [124]. Additionally, a novel injection scheme was attempted to produce the toroidal electron plasma by combination of self electric field and externally applied electric field E^r_{ext}. $\nabla B \times B$ drift was utilized to inject the electrons from the toroidally symmetric cathode-anode arrangement installed at the bottom of the trap. Effect of external radial electric field on equilbrium was investigated and found to alter the equi-potential contours [57]. Hollow density profile observed initially got filled with the application of radial electric field and potential well depth of the cloud exceeds the initial kinetic energy of the electrons. Confinement time however remained limited due to the presence of ions for $\sim 250\,\mu$s. A 2-D electrostatic code was also developed to investigate the processes observed in the experiments and numerical investigations were carried out for various aspect ratios. Plasma is observed to shift inwards with respect to the minor axis and the effect is seen to increase when aspect ratio is reduced [125].

Toroidal Magnetic Surfaces

NNP on magnetic flux surfaces can be produced in dipole ring magnet and stellarator like configurations. Experiments in Proto-RT and Ring Trap-I are examples of dipole like ring magnet producing laboratory magnetospheric configuration. Electron beam was injected at the magnetic separatrix of the trap. Injected particles diffuse across the magnetic surface by the chaotic drift surfaces which spread the electron beam in the confinement region. Long chaotic orbits of the charged particles along with non-adiabatic effects cause the charged particles to diffuse inwards and produced peaked density profile. Confinement of electron plasmas in RT-I exceeds 300 s and is limited by the transport due to electron-neutral collisions or by rapid destabilization of the plasma due to the presence of ions. Long-lived NNP self organizes itself in an in-homogeneous magnetic field where density is no longer homogeneous and rotates rigidly just like in a homogeneous B-field. Under suitable topological constraints the Boltzmann distribution is the relaxed state, hence the electron plasma in magnetospheric configuration evolves towards thermal equilibrium.

CHS uses stochastic magnetic region to inject charge particles across the helical vacuum magnetic field surfaces via collisionless inward propagation. It also reports the existence of the plasma equilibrium on magnetic surfaces having non-constant potential and density profile and preliminary measurements of hot electron plasma temperature of few hundreds of eV have been carried out using emissive Langmuir probe. The confinement time observed in CHS is of the order of ~ 1 ms, which is limited due to disruptive instability [66]. Similarly NNP in toroidal geometry with helical magnetic axis in Heliotron J is also produced [126] but no results on confinement were reported.

Confinement of electron plasma on magnetic surfaces in simple stellarator CNT was explored at Columbia University [114]. CNT was also proposed as an ideal stellarator to study the equal-mass electron-positron plasma as well as for performing experiments of arbitrary degree of neutrality. Equilibrium of the electron plasma in CNT and its 2-D solutions to the equilibrium equations is obtained numerically [127]. Equilibrium shifts outward for NNP confined on magnetic surfaces surrounded by the conducting boundary which is in contrast to the equilibrium reported from toroidal traps with purely toroidal B-field. Stability analysis of the perturbations to equilibrium show that the equilibrium is stable [128]. Transport on magnetic surfaces of the stellarator was predicted to be determined by the neoclassical effects [129] and is inferior to that of magnetic pumping transport proposed as a limit to confinement in purely toroidal magnetic field. Initial electron plasma experiments in CNT confirmed the existence of the stable equilibrium lasting for 20 ms in steady state with all the internal objects in confinement region [65]. The low confinement time limit is attributed to the presence of bulk insulating materials in the plasma. These insulated structures acquire negative polarity and create the $E \times B$ convective transport cells [130]. Confinement was improved by reducing pressure and increasing B-field strength and installation of a flux conforming electrostatic boundary. Transport rate in this parameter regime was inversely proportional to the magnetic field and linearly proportional to the pressure. Maximum confinement time observed was around ~ 0.3 s. Upon removing all the internal objects and installing movable filament source, the observed confinement time was limited to < 0.1 s and was attributed to the accumulation of ions [131].

Open Field-line Configuration: Partial Torus

Successful confinement of electron plasma in cylindrical Penning-Malmberg trap has influenced the idea of using the end-plugs in toroidal traps. This of course interrupts the toroidal symmetry and makes the trap a partial or 'C' shaped torus. Implementation of the concept in large aspect ratio device at Lawrence University (LNT-I) and in small aspect ratio trap at Institute for Plasma Research, India (SMARTEX-C) has led to the two contemporary devices.

LNT-I had confined electron plasma of densities $\sim 3 \times 10^6\,\mathrm{cm^{-3}}$ with the application of radial electric field as strong as $\sim 10\,\mathrm{V\,cm^{-1}}$ and had reported confinement time of the order of $\sim 100\,\mu$s at 200 Gauss magnetic field [61]. Plasma was trapped in 300° region of the full torus. Confinement time was estimated by the damping rate of low-frequency oscillations observed on the capacitive probes. Total charge was also measured by dumping the charges on the end-grid. Later with the application of higher radial electric field $60\,\mathrm{V\,cm^{-1}}$, confinement time as long as ~ 2 ms was estimated [62]. Improvement in confinement was observed with the application of the feedback stabilization of the diocotron instability observed due to the presence of the ions in the trap. As soon as the unstable diocotron mode on any of the capacitive probe was detected, it was phase shifted, amplified and applied to the inner middle horizontal field electrode and the mode got suppressed. Such similar techniques had earlier been applied in the cylindrical traps

[132]. With the help of the technique, confinement time was observed as long as 18 ms. Thus, applied radial electric field and feed-back control of the diocotron instability appeared to play an important role in improving the confinement time. Empirical confinement time scaling of Cylindrical Penning-Malmberg trap with plasma length L and magnetic field B is given as $\tau_{Cyl}[\mathrm{s}] = 1.6 \times 10^{-2}[\frac{L[\mathrm{cm}]}{B[Gauss]}]^2$ [9]. The observed confinement time in LNT-I was compared with this scaling and it was concluded that no significant toroidal effects were present on the observed time scale. The confinement time observed was primarily limited due to ion driven instability but with the feed-back control this limit was overcome. Fundamental limit at this stage was speculated due to asymmetry induced transport and time-scales were compared with empirical formula deduced from cylindrical trap experiments.

LNT-I has been since upgraded to LNT-II that has achieved better vacuum ($< 1 \times 10^{-9}$ mbar), minimum electrode fabrication errors to reduce field asymmetries, kilo-Gauss scale high magnetic field, open(hollow) segmented Au plated Al electrodes (instead of end-grid), radially retractable electron source mounted on pneumatic bellows [133]. These features allow the LNT-II to operate it in partial ('C-shape') torus or full torus mode. The device has been built to minimize the transport driven by collisions with neutrals and observe the Magnetic Pumping Transport(MPT) predicted [59] to be dominant in such plasmas confined by purely toroidal B-field. Confinement time was obtained from the charge loss-rate obtained from the time evolution of line density estimated from frequency of diocotron mode launched in the electron plasma. The observed steady state confinement time of electron plasmas lasting beyond 1×10^5 $E \times B$ oscillations which corresponds to ~ 3 s without any aid of radial external electric field [60, 64] was reported which is lower but approaching the confinement time limit predicted by the MPT theory. Charge loss rate with magnetic field was observed to be scaling as $\tau \propto B^{3.7}$ [60]. Increase in confinement time was observed as the toroidal arc length (confinement region) is reduced and depends as $\tau \propto L^{-2}$. This shows remarkable similarity with the experiments of cylindrical Penning-Malmberg traps [8, 9]. For short electron plasmas in LNT-II, the observed confinement time exceeds the limit posed by MPT theory for an assumed temperature of 1 eV. Diocotron mode damping rate was found to be scaling as $\gamma \propto B^{-3}$ in partial torus. As transition is made to full-torus, the confinement time is observed to reduce and this is attributed to longer length of the plasma column as well as build-up of ions in the trap [134]. The observed scaling of confinement times with magnetic field and plasma length in addition to the damping rate of the diocotron modes are as yet unexplained.

SMall Aspect Ratio Toroidal Electron plasma eXperiment (SMARTEX) at Institute for Plasma Research (IPR) [55, 57], initially carried out in a full torus (SMARTEX-T, 'T' implying Full torus) also implemented the idea of toroidal Penning Trap in the late 90's. The trap was converted into a partial toroidal trap (SMARTEX-C) and the electrons were injected along the field lines. Successful trapping was demonstrated for few milliseconds [63, 135]. Pulsed B-field produced using Pulse Forming Network (PFN) was decaying in 4 ms after a steady state of 1.2 ms. The equilibrium existed for the entire duration of pulsed B-field length without any aid of external radial electric field. The rapid injection of charge particles in the empty trap forms sufficient space charge electric field that allowed dynamical equilibrium by overcoming all the ∇B and curvature drifts in the tight aspect ratio regime. Capacitive probes and Charge collector diagnostics were developed and acted as the principle diagnostics in the system. Charge collector diagnostics was crucially challenged by dominant capacitive pick-ups. Fast dumping of the charges induced a displacement current in the collector grid, which was cleverly removed by a shield electrode improving the signal to noise ratio [136].

The electron plasma exhibited coherent double-peak diocotron oscillations comprising many harmonics with dominant power in $m = 2$ mode which indicated the elliptical shaping of the electron cloud. At an operating pressure of 1×10^{-7} mbar and magnetic field of 200 Gauss the mode oscillations were seen to grow in amplitude right from the end of injection period, before saturating and damping. The electrostatic activity decayed with the decay of magnetic field (~ 4 ms). Due to the limited duration of confining field, it became difficult to quote the accurate confinement time of electron plasma in SMARTEX-C and any corresponding investigation of transport mechanisms [121]. So at a later stage, the pulsed B-field power supply (PFN) was redesigned with additional inductors L and capacitors C. B-field pulse length with flat top of ~ 11 ms and total pulse length of 20 ms was obatined. Electron plasma experiments with this B-field showed that the mode oscillations continued to grow, saturate and decay within the flat-top of the B-pulse [137]. It proved that even if the confining fields were to be extended and improved, the observed confinement time was fundamentally limited due to the instability driven transport. The instability growth was scaled with background neutral pressure and the growth rates were found to slow-down with decrease in ionization. The base pressure of the system was $\sim 4 \times 10^{-8}$ mbar but operating pressure during filament heating rises to 8×10^{-8} mbar that too for very few minutes. Systematic Residual Gas Analysis (RGA) of the vacuum system revealed the gigantic amount of H_2 gas released as soon as filament was switched on. The source of the observed gas-load were the current leads that were made up of Cu. When these were replaced with Stainless-Steel 304 leads operating pressures of the order of $\sim 5 \times 10^{-8}$ mbar sustained well for the entire duration of operation. The experiments in this regime demonstrated some control over instabilities but the observed confinement time ($\sim$ 10 ms) did not exceed the existing magnetic field pulse length. Thus, the observed confinement was limited due to the high background neutral pressure.

The careful RGA analysis suggested the dominant gas load of CO_2 prevailing due to the Viton elastomers used to seal the major ports of the vacuum vessel. Upon replacement of these sealants, it became possible to bake the vacuum vessel to high temperatures of 250 °C. These measures taken led to an improved base pressure of $\sim 4 \times 10^{-9}$ mbar and operating pressure of $\sim 4 - 5 \times 10^{-9}$ mbar. Simultaneous up-gradation of the magnetic field PFN was also necessary as the flat-top of the pulse was limited to 11 ms. PFN pulse length was out-stretched with $\sim$ 30 ms flat-top and total pulse extending $\sim$ 100 ms duration. Electron plasma experiments were carried out at these pressures and magnetic field, and could successfully confine the electron plasma well beyond 30 ms. The growth rate of the instability got arrested and quiescent electron plasma lasting for the steady state duration of the B field could be obtained [137]. The instability grew as soon as the B-field started to decay, then saturated and damped within the magnetic field pulse length. Limited capabilities of the PFN and electron plasma out-living the steady state pulse duration, made it once again impossible to quote for the confinement time and the prevented any further investigation.

In addition to the above, the diagnostics is challenged by unique complexities. Cylindrical traps have resorted to imaging of the plasma by dumping it onto a phosphor screen with a CCD camera placed at one end of the trap [138]. Similar imaging has been difficult in SMARTEX-C. Due to its toroidal geometry, the toroidal trap obviously has no “ends” where a camera can be placed conveniently. Charge collector diagnostics, also popular in cylindrical traps [18], has been adapted in SMARTEX-C to a limited extent for measuring total charge [139]. However obtaining the spatio-temporal distribution has been difficult as it requires fast dumping of charges relative to the poloidal drift time scales, to avoid smearing of the charge profile. Obtaining plasma parameters i.e. plasma potential Φ_p, temperature T_e using Langmuir Probe (LP) has also been difficult due to low density and flowing nature of the non-neutral plasma [140, 141]. Due to the flowing nature of the plasma the characteristic I-V curve of LP spreads out significantly resulting in long tail. Plasma potential measurement using LP in high impedance mode [50, 55, 57] gets over-estimated as current is never zero at plasma potential, and it becomes reliable only for plasma with densities much smaller than Brillouin density limit [140]. Additionally, it had also been found perturbing the plasma significantly and affecting the confinement of the plasma in earlier experiments of SMARTEX-C [121].

The work proposed in the scope of the thesis promised to take on these challenges to achieve long time confinement of electron plasmas in SMARTEX-C. Following chapter discusses the necessary upgrades carried out in SMARTEX-C.

3

SMARTEX-C Trap, Diagnostics and Sub-systems

Concept of partial toroidal electron plasma trap is to break toroidal symmetry, recreate the cylindrical Penning-Malmberg trap arrangement in the toroidal geometry and produce electron plasma in a "C" shaped region of the trap. Remaining part of the torus is used to accommodate the trapping electrodes and diagnostics. The successful implementation of the concept was demonstrated by Stoneking et al [61] at Lawrence University(LU) in a large aspect ratio torus (LNT-I) and Pahari et al [63] at Institute for Plasma Research(IPR), India in a similar but small aspect ratio torus. The latter was referred to as 'Toroidal Penning Trap'. Since then the trap has been re-christened as *SMARTEX-C*, where the acronym stands for SMall Aspect Ratio Toroidal Electron plasma eXperiment in 'C' shape geometry. This is to distinguish it from the earlier small aspect ratio toroidal trap, in IPR, that trapped plasmas in a full torus [54, 142] and the electrons were introduced through cross-field injection. (The earlier trap is now referred to as SMARTEX-T, 'T' referring to full torus).

Initially, the successful trapping of plasmas in LNT-I was carried out with the aid of toroidal magnetic field and an external radial electric field. SMARTEX-C, demonstrated that the external electric field was not necessary. Subsequent experiments in LNT reconfirmed the same.

SMARTEX-C also reported rich coherent electrostatic wave activity (flute mode). Plasma loss was triggered presumably due to the destabilized mode. Confinement time was also limited due to pulsed magnetic field (4 ms). In other words, the presence of instability and limited B-field pulse duration appeared to be the prime shortcomings in this trap. Important up-gradations to perform long-time, quiescent electron plasma experiments in this partial toroidal trap were therefore imperative and are reported in this thesis. This chapter, in particular, discusses about the experimental set-up, associated sub-systems, operation of the trap and necessary up-gradations carried out. Section 3.1 discusses about the mechanical design of the trap. The experiment is operated in a Ultra High Vacuum (UHV) environment to reduce the electron-neutral collisions, as they contribute to the transport of electron plasma. Measures taken to achieve sustainable UHV environment are described in the section 3.2. Producing the high magnetic field of ~ 1 kGauss for $t > 1\,\mathrm{s}$ is very necessary for controlling the instability and performing the long-time electron plasma confinement experiment. Design of the TF coil and obtained results are detailed in the section 3.3.

Electron plasma experiment is carried out in a '*inject-hold-dump/launch*' or '*inject-hold*' sequence. The experimental sequence is as follows: power supply to toroidal field coil is switched on. When steady B field is established, electrons are injected in the trap(inject), trapped for finite time duration(hold) and are dumped to diagnose the amount of total charge(dump). During the hold phase diocotron oscillations are launched in an otherwise quiescent electron plasma to estimate the line density of electron plasma. All of these are done by Trigger Control System(TCS). It enables synchronized switching of Toroidal Field(TF) magnet power supply, biasing and pulsing of the grid electrodes and measurement of all diagnostic signals on the high speed data acquisition system. Section 3.4 discusses about TCS and control and operation of the trap. Trigger circuit that enables fast switching of electrodes and allows tunable parameters is described in sub-section 3.4.1. LabVIEW® based software for acquiring data from NI PXI data acquisition system is described in sub-section 3.4.2. Destructive and non-destructive diagnostics used in the experiment are described in the section 3.5 with special reference to Capacitive probes (sub-section 3.5.1) and charge collector diagnostics (sub-section 3.5.2). In a destabilized plasma capacitive probes easily registers the electrostatic activity but under controlled conditions the plasma oscillates around equilibrium position and can be described as quiescent. Any signal on the capacitive probe is then well below the noise floor. In such a scenario, externally launching the diocotron mode in a controlled manner offers a means of non-destructive diagnosis of the plasma. Linear(small amplitude) diocotron modes are triggered by applying small amplitude sinusoidal pulses on capacitive probes and are utilized to estimate the total charge of the electron plasma as described in subsection 3.5.3. The chapter ends with a summary (Section 3.6) of all the upgradations carried out towards successful operation and long time confinement in the trap.

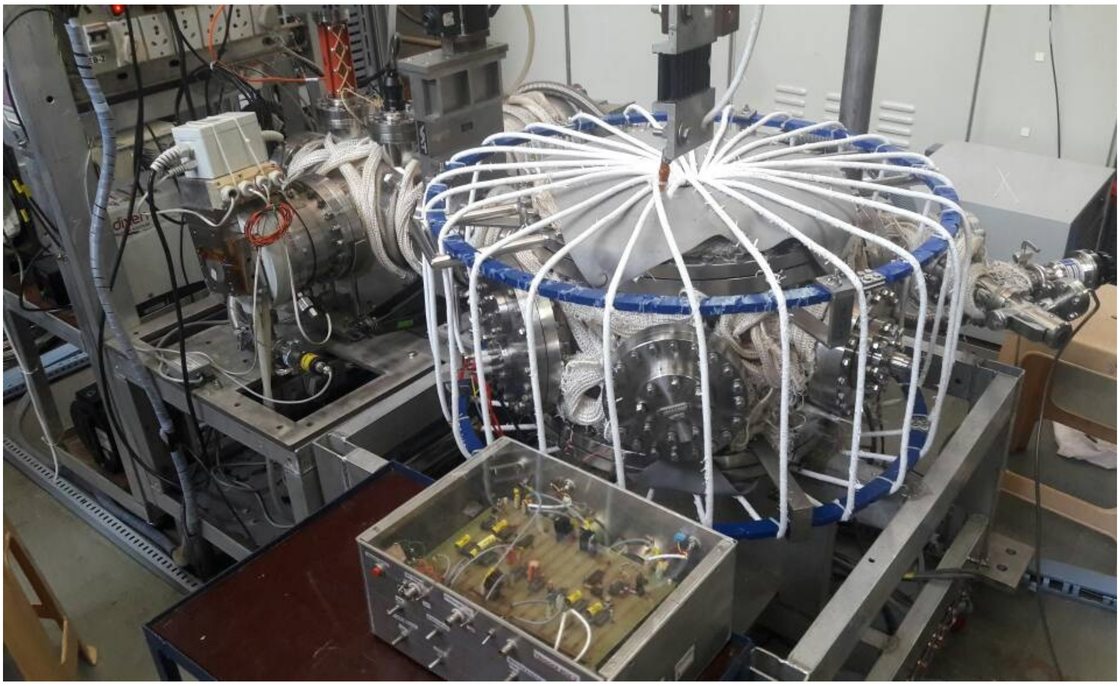

Figure 3.1: Picture of SMARTEX-C: It shows the vacuum pump, toroidal field coil, vacuum vessel, trigger control system and vacuum pumping system.

3.1 Trap: Design

Picture in Figure 3.1 shows the laboratory set-up of SMARTEX-C. The vacuum vessel, pumping system, baking system, toroidal field coil wound around the vessel and trigger circuit for SMARTEX-C can be seen in the picture. Arrangement of components inside SMARTEX-C trap is shown in Figure 3.2. A schematic of the trap is shown in Figure 3.3.

The vacuum vessel is made of Stainless Steel 304 grade. It comprises of a cylindrical vessel of diameter 44 cm and height 32 cm that forms the outer wall of the toroidal trap. The vertically placed cylinder is closed at both ends by circular

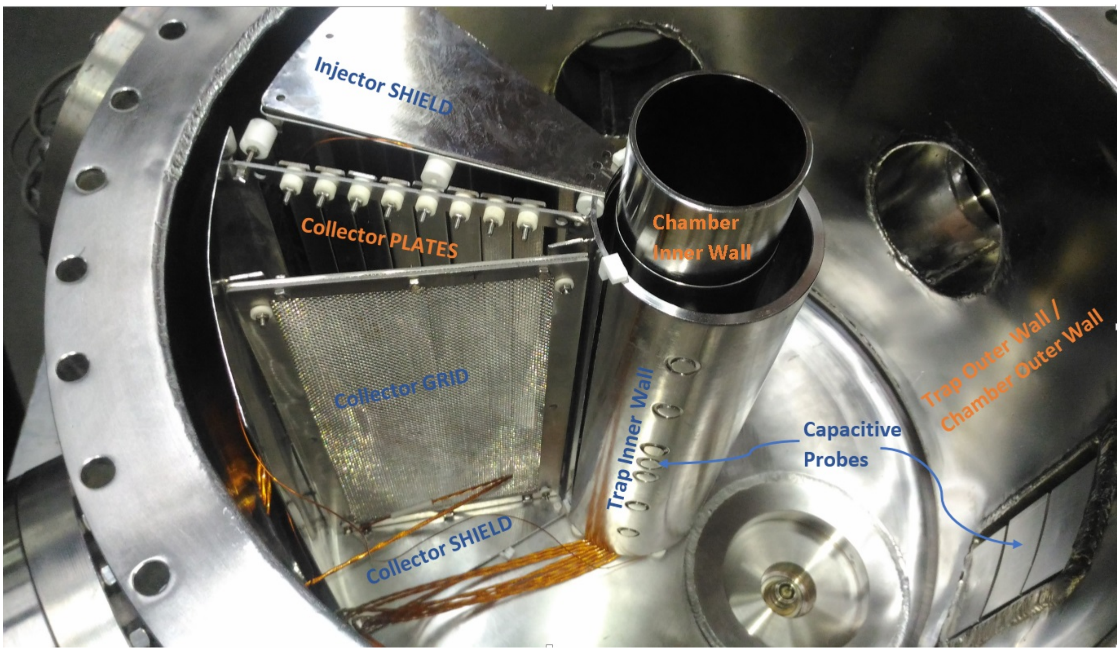

Figure 3.2: Inside picture of SMARTEX-C Trap: It shows the arrangement of trap inner and outer wall, arrangement of capacitive probe diagnostics on inner wall, collector grid, shield and plate placed for the end biasing and diagnostics purpose, injector shield box with injector grid and filament.

removable flanges that form the top and bottom walls. The top and bottom flanges of the cylindrical vessel are sealed using Helicoflex®. Earlier system had aluminum wire seals; in the present system, those have been replaced with Helicoflex. The leak rate is the practically same for both. Helicoflex is easier to install and has a higher success rate. Wire-seals require extreme care during preparation and installation are often seen to fail at the welding joints or due to non-uniformity in the surfaces. A pipe of outer diameter is 7 cm welded to the bottom flange and extends through the top flange forming the inner wall of the vacuum vessel. The sealing between the inner wall and top flange is with the aid of Viton O'ring. This is the only joint in the vacuum system, which is sealed using Viton Oring. It is an easy and low-cost solution as the sealing area is small. Viton Oring was chosen as a sealant as dimensional requirements for Helicoflex are very critical. Baking temperatures are carefully maintained lower in this region due to presence of Viton.

The walls of the vacuum vessel constitute the walls of the trap, except for the inner wall, which is separately formed by a C-shaped cylinder placed concentric with the inner vacuum wall. This inner wall is used to mount the in-board capacitive probes and is also insulated from the other walls. The cylindrical vessel together with the top, bottom and inner C-shaped walls form a small aspect-ratio ($\epsilon \sim 1.6$) rectangular cross-section torus ($R_i = 5\,\text{cm}$, $R_o = 22\,\text{cm}$, height $H = 32\,\text{cm}$) that is used to hold the plasma.

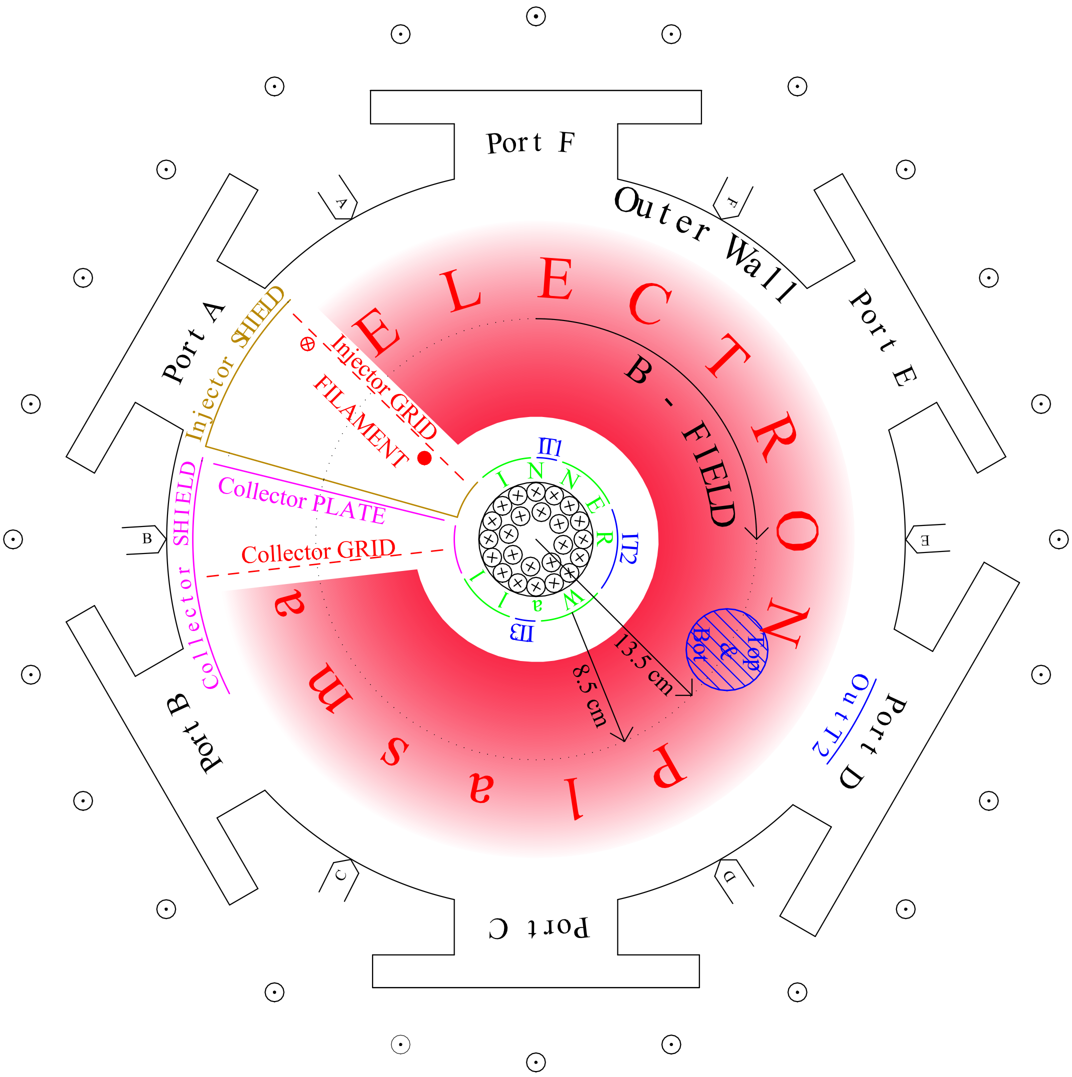

Figure 3.3: Trap geometry and schematic of SMARTEX-C: arrangement of filament, injector grid and collector grid in toroidal section is shown here. Filament and collector grid are electrically separated by a floating conductor placed in between the two. Injector and collector shield boxes are not shown.

The toroidal continuity is broken and is converted into a C-shaped trap by an electrically floating "separator" plate which is placed in a toroidal location (0°) extending over the entire poloidal cross-section. On either side are the Injector module and Collector module occupying nearly $\frac{1}{8}$ region of the toroid. The remaining region (nearing 315°) is used for holding the trapped plasma.

The injector module consists of a circular tungsten filament (10 cm diameter), concentric with the toroidal (minor) axis, that thermionically emits electrons across a grid placed in front. It is surrounded on all sides by an electrically floating shield that restricts the flow of electrons, allowing it only across the grid in front. The gap between the filament and grid is $\approx 1 - 2\,\mathrm{mm}$. The Collector module also consists of a Collector-Grid surrounded by a grounded Shield. Both grids (injector & collector) are made from SS304 with a mesh size of 0.5 mm having physical transparency $> 60\%$. The details of the collector module including its associated electrical circuit and its use as charge collector is outlined in the Diagnostics section later (subsection 3.5.2).

The outer wall has six radial ports (Port A to Port F as shown in Figure 3.3) that allow access to the interior of the trap and are utilized for various diagnostics and pumping requirements. Port B is taken up by feedthroughs to power various electrodes. Port C (with a 100CF six-way cross) is used to host a Non-Evaporable Getter (NEG) pump and BA ionization gauge. It also has BNC feedthroughs to connect up the inner wall capacitive probes. Port D is a 200CF port, that hosts outboard capacitive probes. It also has a fine precision gas-leak valve to allow precise control of neutral pressures. Port E is a diagnostics port utilized to install movable Langmuir probe. The probe has a radial excursion length of $\sim 14.5\,\mathrm{cm}$ and is retracted when not in use. Port F is the main pumping port used for evacuating the trap. The conducting walls of the trap are electrically grounded. Position of capacitive probes, mounted flush with the walls, is shown in the schematic Figure 3.3. Various trap components as described above are carefully aligned and arranged to reduce any asymmetry in the geometry and minimize asymmetry induced transport losses.

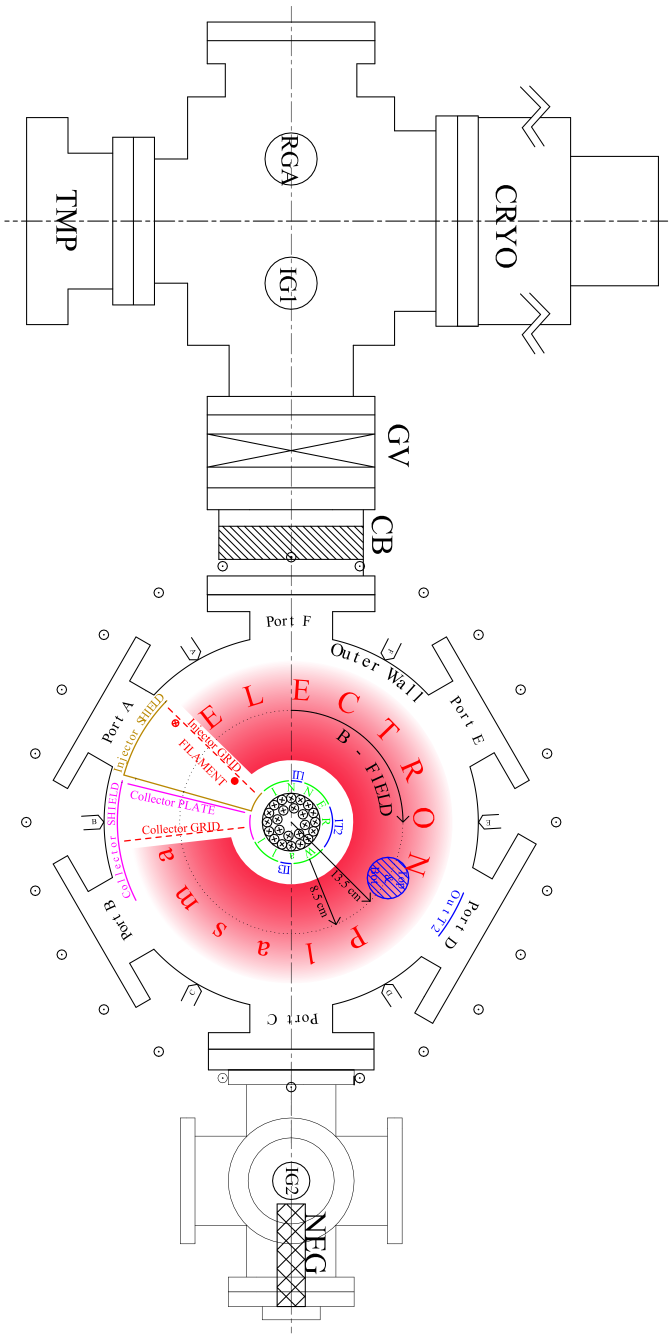

Figure 3.4: Schematic of SMARTEX-C Vacuum System; Turbo-Molecular Pump (TMP), Cryo-Pump (CRYO), Residual Gas Analyser (RGA), Ionization Gauge 1(IG1), Gate Valve (GV), Ceramic Break (CB), Ionization Gauge 2(IG2), Non-Evaporable Gettee pump (NEG).

3.2 Ultra High Vacuum system

To carry out investigations in pure electron plasma, Ultra High Vacuum (UHV) is essential to avoid any neutral/ion contamination. Schematic of SMARTEX-C vacuum system is shown in Figure 3.4. Total volume of the vacuum vessel (including pumping ports) is roughly $\sim 75\,\mathrm{l}$ and surface area is $\sim 15\,000\,\mathrm{cm}^2$ (including trap components).

In-vacuum components with low vapour pressure have been carefully chosen to minimize the system out-gassing. Inner surface of the vessel is machined to three-delta finish ($0.2 - 0.8\,\mu$m) and electro-polished. All the trap-components are electro-polished too. All in-vacuum components are cleaned in ultra-sonic bath with a low vapour pressure liquid before installation to reduce outgassing from contamination.

The trap chamber is connected to Vacuum pumps via a pumping port (port F in schematic Figure 3.4). The pumping port accommodates an electro-pneumatic gate-valve (all-metal seal, bakeable) that is used for pneumatic isolation of the trap. It also includes a DC ceramic break that helps to electrically isolate the earthing of the pump from that of the trap.

UHV pumping system of SMARTEX-C consists of a Turbo-Molecular Pump (TMP)(TMU-521P, Pfeiffer make, $500\,\mathrm{L\,s^{-1}}$), backed by a rotary-vane pump (Penta-35, Pfeiffer make, $34\,\mathrm{m^3\,h^{-1}}$). In addition a Cryopump (CryoTorr-8, CTI Cryogenics make, $4000\,\mathrm{L\,s^{-1}}$), backed by a dry-scroll pump (Adixen make, having speed of $15\,\mathrm{m^3\,h^{-1}}$) is used to mostly pump out H_2O. To utilize the maximum pumping speed of both the pumps, customized pumping cross has been designed which maximizes the conductance. Effective pumping speed at the mouth of the trap is $240\,\mathrm{L\,s^{-1}}$. Additional pumping is provided by Non-Evaporable Getter(NEG) pump (Gamma vacuum make, $400\,\mathrm{L\,s^{-1}}$) which is installed on 100CF six-way cross and is very efficient for pumping light gases like H_2 and He.

The pumping sequence is controlled through a set of interlocks. TMP attains the full speed within 6 to 7 min if there are no leaks in the system. An interlock has been designed between the vacuum pumping system and the vacuum chamber. If TMP fails to attain the full speed, gate-valve trips and isolates the pump. Interlock also prevents the inadvertent venting of the vacuum system in case of a sudden power failure; it prevents venting of the chamber by switching off the gate valve between pumping cross and vessel. A solenoid valve prevents the venting of the turbo pump. These valves will re-open only after a certain time delay after power restoration. As the chamber attains a vacuum of 1×10^{-4} mbar, cryo-pump is switched on which then pumps down the vessel till 8×10^{-9} mbar. At these pressures the residual gas is dominated by the presence of H_2O, N_2 and H_2.

System is equipped with two BA ionization gauges one on pumping port and other on vacuum chamber side. Residual Gas Analyzer (RGA) is mounted on pumping port side to monitor any wall emission occurring during the experiment. Pressure measurements in the system depends upon residual gas composition, geometry of the system and associated pressure gradients. The inaccuracy of the measurements can therefore be of about 30%. Partial pressure analysis of the system has been shown in the Figure 3.5 (dotted line).

Fine precision leak valve is also installed on the vessel to permit the electron plasma experiments at any desired pressures. This also allows the choice of different gas species to investigate any impact of the same in the confinement or instability. Vacuum chamber is also connected to buffer-gas chamber filled with dry-Nitrogen for venting the chamber whenever required. This reduced the pump down time for subsequent campaigns.

3.2.1 Baking System

To attain ultra-high vacuum of the order of 1×10^{-9} mbar and better in the trap region, SMARTEX-C vacuum vessel is uniformly baked at $T = 200\,°\mathrm{C}$ for nearly 48 h. Since the vacuum pumps are always operational (even in case of power failure) and gate valves are open, baking of the entire system ($24 - 48$ h) is required only if the system is being pumped down after venting it to the atmosphere. Glass-wool tapes of 1200 W wrapped around the vessel act as heating elements. TMP and RGA are heated using metal band & silicon rubber based heaters. Cryo-pump is baked to less than 60 °C. 'T' type thermocouples are used to sense the temperature of the vacuum vessel at all radial ports (A to F as shown in Figure 3.4), top & bottom flanges and pumping port. Heater current through individual coils and hence temperature of the vacuum-system can be varied by variable transformer. Temperature is monitored using Massibus make temperature Scanner/Controller. Current of each coil is controlled using mechanical relay switch through this con-

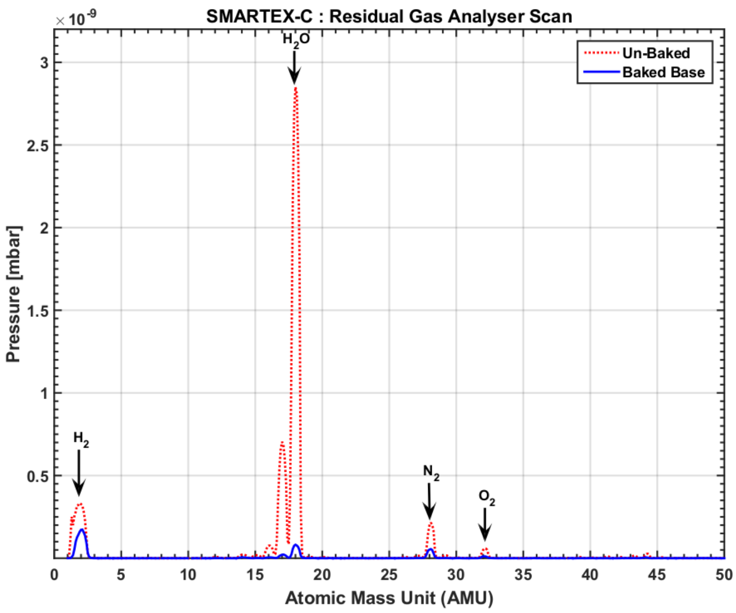

Figure 3.5: RGA scan of different gases during different phases of experiment in SMARTEX-C, Un-baked and baked scenarios.

troller. Controller can trigger the relay switch (Normally Connected(NC) to Normally Open(NO) mode) as soon as temperature of the specific location of vacuum system reaches a set target temperature. Temperature set point can be fixed either manually from controller or through a software. Massibus temperature scanner is interfaced with computer and Scada® based data-logging software is used to log the temperature data. As the current is set manually, rate of temperature increase is not constant throughout the range but our adjustments have led to $< 30\,°\mathrm{C\,h^{-1}}$.

Temperature uniformity on entire toroidal vacuum vessel for $t > 60\,\mathrm{h}$ is demonstrated in Figure 3.6. Top and bottom flanges being thick (higher thermal mass) takes longer time to heat-up to set temperature. Overshoot in the temperature from set values can also be seen in the figure to be $< 3\%$ (less then $5\,°\mathrm{C}$).

RGA monitoring of important gases (i.e. Water vapour, Nitrogen, Hydrogen, Carbon Monoxide and Carbon Dioxide) along with pressure reading of ionization gauges is carried out at two locations (pumping port and vacuum chamber). During the baking cycle water-vapour pressure is observed to increase with temperature and saturates for a brief period at $> 5 \times 10^{-5}\,\mathrm{mbar}$. It then slowly falls and saturates at lower values. As temperature of Cryo-pump increases from 13 K to

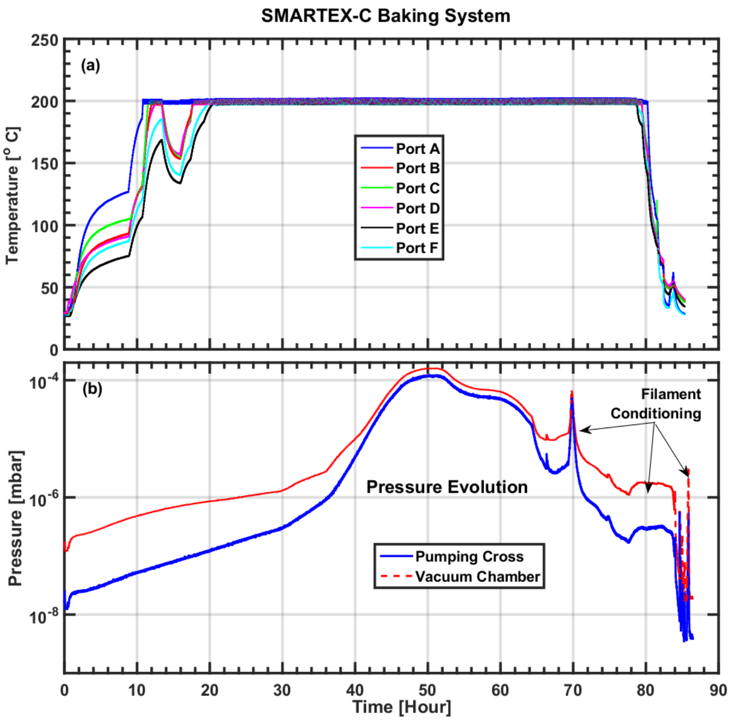

Figure 3.6: Temporal evolution of (a) temperature on all radial ports of SMARTEX-C (b) Pressure.

$45-50$ K, release of Hydrogen from Cryo-pump is observed to increase and then fall off.

After cool-down, chamber achieves a ultra-high vacuum of $\sim 1\times10^{-9}$ mbar. For further improvement a Non-Evaporable Getter (NEG) pump is also used to pump the chamber. This has resulted in ultimate vacuum of $\sim 1-2\times10^{-10}$ mbar at pumping port and $\sim 4-6\times10^{-10}$ mbar range pressure in trap region with filament 'OFF' condition. Most of the experimental work has been carried out in operating range of 1×10^{-9} mbar to 2×10^{-8} mbar pressure with filament ON condition in trapping region. Residual gas analysis of partial pressures of the vacuum chamber in baked system is shown in Figure 3.5.

An important exercise is to carry out baking of in-vacuum components. To achieve this an additional tungsten filament (baking filament) is mounted inside the trap and heated during baking process. Effect of this baking is shown as 'Filament conditioning' in Figure 3.6 and effective base pressure achieved following the conditioning is shown in Figure 3.7 with solid line. RGA scan during the filament

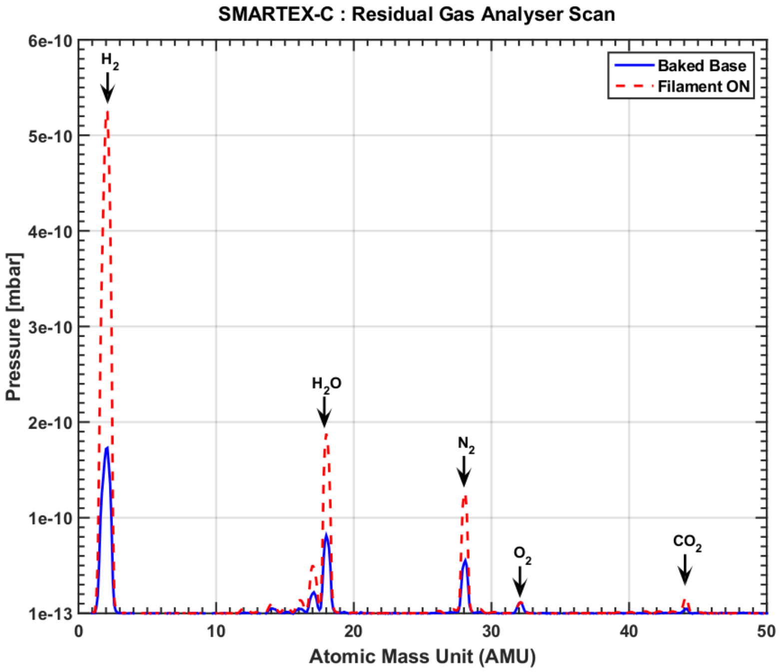

Figure 3.7: RGA scan of different gases during different phases of experiment in SMARTEX-C, baked system and filament ON scenario.

'ON' situation is shown in Figure 3.7 with dashed line. During long-experimental campaigns of few hours, if the injector filament is kept 'ON', heating of the trap components and vessel chamber in and around the injector filament leads to slow but steady rise in pressure(following idea gas law). The rise in pressure is largely due to increase in H_2. Continuous operation of filament leads to increase in out-gassing and higher operating pressure. Wall temperature during this scenario and corresponding time evolution of partial pressure of dominant gases is shown in Figure 3.8. It can be seen that port facing the filament and nearby parts of the vessel get heated up to as much as $\sim 78\,°\mathrm{C}$. As the diocotron mode activity is very sensitive to pressure, this results in an irreproducible plasma when an experimental campaign extends over many shots (few hours). Hence, to carry out experiments under controlled conditions in the range of $1.5 - 2.5 \times 10^{-9}$ mbar and to achieve reproducible plasma, filament is switched 'off' in-between two plasma shots for nearly 15 min. For any further improvement and to ensure long experimental campaigns under filament 'ON' conditions, active cooling of vacuum vessel

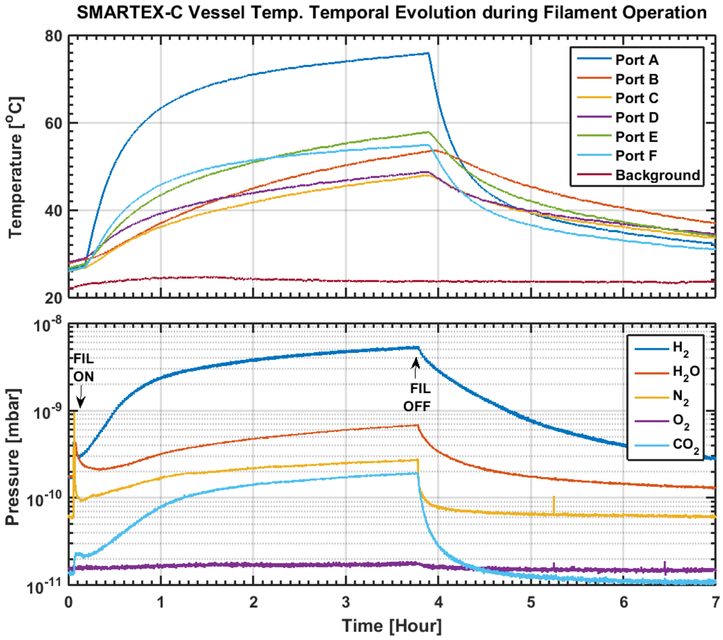

Figure 3.8: Temperature of vacuum vessel at different toroidal location during filament operation. Pressure vs time for different gasses.

is planned for future.

3.3 Toroidal Magnetic Field

In view of the stated objective of achieving long time confinement of electron plasma in SMARTEX-C it was imperative that the toroidal magnetic field was increased both in strength and duration. It may be noted that prior to this thesis the maximum strength of magnetic field in SMARTEX-C was of the order of 300 Gauss and for a duration not more than 10 ms [63, 143], severely limiting the confinement time.

Toroidal magnetic field is obtained using a multiturn toroidal coil. Initial TF coil (Coil-A) was wound of a single AWG 4 wire, having 28 turns. PTFE insulated multistrand silver plated copper conductor was used as a coil conductor and a Pulse Forming Network (PFN) was used to drive the current [144]. PFN is a combination of several inductors(L) and capacitors(C) sections arranged to deliver a current pulse whose pulse length depended upon load impedance and number of LC sections. The PFN was delivering a uniform current pulse of 500 A corresponding to 200 Gauss (Non-uniformity $\sim 10\%$) for 30 ms (flat-top) in Coil-A as shown in Figure 3.9 (black dotted line). TF coil A was operated with PFN and therefor limited to 150 ms. Parameters of Coil-A are given in Table 3.1. Interestingly even in the presence of such a pulsed magnetic field with a droop of 10%, plasma lifetime extended for > 100 ms [137]. Not only did the results indicate an insufficient duration of the B-field, the need for a stronger B-field was also felt to improve and scale the lifetime. However, with the confinement limits being unknown, it was difficult to determine the required magnetic field *a priori*. Around this time the steady state confinement of electron plasma in contemporary traps (LNT-II) was reported to be of the order 3 s, and appeared to be constrained by the Magnetic Pumping transport. The same theory proposed a confinement limit (under theoretical assumption of large aspect ratio) of ~ 2 s for SMARTEX-C. Hence it was argued that a TF coil and Power Supply that could deliver about a ~ 1000 Gauss for at least few seconds could be sufficient.

As an initial upgrade, an intermediate TF coil (Coil-B) having conductor AWG - 6 was designed and the PFN was replaced by a DC power supply primarily to investigate the instabilities and to explore the parameter regime that would allow a quiescent plasma in SMARTEX-C. The DC Power supply had power rating of 100 V and 5000 A for 1.2 s duration. The product $I \cdot \tau$ of the power supply (where

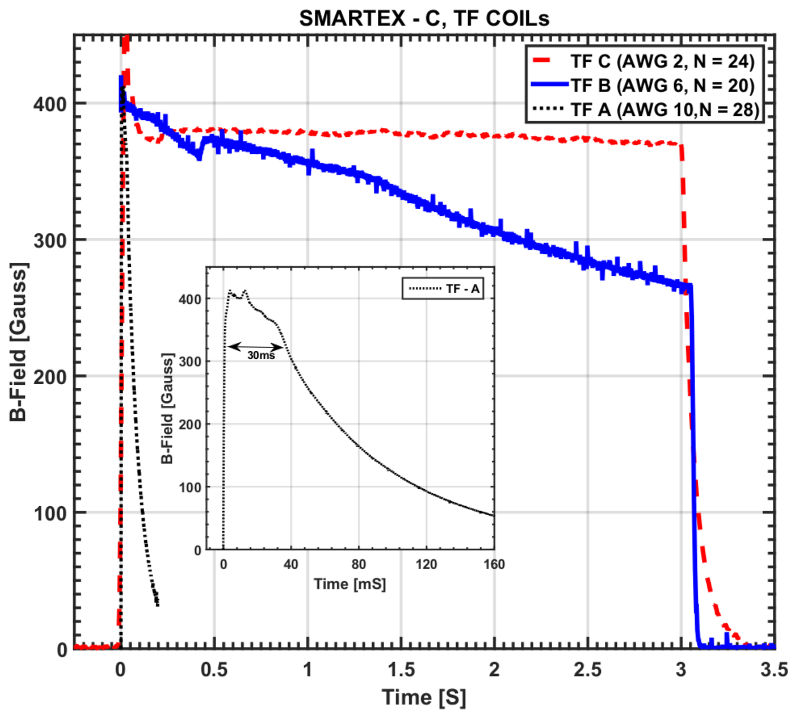

Figure 3.9: Magnetic field pulse TF-A (AWG 10, 28 turn coil-dotted black line) powered using Pulse Forming Network(PFN), TF-B (AWG 6, 20 turn coil-solid blue line) powered using high current, 4.0 s pulsed power supply and TF-C (AWG 2, 24 turn coil-dashed red line) powered using same PS as for TF-B.

I is current and τ is pulse duration) was limited to 6000 A s at maximum voltage rating of 100 V, allowing for current and pulse duration to be set within the range. Parameters of the Coil-B are given in Table 3.1. A typical magnetic field generated for 3 s by Coil-B is shown in Figure 3.9 (solid blue line). Current of (5 kA) was measured using DC shunt(75 mV). The coil was found to be resistive. In-spite of a constant current mode, current drops in the coil due to Ohmic heating ($\sim 42\,^\circ\mathrm{C\,s^{-1}}$) and the voltage limit of 100 V. The drop is around $\sim$ 11%/s at 1300 A (400 Gauss). Droop of $\sim$ 35% in the pulse of TF Coil-B can be clearly seen in Figure 3.9 by the end of pulse. At lower currents (200 Gauss) droop was observed to be less than 5 %/s. In-spite of the droop we found TF Coil-B adequate to carry out most of our experiments towards characterization of instability. These experiments in turn gave us some indication towards the possible extent of confinement and helped us in defining the requirement of the Coil and Power Supply more precisely for extended confinement.

Parameter	TF - A	TF - B	TF - C
Conductor Gauge	AWG 10	AWG 6	AWG 2
Number of Turns	28	20	24
Designed B-Field (in Gauss)	200	400	1000
Pulse Duration	0.03 s	4 s	4 s
Current Source	PFN	DC PS	DC PS
Coil Resistence (R [Ω])	$\sim 200\,\mathrm{m\Omega}$	$\sim 75\,\mathrm{m\Omega}$	$\sim 25\,\mathrm{m\Omega}$
Coil Inductence (L [H])	$\sim 200\,\mu\mathrm{H}$	$\sim 100\,\mu\mathrm{H}$	$\sim 150\,\mu\mathrm{H}$
Heating ($^{\circ}\mathrm{C\,s^{-1}}$)	~ 40	~ 42	~ 30

Table 3.1: Physical parameters of SMARTEX-C Toroidal Filed coil for (A) 200, (B) 400 and (C) 1×10^3 Gauss of magnetic field at trap minor axis.

The droop in B field resulting from the resistive heating of TF Coil-B was ultimately found to limit us in achieving long time confinement and investigation of transport theories. The heating resulted not only in a droop but forced long time interval ($\sim$ 30 min) between two shots to prevent any damage to the coil. This was because the small inner bore of the tight aspect ratio trap, allowed little air cooling of the inboard conductors. To overcome these limitations, TF Coil has been redesigned for SMARTEX-C using a AWG 2 conductor. While the higher conductor diameter > 10 mm reduced heating, the limited bore diameter of the small aspect ratio trap restricted the number of turns. The bore diameter of the vacuum chamber had to be increased from 44 mm to 67 mm. The new bore diameter (67 mm) was able to accommodate $N = 24$ turns of AWG 2 silver plated PTFE insulated multi-strand copper conductor in two circular layers. The radius of vacuum wall was increased but that of the trap inner wall was not altered to keep the aspect ratio unchanged. Therefore the trap components, namely the capacitive probes, insulation, cabling etc had to redesigned to accommodate and support them in the limited space available.

Current pulse in TF Coil-C has been shown in Figure 3.9 with dashed (red) line, where nearly steady current pulse as long as 3 s is observed clearly. For comparision, all the coils have been operated for initial B field of $350 - 400$ Gauss. With resistance of the coil approx. $\sim 25\,\mathrm{m\Omega}$ resistance, droop in the a current pulse is $< 1\%$ helping us to achieve a steady state magnetic field for 4 s. The details of the TF coil (TF-C) is tabulated in Table 3.1. Pulse of different current values of 4 s duration are shown in Figure 3.10. With additional low current

(600 A) low voltage (25 V) supply, the TF coil-C can be used to produce B-field up to 200 Gauss for as long as ~ 60 s. Current pulse for 100 and 200 Gauss is shown for comparison in Figure 3.11.

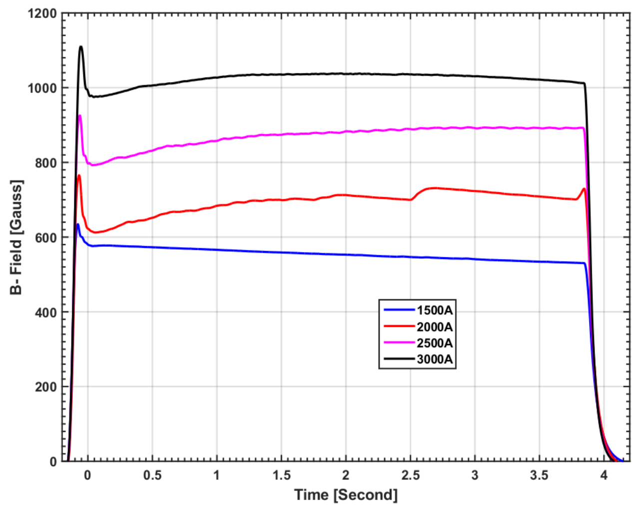

Figure 3.10: Magnetic field current pulses for different B-field strength for new TF coil.

The details of the DC Power supply are as follows. It is a Thyrister based power supply that can deliver 5×10^3 A current at 100 V with maximum pulse duration of 4.0 s at full load *. It utilizes 24 pulse-division technology. Current ripple (in constant current mode) is 2% till 500 A, $< 1\%$ for $500\,\text{A} < I \leq 1 \times 10^3$ A and $< 0.5\%$ for $1000\,\text{A} < I \leq 5 \times 10^3$ A. This ripple is found to cause no significant change in the diocotron mode frequency. Additional low current DC PS is from TDK-Lambda (Model: EMHP-40-600) with temporal ripple $< 0.01\%$.

*Purchased from M/s Gururaj Engineers

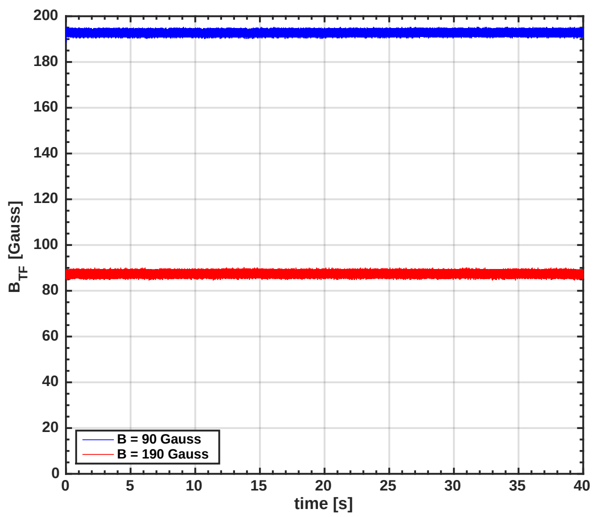

Figure 3.11: Magnetic field current pulses for low B-field strength in steady state condition for new TF coil.

3.4 Operation and Control of the Trap

The electrical arrangement of the trap and its electrodes is shown in the Figure 3.12. The trap is typically operated either in an 'inject-hold-dump' or 'inject-hold' sequence. In addition, a diocotron mode may be externally launched during the 'hold' period. A typical trap operation is as follows. Initially, circular (annular) filament is pre-heated by passing a constant current of 16 A(at 16 V) and is maintained at bias of ~ -250 V with respect to the vessel which is electrically grounded. Choice of circular filament is made in order to minimize the pressure rise occurring due to filament heating in comparison to large spirally wound filament. However, this choice of injector triggers the diocotorn instability in the linear traps, but it would be interesting to investigate this in the presence of non-uniform B-field. Injector grid is held at slightly higher negative potential than the filament (~ -320 V). This prevents the leakage of electrons from the filament to the trap. Collector grid is also biased at -320 V. A toroidal magnetic field of is produced by passing a current through a 24 turn coil at TF_{start} as shown in Figure 3.13. Current pulse duration is set on the DC Power supply either manually or externally through a TTL trigger pulse. After an initial rise time of ~ 120 ms the magnetic field reaches a steady state and the electrons are injected by biasing the

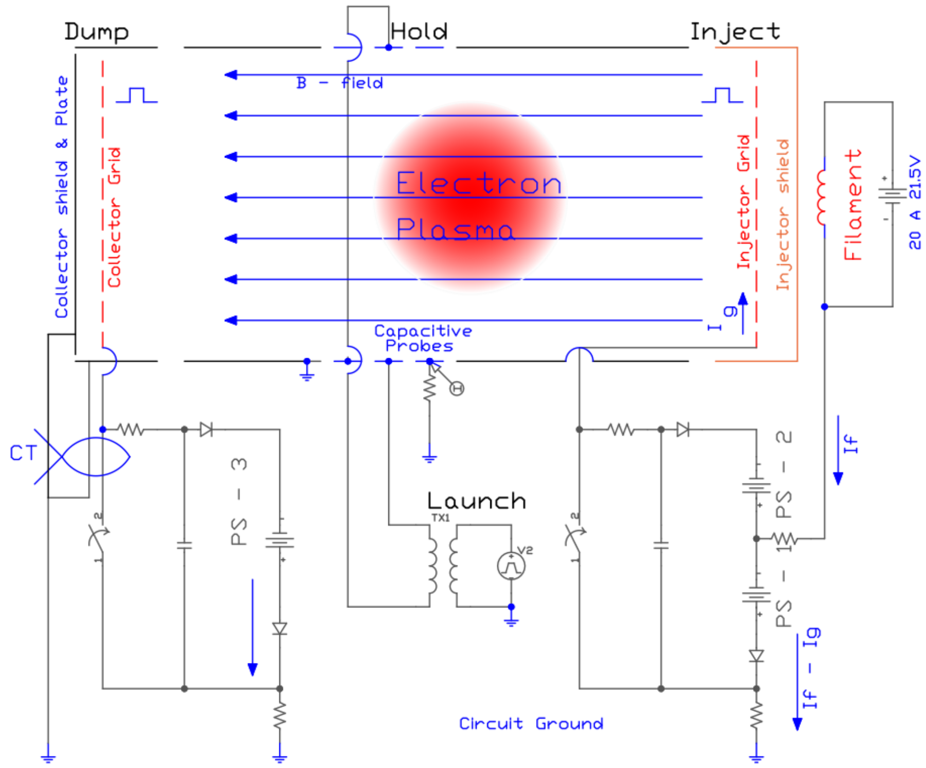

Figure 3.12: Electrical schematic of SMARTEX-C showing various phases of the experiment as inject-hold-dump/launch.

injector grid to ground(0 V) for 60 µs $- \tau_{inj}$ (inject mode) using a MOFET(IRF BC-30) based switch.

Electrons tied to the magnetic field lines in injection phase bounce back from the negatively biased Collector Grid and fill the trap. Injection phase is highly turbulent and dynamics during this period is not yet well characterized. While the initial injection is determined by the filament-grid bias, the trap is expected to fill up quickly and the injection is expected to be cut-off by the space charge potential. At the end of the injection period the injector grid reverts back to negative bias. Now the injected electrons are trapped toroidally between two negatively biased grids (hold mode). The self consistent radial E field in the presence of toroidal B field ensures rotational transform, with the plasma undergoing a poloidal $E \times B$ rotation resulting in a dynamic equilibrium. The duration, τ_{hold}, for which electrons are held in the trap is referred to as the 'hold time'. Any electrostatic activity in the plasma can be observed on capacitive probes during hold period revealing the

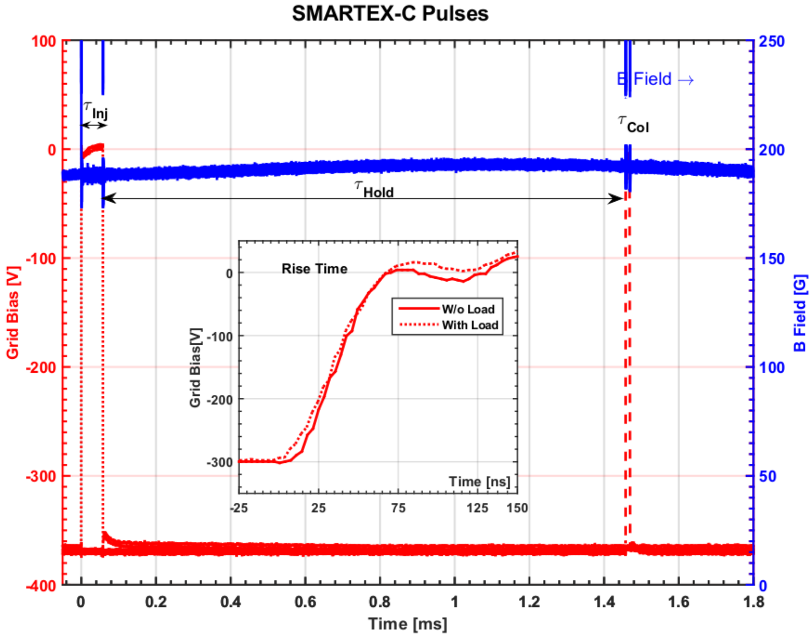

Figure 3.13: Typical pulses on injector grid, collector grid and magnetic field pulses. Inset figure shows the rise time of injector grid with and without load.

dynamics. During the hold period at any instant, the plasma can be dumped onto collector grid to measure the total amount of charge (dump mode). For this the Collector grid is grounded allowing the electrons trapped in the trap at that instant to flow out along the field lines onto the collector assembly. A part of the electrons flows onto the collector-grid and the rest is collected by the collector-shield. Pulsing of the collector to ground is typically carried out for 10 μs and can be delayed with respect to the Injector Grid pulse with a resolution of 1 μs.

A Typical B-field pulse, injector and collector grid pulses are shown in Figure 3.13 (inset figure represents the typical rise-time offered by the trigger circuit). Time-line of various events starting with the triggering of the DCPS, biasing of the electrodes, trapping and dumping of the trapped electrons and the synchronized triggering of the Data Acquisition system is shown in Figure 3.14. Following sub-sections describe the different parts of the control system.

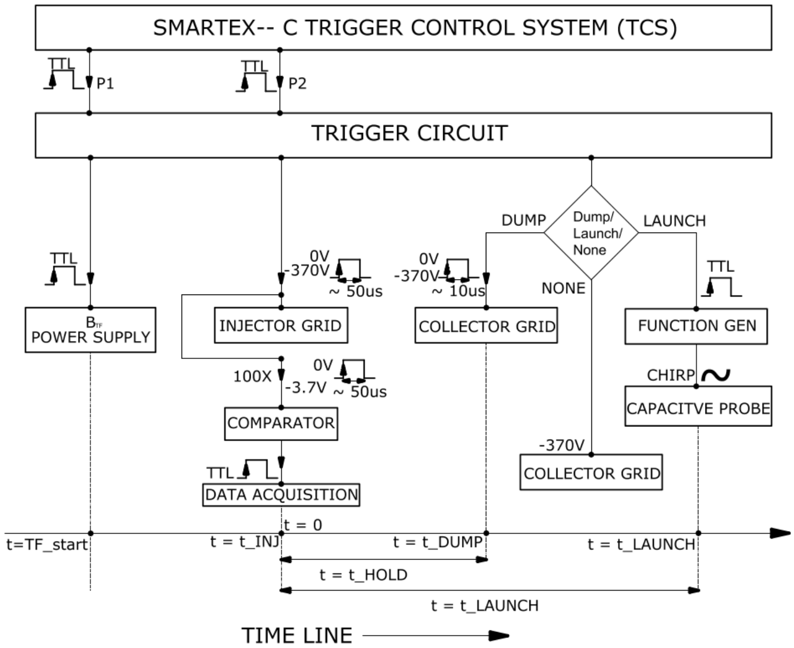

Figure 3.14: Time sequence of the events in the experiment.

3.4.1 Trigger Control System / Circuit

The control of operation is done through a Trigger Control Circuit. It can be triggered either manually or remotely by a TTL pulse generated (using NI-6133 digital I/O card). It allows us to operate the TF-power supply including setting its pulse width (B_{TF}), synchronization of various applied voltage pulses to different electrodes, setting of voltage bias, pulse width and delays. It also helps to launch external diocotron mode and incrementally delay it in every injection-hold cycle.

Two types of trigger circuits have been used. (a) An analog trigger circuit (old) comprising of mono-stable multi-vibrators (74121) to control and set various pulse widths and delays, opto-couplers (MOC3041)and Schmidt trigger (74LS14) for isolation and MOSFETs (IRF BC-30) and their driver (IoR 2112) for switching. It utilizes carefully chosen variable resistors(R) and capacitors(C) to adjust the pulse delays and widths. These components are however prone to thermal drifts over long time usage. Duration of the pulses can be varied with a resolution of $\sim 1\,\mu$s and jitters are in the range of 300 to 400 ns. (b) Digital circuit (new) comprises of a Field Programmable Gate Array (FPGA) utilizing a Microblaze processor and a LabVIEW based user interface to adjust time-delays and pulse widths of the pulses[†]. This offer better flexibility in setting time-delays and widths with minimum settable time of 1 μs with jitters between 10 and 20 ns.

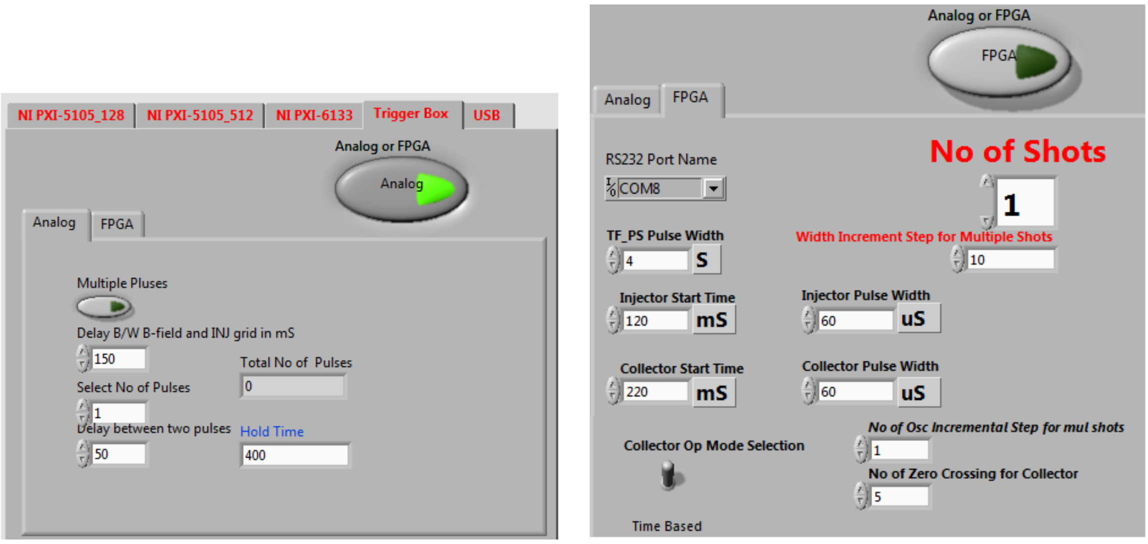

Figure 3.15: Graphical User Interface (LabVIEW based) for multiple shots/triggering of the experiment in a steady DC B-field using Left : Analogue tirgger circuit Right: FPGA based trigger circuit.

In the 'no-load' condition (i.e. grids are not connected), the voltage pulse has a rise time of 50 to 70 ns. When grids are connected, an appropriate resistance is introduced to damp the LC oscillations (L and C being the inductance and capacitance of the cable and Injector/collector grid assembly respectively). The rise time of the pulses increases slightly to 80 to 100 ns which is still much faster than the observed $E \times B$ time scales $\sim 20\,\mu$s. Injection cut-off may therefore be considered to be 'instantaneous'. Collector pulse too is required to be fast to enable instantaneous collection of trapped particles roughly two orders of magnitude faster than diocotron time scale($\sim 10 - 20\,\mu$s); slow rise time reduces the self-electric field causing radial loss of charges thus giving an incorrect information about the trapped charge. Expected flow time scale of plasma is also in similar range.

The injector grid pulse (rising edge) is used as a reference to trigger various electrical subsystems. The pulse on the injector grid is attenuated (by 100x) and used via a comparator circuit (IC LM-311) to generate a TTL pulse. This TTL

[†]Developed by Electronics Division, IPR

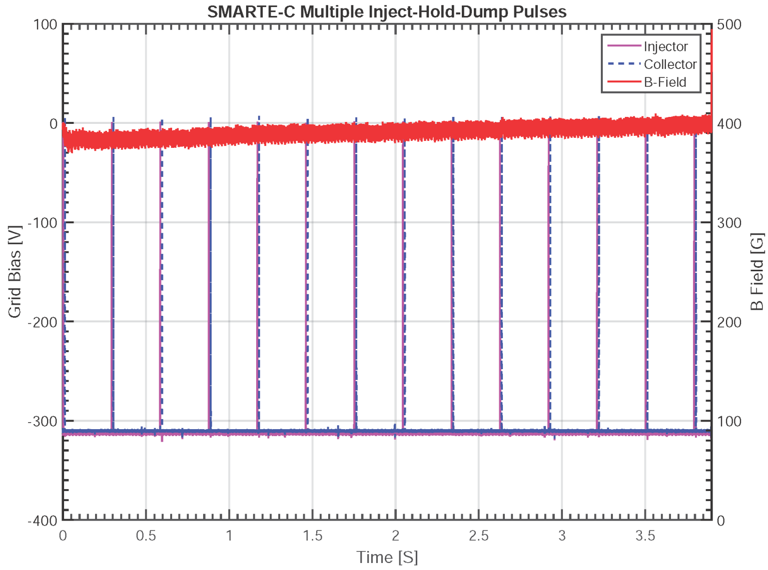

Figure 3.16: Multiple 'inject-hold-dump' sequences of injector grid, collector grid pulses in a steady state magnetic field pulse

pulse is fed to the external trigger-bus of DAQ to start acquisition. The same pulse is also fed to a function generator (Agilent make) to generate a 5 ms burst of sinusoidal pulse for launching the diocotron mode. The mode launch occurs at a desired time instant in the hold phase, with a delay introduced by the function generator. Timing diagram of the entire sequence is shown in Figure 3.14.

The FPGA based trigger circuit has offered several advantages. Multiple 'inject-hold-dump' sequences can be triggered within a single DCPS pulse. A dead time t_{DEAD} of about 50 ms is allowed after each dump to restart the injection of electrons into the trap. Graphical User Menu used to generate multiple pulses(i.e. plasma shots)using analogue trigger circuit and Field Programmable Gate Array (FPGA) is shown in Figure 3.15. The sequence of multiple 'inject-hold-dump' can be repeated during a single magnetic field pulse of 4 s as shown in Figure 3.16. FPGA based trigger-circuit has reduced the thermal drifts and helped in reproducible experiments over long operation periods. It can allow multiple inject-hold-dump sequences with a programmable delay. It also has provision for dumping after a predetermined hold time. The duration of hold can be based on user defined time-delay or a certain number of diocotron oscillations. In the latter case, the oscillations are counted in real-time by obtaining feedback from capacitive probes.

3.4.2 Data Acquisition System

Oscilloscopes have been the main-stay for a large set of experiments and used to acquire the experimental data and transfer it to computers over Ethernet, USB, RS232 etc. With growing number of diagnostics there was need for more channels with diferent bandwidths. The task of synchronization and data handling became tedious as well. The acquisition based upon a dedicated DAQ was therfore conceived with large number of channels, sufficient acquisition rate, storage and front-end integration with a suitable computer program and user interface [145]. A hardware configuration based on the PXI platform was found to fulfill all of these requirements for SMARTEX - C[‡].

The Data Acquisition system (DAQ) includes PXI based data acquisition cards, communication card, chassis, optical fiber link, a dedicated computer, a Trigger Circuit (TC) and a voltage comparator. A comprehensive code in LabVIEW® - 2016 software is developed in order to control the operation of SMARTEX-C as well as to acquire the experimental data from it. The code has been incorporated with features like configuration of card parameters and experimental parameters related to plasma shot. A hardware based control sequence involving TC has also been developed and integrated with the DAQ. In the acquisition part, the data from an experimental shot is acquired when a digital pulse from one of the PXI cards triggers TC, which further triggers the TF power supply and rest of the DAQ. The data hence acquired, is stored in the hard disc in binary format for further offline analysis. In a plasma shot, typical data acquired are information about Toroidal magnetic field $B_{TF}(t)$, filament bias, the injector and collector pulse voltage and duration, frequency and amplitude of diocotron oscillations, the charge collected at dump $q_{coll}(t)$, pressure, wall temperature and other essential experimental parameters. It is also possible to acquire data from multiple plasma shots within the duration of a steady state B_{TF} pulse using the PXI. The specifications of the PXI based DAQ are tabulated below.

Requirement of sampling rate of different channels is listed below and correspondingly they are connected to the DAQ cards.

[‡]Developed by Mr. Yogesh Yeole, NNP-Section, IPR

DAQ Card	Sampling Rate	Channels	Memory	Bit Resolution
NI PXI - 6133	2.5 MSa/s	8 AI & 8 DIO	16 MB	14
NI PXI - 5105	60 MSa/s	8	128 MB	12
NI PXI - 5105	60 MSa/s	8	512 MB	12
NI USB 6109	48 kSa/s	8 AI & 8 DIO	100 kB	14
Agilent DSO	2 GSa/s	4	4 MB	8

Table 3.2: Physical parameters of SMARTEX-C Data Acquisition System.

- Channels that require fast sampling

  1. Acquisition of injector (width $\sim 60\,\mu$s) and collector grid (width $\sim 10\,\mu$s) square pulses (-320 V to 0 V) with rise time $\sim 50-100$ ns equivalent to 10 MHz, sampling rate 30 MSa/s.
  2. Acquisition of the signals from 14 wall (Capacitive) probes with signal frequency i.e., typical diocotron frequency ~ 100 kHz and amplitude ~ 1 mV to ~ 200 mV. High 20 MS/s for harmonic analysis but slow sampling rate 1 MSa/s for Diocotron oscillations

- Channels that require slow sampling

  1. Acquisition of toroidal magnetic field B_{TF} (amplified output of DC shunt from 0 V to 7.5 V) with rise time ~ 100 ms and pulse length from 200 ms to 4 s at a low sampling rate $10kS/s$
  2. Filament current and biasing voltage
  3. Pressure and Temperature of vessel (in order to check the out-gassing from its walls)
  4. Function generator signals

The system includes National Instruments' PXI based system with 64-bit compatible computer interface and has the following modules:

- PXI-8336 (Communication hardware MXI-4, 78 MB/s)
- Fiber-optic link, 10 m, 1.5GB/s
- PXI-1042 (Chassis)

- A computer for operation, control and the acquisition which, works on a Microsoft Windows-7 platform

On-board memory can be shared flexibly only between few channels and recording for higher pulse length as long as 60 s can be made possible as and when required. This system along with the software developed have been integrated with the components of the control circuitry as discussed above.

Fig. 3.17 shows the user friendly Graphic User Interface (GUI) for SMARTEX - C DAQ. The GUI controls the PXI system and all the aspects of the DAQ can be managed from the control-panel. Settable parameters in GUI are(a) Selection of channels (b) Channel names (c) Vertical coupling (d) Vertical range (e) Input impedance (f) Shot duration (g) Sampling Rate (h) Pre-triggered samples (% of total number of samples)and (i) Trigger type and (j) Preset user inputs like name of the experiment, user and other parameters not recorded on DAQ. Default input values entered in the GUI and drop-down menus help the user while entering the input values that are often repeated. Data acquired from all channels are stored in different files, each attributed to one card. Users are also allowed to enter any other data apart from standard inputs. A header file containing set-parameters is created for each shot, which serves useful during offline analysis. The shot number is incremented automatically with subsequent shots. A platform independent, browser based database system has also been developed for easy offline remote query and analysis.

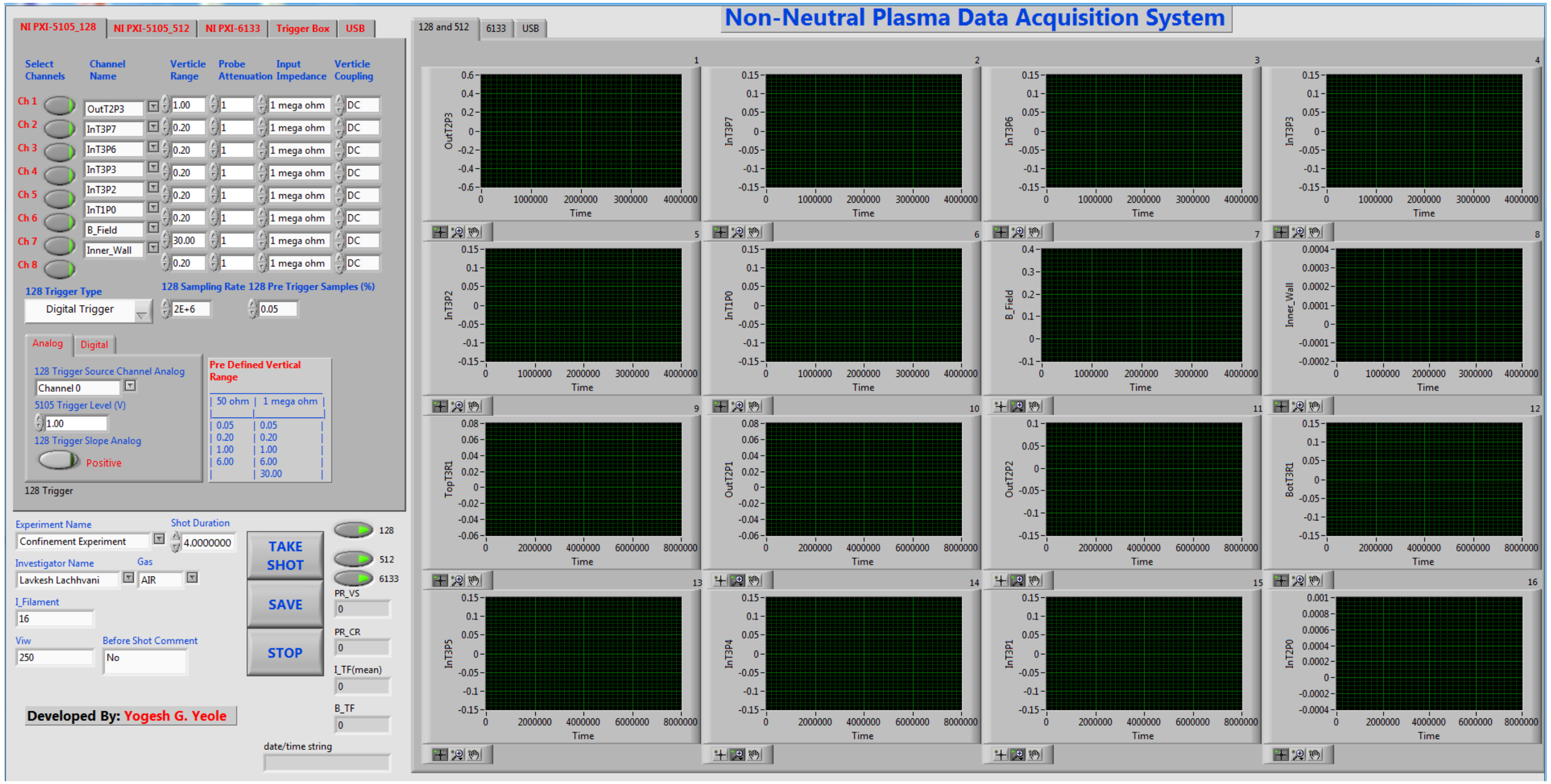

Figure 3.17: Graphical User Interface (GUI) of LabVIEW based SMARTEX-C Data Acquisition System. Panel on left is for user input for various control parameters and panel on right is for visualizing output data from various diagnostics channels and for monitoring purpose.

3.5 Diagnostics

3.5.1 Capacitive probe diagnostics

Any information about the space charge, electric field and dynamics of charge distribution in an electron plasma may be obtained using an electrostatic probe. Such a probe is a small metallic disc or any other shape mounted flush with the plasma chamber walls but insulated from the rest of the walls. It is electrostatically coupled to the plasma and hence also known as capacitive probe. The output signal from the probe is due to the charge induced on it due to the space-charge cloud. As the induced charges flow in and out in response to the space charge fluctuations, the probe can be used either in the charge-sensitive mode or in the current sensitive mode. In the former, the output of the probe is integrated with an integrator having a suitable time constant. The probe signal is proportional to the net charge and the interpretation is straightforward. However, in this case the response of the probe may be limited by the response of the integrator and therefore is used only in low frequency diagnosis. In the current sensitive mode, the current resulting from the flow of induced charges is measured directly across a terminating resistor or with a current transformer or with a I-to-V converter circuit with suitable gain. The recorded currents is then unfolded to obtain information about any plasma dynamics. The acquired current data can also be integrated numerically to obtain the total charge content. Although current-sensitive mode is thought to be more informative, it may prove to be complex as the interpretation and analysis of the current signals requires an appropriate model and expression for the induced current, which in turn is geometry dependent.

Kapenatanakos et al [70] have shown that for two grounded conductors and point charge Q, the instantaneous induced current on one of the conductors can be given as,$i(t) = -\frac{q}{V}E(\rho, v)$, where $i(t)$ is the instantaneous induced current on the conductor, v is the velocity of charged particles and E is the electric field that would be at the position of the particles if a potential V were applied to the conductor and the charged particle were removed. In general, it may be difficult to obtain an analytical expression for E. However, if the geometry is simple, as is the case of say, cylindrical geometries, an analytical expression for E may be derived as shown explicitly in Ref [70]. $i(t)$ is then the explicit expression for induced current on the probe by a point charge and may be unfolded to furnish information about the motion of the particle for simple motions. For example, Ref [70] shows the anticipated wave-forms for a straight line trajectory (along the cylindrical axis) and for a spiral trajectory of a test charge. The equation for i(t) can also be generalized to include distribution of charges and has been obtained for line distribution of charges in Ref [70].

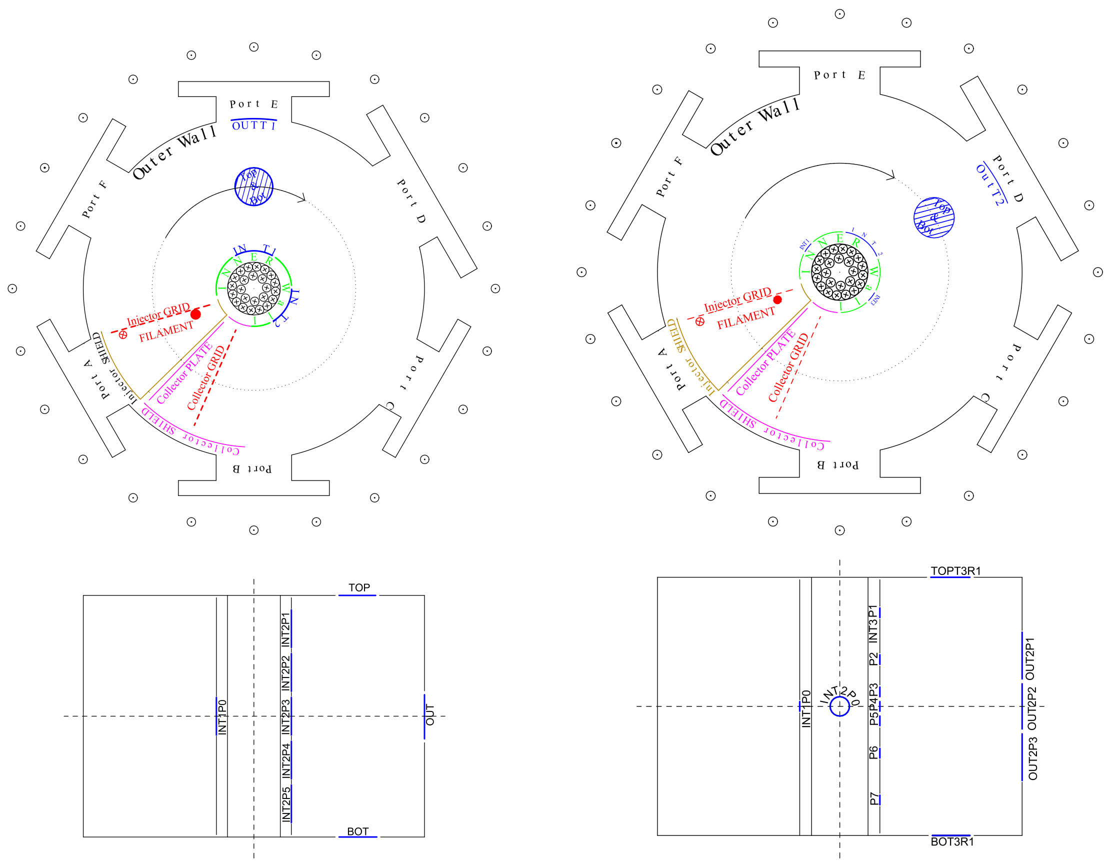

Figure 3.18: (Left) Arrangement of capacitive probes in SMARTEX-C before up-gradation. (Right) Arrangement of capacitive probes after up-gradation, more capacitive probes with fine spatial separation.

Arrangement of the capacitive probes in SMARTEX-C trap before up-gradation is shown in Figure 3.18(left) and after up-gradation is shown on the right of Figure 3.18. Initially, capacitive probes of 50 mm diameter were located on the inboard side at two different toroidal locations, one from 120^o from the injector grid and another five probes at 240^o arranged vertically as shown in Figure 3.18(left). One capacitive probe of 60 mm diameter was placed on outboard side. Probes are machined to have a radius of curvature such that they can be mounted flush with inner wall and insulated using specially designed alumina ceramic bushes. Cross-correlation/cross-phase between any two probes can be used to find the velocity and identify the mode structure in toroidal and/or poloidal direction. The arrangement allowed us to delineate the toroidal or poloidal activity as well as obtain the phase velocity using cross-correlation between two probes. This arrangement however restricted the wave-number analysis of diocotron mode $k_{\perp} <\sim 2.5\,\mathrm{cm}^{-1}$; also large inter-probe separation limited resolution with which phase velocity can be determined.

These limitations were addressed in the up-graded trap. Reducing the probe dimensions on the inboard side and increasing the number of probes on outboard side helped to extend the velocity analysis with enhanced resolution. Small capacitive probes of 12 mm, at various toroidal and poloidal locations are mounted on the inner wall at locations labelled as IT1, IT2 and IT3 as shown in Figure 3.3. IT1 is 53^o away from injector grid location. Probes at IT2 and IT3 are separated by 90^o and 180^o from IT1 respectively. Two capacitive probes are installed each on IT1 and IT2 locations at the mid-plane of the trap. Seven capacitive probes are installed at different poloidal locations(vertically) at IT3 toroidal location. Separation between them is kept in such a way that the velocity on the inboard side gets optimally resolved. This allows a wave-number analysis span of $\sim 7\,\mathrm{cm}^{-1}$ to $\sim 0.54\,\mathrm{cm}^{-1}$. Outer wall of the trap is same as that of the vacuum chamber. Three rectangular capacitive probes ($30\,\mathrm{mm}(H)$ by $60\,\mathrm{mm}(W)$, having same radius of curvature as of outer wall) are mounted on the outer wall. Top and bottom walls also have capacitive probes mounted at minor axis of the trap.

Since the ratio of the surface area of the outboard to inboard wall is significantly greater than 1 in a tight aspect ratio torus, surface charge density induced on inboard side is greater than outboard side for the stored charge Q in the trap (even for a charge cloud placed midway between the walls). One can therefore afford to keep dimensions of capacitive probes on inboard side smaller as compared to the outboard side. Typical capacitive probe signal for a plasma shot in SMARTEX-C is shown in Figure 3.19(a). Inset Figure 3.19(b) offers a closer look at the signal at 15 ms showing large amplitude coherent, double-peaked periodic oscillations. The probe signal exhibits a plasma mode that becomes unstable, grows, saturates and damps in later stages. Amplitude of the signal not just represents the displacement of electron cloud from its equilibrium, but also depends on the geometry, charge distribution and velocity of the charge cloud. Geometry dependent analysis of capacitive probe signals has been carried out for SMARTEX-C, allowing a detailed interpretation of the probe signal and is presented in Chapter 4.

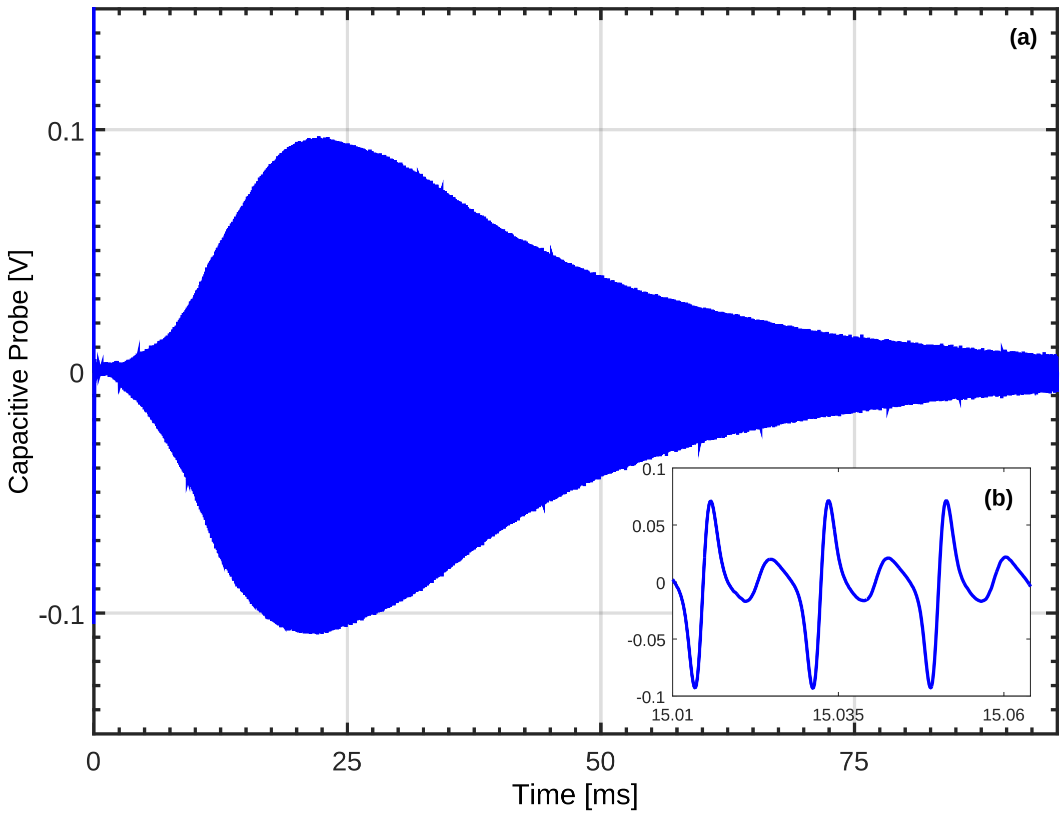

Figure 3.19: Capacitive probe signal evolution with time.

3.5.2 Charge collector diagnostics

A suitable charge-collector has been designed and developed to estimate charge-content of electron plasmas in SMARTEX-C. The electrons are injected and held in the trap with the aid of electrostatic end-fields and a toroidal magnetic field. After a preset 'hold' time the trapped charges are dumped onto a grounded collector (by gating it). As the charges flow along the magnetic field lines onto the collector the integrated current on the collector gives the charge-content of the plasma at the instant of dump. In designing such a charge collector several challenges peculiar to the geometry of the trap and the nature of the plasma are addressed. Instantaneous charge measurements synchronised with the $E \times B$ drift of the plasma, along with fast transit times of electrons (few 100 ns or less) to the collector (due to the low aspect ratio of the trap), essentially require fast gating of the collector. The resulting large capacitive transients alongside low charge content (few nC) of such plasmas further lead to increasing demands on response and sensitivity of the collector. Complete cancellation of such transients is shown to be possible, in principle, by including the return path in our measurement circuit, but the 'non-neutrality' of the plasma acts as a further impediment. Ultimately, appropriate shielding and measurement circuits allows us to (re)distribute the capacitance and delineate the paths of these currents, leading to effective cancellation of transients and remarkable improvement in the sensitivity. Improved charge-collector, has thus been used to successfully estimate the time evolution of the total charge of the confined electron plasma in SMARTEX-C. Complete details of the diagnostics can be found in Ref. [121,139]. Scheme of the capacitive current cancellation has been briefly discussed over here and the schematic is shown in Figure 3.20.

The charge collector is designed as follows: the collector grid is placed inside a conducting shield which encloses it from all sides, leaving only its face exposed to collect the incident electrons. This way the capacitive coupling of the collector grid is largely restricted to the shield around it. Selection of grid over plate as a collector electrode helps further, as the coarse transparency of the grid reduces the geometric-surface area and therefore the capacitance with the surrounding trap components. The grid and shield together forms the charge collector assembly. A voltage bias is applied on the grid. The shield is isolated from the grid and electrically grounded. Importantly, the path from the shield to the ground is distinct from the trap's ground path (see Figure 3.20). A two-core, twisted cable, is used to connect the grid (negatively biased)to the power supply and the shield to the ground. A Current Transformer (CT) is used to measure the total collector current flowing in the two-core cable. Twisted pair also helps in reducing the inductance of the cable and therefore minimizes the ripples in the collector pulse as well as in the current. Additionally, the cables are enclosed in a grounded braid and the CT is placed close to the ground termination for reducing the capacitive pickup.

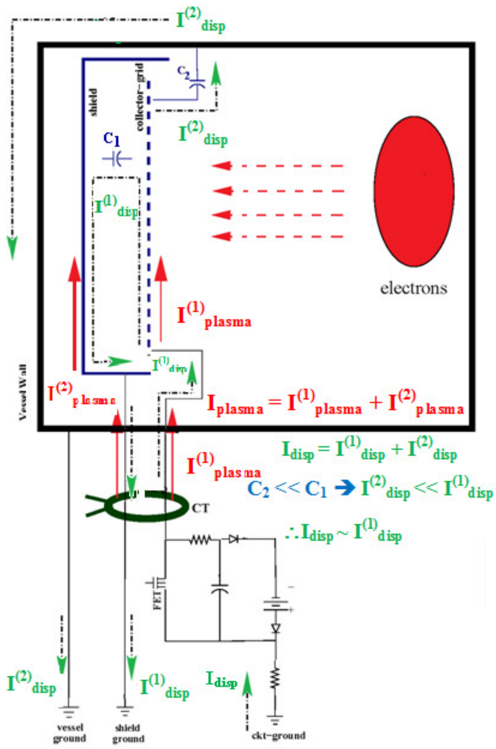

Figure 3.20: Schematic of redesigned collector assembly and electrical circuit.

The illustration in Fig. 3.20 shows the mechanical and electrical arrangement of the collector assembly along with the resultant currents flowing in various paths.

The effect of the shielding is explained as follows. The self-capacitance of the collector-grid, C, is distributed as mutual capacitances between the grid and the shield (C_1) and grid and surrounding trap wall (C_2). We assume C_1 also includes the cable capacitance. Effective shielding of the grid will increase the mutual capacitance of the grid to the shield while reducing its coupling with the grounded walls of the trap, rendering $C_1 > C_2$. When a pulsed voltage is applied on the grid, most of the displacement current will thus be restricted in the path between the grid and the shield. Now, by including the return path of the current (i.e. from the shield to ground) in measurement, the component of the displacement current ($I^{(1)}_{disp}$), flowing between the grid and the shield, is cancelled. Fraction of the total displacement current that gets cancelled, will depend on the relative strength of the mutual capacitances. Due to the limited coupling, C_2, between the grid and the trap walls, only a small component of the displacement current, flowing to the ground via the walls of the trap ($I^{(2)}_{disp}$), remains uncompensated in the measurement of I_{coll}. Interestingly, the measurement of I_{plasma} remains unaffected by this design. Upon gating the collector grid, all of the trapped electrons are either collected by the grid ($I^{(1)}_{plasma}$) or by the shield present behind the grid ($I^{(2)}_{plasma}$). Since both the current paths to the ground are included in the measurement (see Fig. 3.20), transparency of the grid is inconsequential and current measured by the CT represents the total trapped charge collected during the dump.

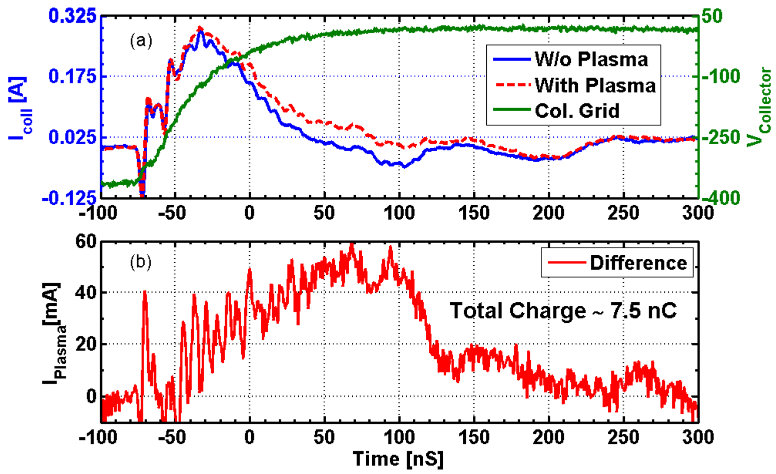

Figure 3.21: (a) Collector current measurement using the current transformer with plasma(red-dashed) and without plasma(blue-solid) during a collector grid pulse (green-solid) rise. (b) Plasma current obtained by taking difference between two signals and integration of same gives the total charge stored in the plasma to be 7.5 nC.

The charge collector assembly with maximally optimized shielding, comprising of the grid and shield, measures the plasma current as shown in Figure 3.21. The negatively biased collector is pulsed to 0 V, first, in the absence of any plasma in the trap and then in the presence of a plasma. The voltage on the collector grid is shown with a solid line(green); the collector currents measured with CT are shown with a solid(blue) line (in case of a shot without plasma) and a dashed line (in case of a shot with plasma). Due to the shielding, the collector current now comprises of I_{disp}, which is a small residual component that flows in a limited path through the grounded trap walls along with I_{cap}, which is approximately

$\approx 15 - 20\,\mathrm{mA}$. In order to obtain the plasma current, I_{coll} is recorded in the absence of the plasma and numerically subtracted from the I_{coll} acquired in the presence of plasma. This effectively removes the components I_{disp} and I_{cap} therein, yielding I_{plasma} of $40 - 50\,\mathrm{mA}$. With a 8 - bit data acquisition system, 50 mA of plasma current can be reliably acquired and extracted from a 300 mA signal with resolution of 26 LSB at an accuracy of $\sim 7\%$. As seen from Fig. 3.21(b), the numerical subtraction with shielding is less noisy than without shielding and the current due to the collected plasma is fairly discernible. Upon integrating I_{plasma}, $\approx 7.5\,\mathrm{nC}$ of charge is shown to be left in the trap at the end of 100 µs. The obtained plasma current has been recorded by producing a new plasma each time and dumping it at the end of different hold duration. Charge computed at the end of each dump provides the time evolution of the total charge trapped in the system. Of course, such a measurement is viable only if shot-to-shot reproducibility of the electron plasma is ensured. Total charge evolution obtained from several such repetitive shots, obtained at a constant pressure of 4×10^{-8} mbar is shown in Figure 3.22(a). It shows that if the plasma is unstable (see capacitive probe data in Figure 3.22(b)) during the hold phase, charges are being lost from the plasma at a very rapid rate.

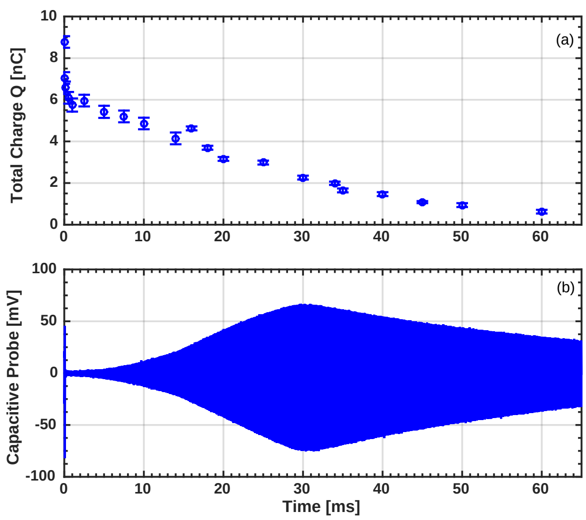

Figure 3.22: Total charge evolution obtained using the charge collector diagnostics at constant pressure 4.0×10^{-8} mbar and B field 350 Gauss.

3.5.3 Externally launched Diocotron mode as a Diagnostics

Dicotron mode oscillations as observed on the capacitive probes in SMARTEX-C are tell-tale signatures of plasma activity. The frequency of the small amplitude oscillations can be related to the line charge density as in linear machines. However if the mode is stable and the plasma is quiescent the oscillation amplitude can be well below the noise floor and no discernable activity is observed on the capacitive probes. In such scenarios, the existence of plasma can be confirmed by dumping the plasma on to the charge collector. An alternate method can be to perturb the plasma in a controlled manner. Assuming linear diocotron mode theory (for cylindrical geometry) applies for small amplitude oscillations in toroidal device too, one can estimate the line density of the electron plasma from the launched diocotron mode frequency for $m = 1$. The linear relation between them is shown in Equation $f_{m_\theta} = f_e[(m_\theta - 1) + (R_p/R_w)^{2m_\theta}]$ [1] where, $f_e = ne/4\pi\epsilon_0 B$ and m_θ is the azimuthal mode number. $m_\theta = 1$ mode is the lowest dynamical frequency for these systems and at small amplitude is proportional to the total trapped charge. At finite amplitude, the $m_\theta = 1$ mode frequency has an amplitude (A_1) dependency given by

$$f_1 = \frac{Q}{4\pi^2\epsilon_0 L {R_w}^2 B}\left(\frac{1}{1 - \frac{{A_1}^2}{R_w^2}}\right) \tag{3.1}$$

Here, L is the electron plasma length, R_p is the radius of the plasma in a cylinder having radius of R_w.

Thus, the launched diocotron mode can be used to estimate the total stored charge. Launch frequency is found using FFT routines on the sinusoidal signals. Accuracy of the method depends upon the number of points used in FFT, with fairly large FFT points, this can be made as good as $\sim 500\,\mathrm{Hz}$ which corresponds to better than $\sim 0.015\%$. Evolution of the total stored charge and the e-folding time can provide information about the confinement time of the electron plasma in the trap. Shot-to-shot reproducibility is a crucial element in estimating lifetime from such multiple shots.

To externally launch the diocotron mode capacitive probes are used as launching antenna (exciter electrodes). $m_\theta = 1$ diocotron mode has been launched in SMARTEX-C, by applying a frequency burst on diametrically opposite probes.

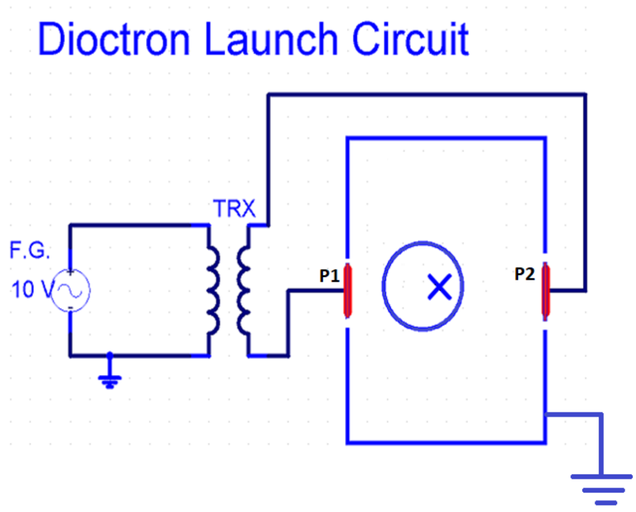

Figure 3.23: Electrical circuit diagram for the diocotron launch technique.

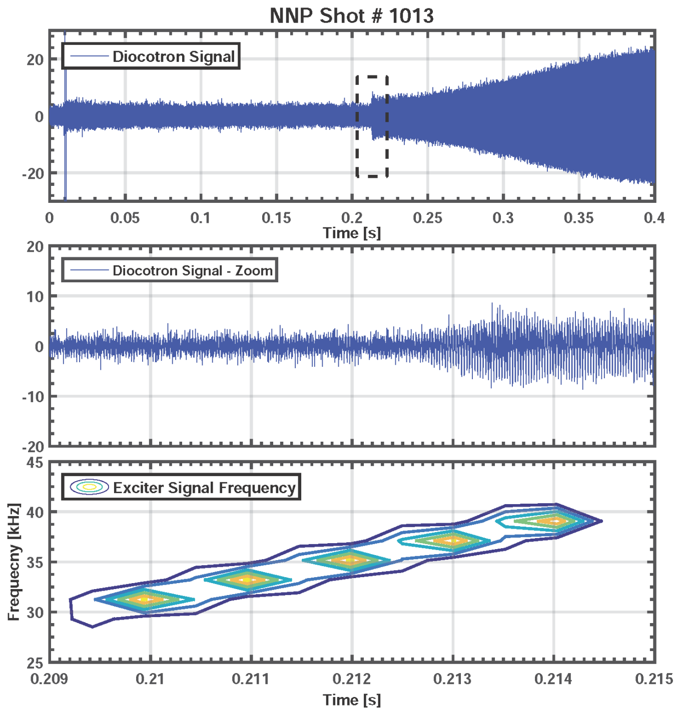

Figure 3.24: (a) Diocotron mode (b) Zoom diocotron mode (c) Frequency of chirping exciter pulse applied on capacitive probes.

Schematic diagram of the diocotron launch circuit is shown in Figure 3.23. Capacitive probes located on inboard side and outboard side at IT2 are used to excite the wave.

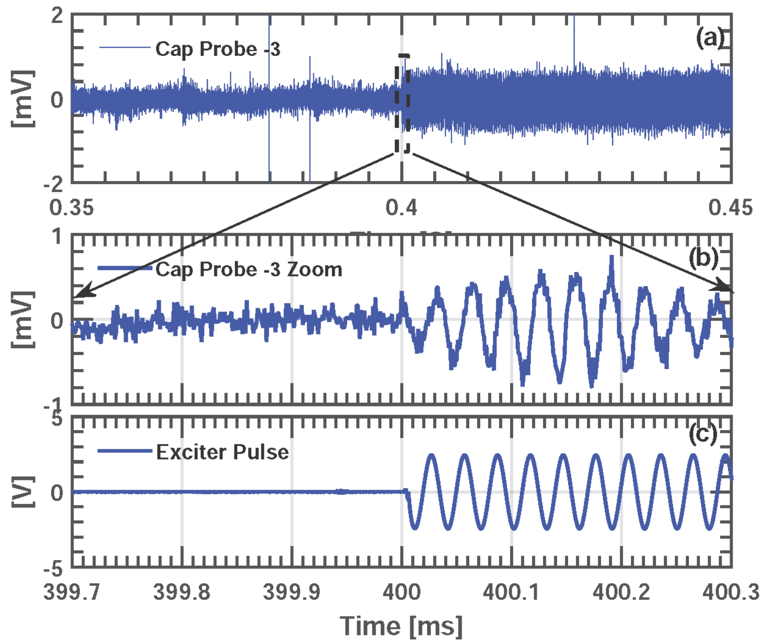

Figure 3.25: (a) Diocotron mode (b) Zoom diocotron mode (c) Exciter pulse.

Mode was successfully launched when an oscillating potential is applied on both the probes with 180^o phase difference. The frequency of the launch pulse has to be carefully chosen so as to resonate with the $E \times B$ rotation frequency of the electron plasma, E being dependent on the trapped charge at the instant of launch. This frequency is selected by applying a frequency chirp to the antenna electrode at the end of a specified hold period as shown in Figure 3.24. Once the frequency of the destabilised linear mode is obtained, a burst of 10 oscillations with $V_{p-p} : 5 - 10$ at that frequency is applied (at the 'hold period') and the linear mode is launched. The amplitude of the perturbation is adequately adjusted so that the mode is not driven to non-linearity. Controlled diocotron launch is shown in Figure 3.25. Complete diocotron mode evolution is shown in Figure 3.25(a), initial zoomed part of capacitive probes is shown in 3.25(b) and exciter pulse is shown in 3.25(c). Many a times it was observed that the plasma got highly destabilized. The frequency of such high amplitude oscillations can not be used to estimate the density as the mode is no-longer a linear mode. Launching of the diocotron mode is very well characterized with the launch signal amplitude, frequency and frequency bandwidth(very narrow, Q_o of the oscillator is very high). Mode gets linearly destabilised if the exciter pulse amplitude is $\sim 4.5\,\mathrm{V}$. Dependency of launch signal amplitude on diocotron launch is shown in Figure 3.26

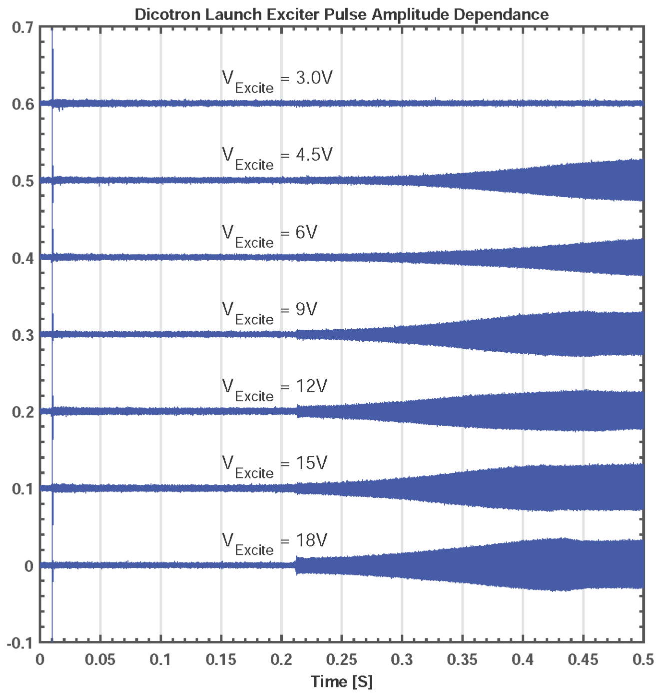

Figure 3.26: Exciter pulse amplitude dependency on diocotron mode launch.

3.5.4 Parallel Temperature ($T_{\parallel}$) estimation : Preliminary

Parallel temperature($T_{\parallel}$) of electron plasma along the magnetic field can be obtained by finding the parallel energy distribution function. It relies on measuring the number of trapped electrons, energetic enough to escape past the applied confinement potentials. This can be achieved in two different ways; (a) Evaporative technique and (b) Two-Stage Dump technique. In evaporative method, the charge collector voltage is ramped up slowly to ground ($V = 0$ in $\sim 1\,\mu$s) and the current is measured due to falling charges on the charge collector (grid + shield). Number of charges that escape are obtained, as a function of the potential barrier, by integrating the current signal. If the distribution is Maxwellian, then on log-log scale the charge versus voltage plot will be linear and the slope can give us the estimation of parallel temperature ($T_{\|}$) of the electron cloud. Such an estimate is shown in Figure 3.27.

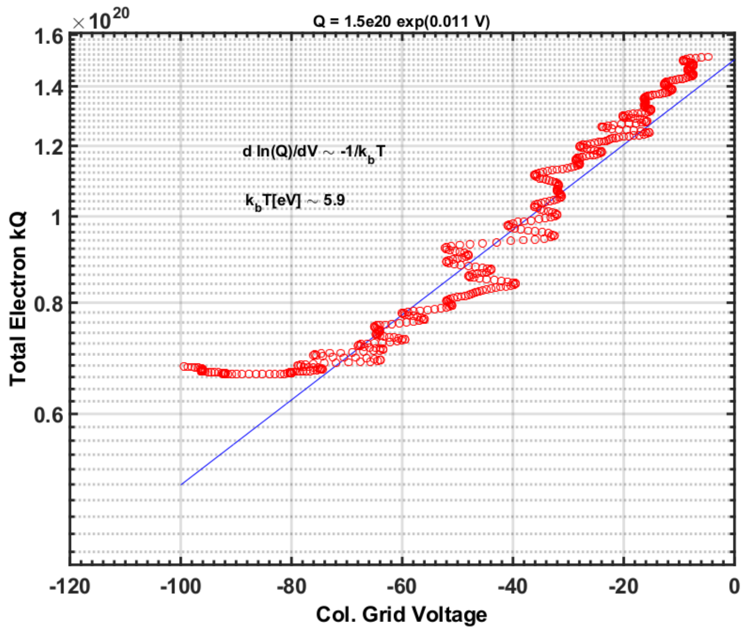

Figure 3.27: Preliminary estimation : Parallel temperature of electron plasma in SMARTEX-C

There are several underlying assumptions and limitations of the technique as adapted here. The plasma is assumed to be in thermal equilibrium and Maxwellian. Second, it is assumed that collection of electrons overcoming the bias potentials is based on their energy distribution and not influenced by their proximity to the collector. To achieve this, the linear machines use separate gating electrode while the collector is placed away at a distance large enough comparable to the length of the plasma (so that all the electrons travel nearly the same distance). This has not been possible in SMARTEX-C. Thirdly, being a non-neutral plasma, it is likely that the electrons will be having a larger component of potential energy as compared to the kinetic energy; when this plasma is dumped on the collector, the potential energy gets converted to the kinetic energy and thus gives an incorrect estimation of T_e. To account for this, the linear devices generally correct the measured temperature by a factor which is determined by a PIC simulation code accounting for the plasma potentials, time dependent vacuum potential and energy exchange between different translational degrees of freedom and conversion of potential energy to kinetic energy. No such correction has been carried out in the SMARTEX-C.

Ideally a dump should be carried out in two stages. First dump should be carried out at intermediate step potential V and second at the ground potential. Intermediate step shall be incremented by multiple small steps (i.e. $\sim 5\,\mathrm{V}$) at every shot. If the gating pulse is kept slow enough, the effect of proximity of collector can be partly nullified. The dump at intermediate step is used as an energy analyser. The second step collects the remaining charges giving the spatial density distribution of these trapped charges. The density profile is used to calculate the potential distribution. At every step this gives the corrective factor for conversion of P.E. to K.E., allowing us to obtain the full distribution function and estimation of temperature with least error. The technique is evidently cumbersome, time consuming, requires additional numerical calculations at every step to obtain temperature information and excellent shot-to-shot reproducibility. Either the improved two stage dump temperature diagnostics [146] [147] or by measuring thermally excited fluctuations [148,149] or normal Trivelpiece-Gould modes of the toroidal electron plasma [150] system can corroborate the temperature.

Temperature estimation in SMARTEX-C, in-spite of the above stated limitations, is approx. 5.9 eV as shown in Figure 3.27 and may be regarded as an upper limit on the temperature.

3.5.5 High Impedance Langmuir Probe

Obtaining plasma parameters in NNP i.e. plasma potential Φ_p, temperature T_e using Langmuir Probe (LP [151]) has been difficult due to low density, low cross-field tansport and flowing nature of the non-neutral plasma [140, 141, 152]. Due to the flowing nature of the plasma the characteristic I-V curve of LP spreads out significantly resulting in long tail. In flowing electron plasma, the distribution function in the laboratory frame is always non-Maxwellian even if the plasma is at thermal equilibrium. Plasma potential using LP in high impedance mode [50,55,57] gets over-estimated as current is never zero even when probe floats at plasma potential. It becomes reliable only for plasma with density much smaller than Brillouin density limit [140], i.e. when the flow energy is much smaller than the electrostatic potential energy of the electron plasma. Additionally, probes are also found to perturb significantly and affecting the confinement of the plasma in earlier experiments of SMARTEX-C [121].

Floating potential (self electric potential) of the electron plasma in SMARTEX-C is measured using a Langmuir probe of very thin tip in high-impedance mode. Tungsten wire of 0.5 mm diameter and 5 mm length is used as a probe, which is inserted using alumina ceramic tube. Probe can have a radial excursion length from $r = 7\,\mathrm{cm}$ to $r = 22\,\mathrm{cm}$. Potential measurement is carried out using OP-AMP (OP-37) in inverting mode offering high impedance to plasma such that it draws as little current as possible. Measurement of the potential is done by keeping attenuation factor of 10. There is a probability of the probe shaft getting charged up due to pickup of flowing electrons by the ceramic tube, this would affect the dynamics of the plasma. Results of measuring potential profile are very preliminary and we have refrained ourselves from measuring potential in most experiments as any electrostatic perturbation to the plasma heavily disturbs the electron plasma and its lifetime gets adversly affected as reported by previous researchers [121].

3.6 Conclusion

The SMARTEX-C trap and all its subsystems have been re-designed and developed keeping in view the demands of long-time confinement of electron plasma experiments in the trap. Vacuum system has been upgraded to achieve Ultra-High Vacuum of $\sim 1 \times 10^{-9}$ mbar to minimize the interaction of electrons with background neutrals to avoid any ion-driven instabilities to improve the confinement time. Toroidal magnetic field coil has been upgraded to achieve strong magnetic field of $\sim 9 \times 10^{2}$ Gauss with a pulse length of 4 s, this also allows to operate the TF coil at lower B fields for steady duration of 69 s. Sufficiently high B-field strength or very low pressures lead to the suppression of the instability by refraining the plasma from meeting the resonance conditions for instability driven by ions. These steps are crucial to lead the experiments of long-time, instability free electron plasma experiments in SMARTEX-C. New trigger circuit has been developed, which incorporates the multiple 'inject-hold-dump' (plasma shots), feedback based (from diagnostics) charge dump to obtain the reproducible charge collection and also synchronizes the NI PXI based data acquisition system. The multi-channel data acquisition system has been developed keeping in mind the large number of operational parameters and diagnostics of different bandwidths to be acquired over a period of long confinement time of few seconds. Diagnostics like charge collector has been redesigned to bring highly reproducible charge collection data and capacitive probes has been re-designed to obtain clear mode structure of the diocotron mode with improved spatial resolution. Diocotron mode launch technique(diagnostics) has also been developed for a quiescent plasma to estimate the confinement time of electron plasma.

Below we have summarized the upgrades carried out as a part of the thesis work.

- Vacuum : Base vacuum of the system has been upgraded to 1.0×10^{-9} mbar and operating pressure is 1.5×10^{-9} mbar (filament 'On' condition.

- Magnetic field : TF coil has been designed for 9×10^{2} Gauss magnetic field for steady 2.5 s pulse duration and at 200 Gauss for nearly 60 s duration.

- Diagnostics : In addition to improvements carried out in charge collector diagnostics (signal-to-noise ratio) and capacitive probe diagnostics (spatial resolution), externally launched diocotron modes have been perfected as a non-destructive diagnostic and successfully used to measure the lifetime in a quiescent plasma.

- Electronics, Control and Data-Acquisition System : New FPGA based trigger-box has been developed, which has lower jitters, capability of taking multiple shots in single B-field pulse duration and real-time feedback of number of diocotron oscillations to trigger charge dump. In addition to this, new PXI based high-speed multi-channel, data-acquisition system for acquiring data over long-time confinement has also been integrated with experimental system.

4

Investigation of Diocotron Modes in SMARTEX-C

4.1 Introduction

Diocotron modes are of ubiquitous presence in electron plasmas. In its simplest form, seen in cylindrical machines, the small amplitude (linear) $m = 1$ diocotron mode [1, 21, 81] is a centre-of-charge motion, of a charge cloud displaced from its equilibrium position undergoing stable $E' \times B$ drift about the axis of the trap, due to electric fields (E') from non-uniform distribution of image charges on the grounded trap-walls. These modes are detected through wall probes that are placed on the walls of the trap insulated from the rest of the walls. They are also referred to as capacitive probes as they are capacitively coupled to the plasma. Cylindrical non-neutral plasmas have utilised such wall patches to investigate the waves and transport activity [25], excitation of waves to diagnose & manipulate [73] and investigate dynamics [74–76] of non-neutral plasma.

A useful property of the diocotron mode as shown by the linear theory, is the dependency of the mode frequency upon the line density rather than on the radial density distribution. This fact has been exploited as a non-destructive diagnostic of electron plasmas whereby the frequency of the launched $m = 1$ diocotron mode has been used to estimate the line density of the plasma [25]. As the mode becomes nonlinear [77, 153], mode frequency becomes dependent on the displacement of charge cloud from trap center and has been utilized to find the displacement in some of the cylindrical traps [10, 78–80, 154].

Toroidal versions of these diocotron modes, have been earlier reported from experiments in both LNT-I [61] and SMARTEX-C [155] though not well characterised. In the absence of any theoretical framework of toroidal diocotron modes, linear theory of cylindrical diocotron modes has been assumed valid for toroidal geometry in the large aspect ratio limit. Accordingly, these linear, small amplitude diocotron modes have been utilized in estimating the line density of electron plasma in several toroidal traps too. [50, 52, 64]. However, it is a matter of debate whether theoretical approximations that relate the large aspect ratio toroidal geometries to cylindrical geometries remain valid in the limit of small aspect ratio too.

In SMARTEX-C, a small aspect ratio toroidal trap, the diocotron oscillation manifests itself as "double-peak" signature-oscillations on the capacitive probe. Simultaneous appearance of significant number of coupled harmonics, with dominance of $m = 2$, had been reported earlier [63]. The growth in oscillation-amplitude was also observed and reported [122] to be due to rapid destabilization of the mode. The evolution appears complex and non-linear and the charge cloud dynamics has been in the realm of speculation. While the actual dynamics can be best confirmed by imaging diagnostics, we demonstrate that the existing capacitive probes too can be utilized, to a great extent, to infer the charge cloud dynamics non-perturbatively.

In this chapter we attempt to de-construct the observed signal on the capacitive probes in terms of charge cloud trajectory. An expression of the image current flowing through probe is derived for a given motion of point charge, based on the Green's reciprocation method [156]. The radial position, the poloidal velocity, frequency of evolution and charge content of the cloud are essential to compute the image current and are obtained from experimental data and provided as inputs. Resulting probe signals for various possible trajectories of a point charge are then numerically generated. A limited set of wall probe data obtained from SMARTEX-C is interpreted using this method. Assuming a monopole, a combination of evolving trajectories is intuitively guessed for a point charge that nearly reproduces the signal and its Fourier harmonic structure with experimentally obtained signal from a single probe. Although the approach is heuristic, it is seen to be effective and throws up the possibility of a vortex-like dynamics, underlying the transition from small amplitude sinusoidal oscillations to large amplitude, double-peak oscillations that is so distinctly observed in SMARTEX-C. It may be noted that the equilibrium configuration corresponding to two vortex was also predicted by solving Levy-Daugherty equation for specific potential profile by Purvi et al [54] and has earlier been shown possible in simulations [42, 157].

The chapter is arranged as follows: Section II describes the probe signal observed on the wall probe diagnostics and its evolution in time, emphasizing the transition from a small amplitude, linear oscillations to non-linear, double peaked oscillations. In section III expression for induced charge on various capacitive probes is derived analytically for a 2-D geometry having rectangular cross-section. Signals are then simulated for various possible test charge trajectories. In Section IV the vortex-like dynamics in SMARTEX-C is interpreted from wall probe data using the technique. The results have been summarized and discussed in Section V.

4.2 Experimental Observations of Diocotron Mode

As discussed in Chapter 2 capacitive probes are located at different toroidal and poloidal locations: two placed diametrically opposite at toroidal angle $\Phi = 120^o$ and eight placed poloidally at $\Phi = 240^o$ (measurement of toroidal angle Φ is with reference to injector grid plane). These are mounted flush with the walls of the trap, insulated from the rest of it. The probes are grounded through $1\,\mathrm{k\Omega}$ resistors and image current flowing back and forth is measured through it.

Time evolution of a typical capacitive probe signal, during the 'hold' time, for experiments performed with Nitrogen as background gas at a pressure of 1.0×10^{-8} mbar and in a uniform magnetic field of ~ 210 Gauss, is shown in Fig. 4.1 (a). Oscillations appear soon after injection, grow to large amplitudes, largely driven by ions [143], non-linearly saturate and then gradually decay. Coherent, periodic, "double-peak" oscillating signal seen on the capacitive probes (Fig. 4.1 (b)) are the signature oscillations observed in SMARTEX-C. Two toroidally separated probes (at 120^o and 240^o on inboard side) register equally large signals that are synchronous; cross correlation of these probe signals confirms that $k_{\parallel} = 0$. On the other hand, poloidally separated probes show a phase delay, with oscillations on probes placed poloidally opposite (on the inboard and outboard side) showing

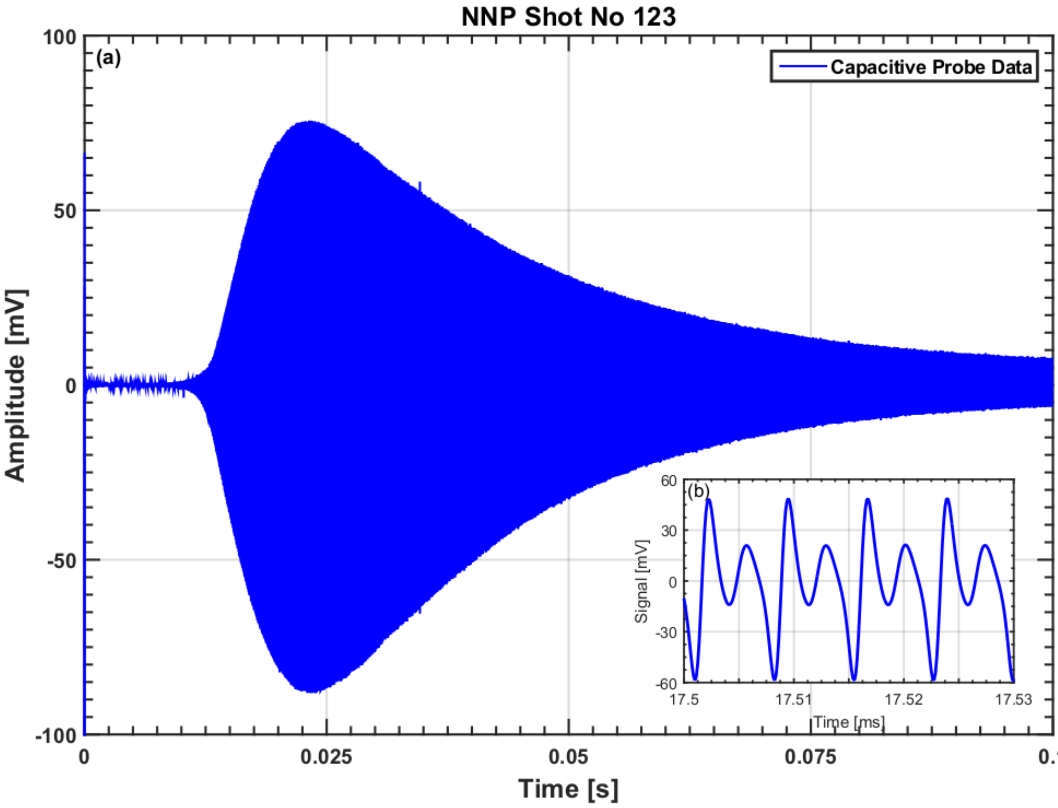

Figure 4.1: Time evolution of (a) capacitive probe signal for a charge cloud trapped with a magnetic field of ~ 210 Gauss. (b) Coherent, periodic, large amplitude double peaked oscillations (Zoomed).

a phase difference of 180^o. All of these suggest a flute-like mode, analogous to diocotron modes in cylindrical machines.

The growth of oscillation amplitude has been arrested in recent experiments [122, 143] allowing one to observe the transition of mode oscillations from small amplitude, linear, near-sinusoidal to large amplitude (non-linear), double-peaked oscillations. The transition in oscillations is shown in Fig. 4.2 (a1 - d1) and corresponding Fourier transform in Fig. 4.2 (a2 - d2). FFT has been carried out by taking 8192 points giving frequency resolution $< 1\,\mathrm{kHz}$ as data is sampled at 10 MSa per second. Initially mode oscillations have single dominant frequency of $\sim 48\,\mathrm{kHz}$. As mode evolves, nearly sinusoidal oscillations distort with appearance of higher harmonics.

An intuitive model was proposed by Pahari *et al* to explain the “double-peak”

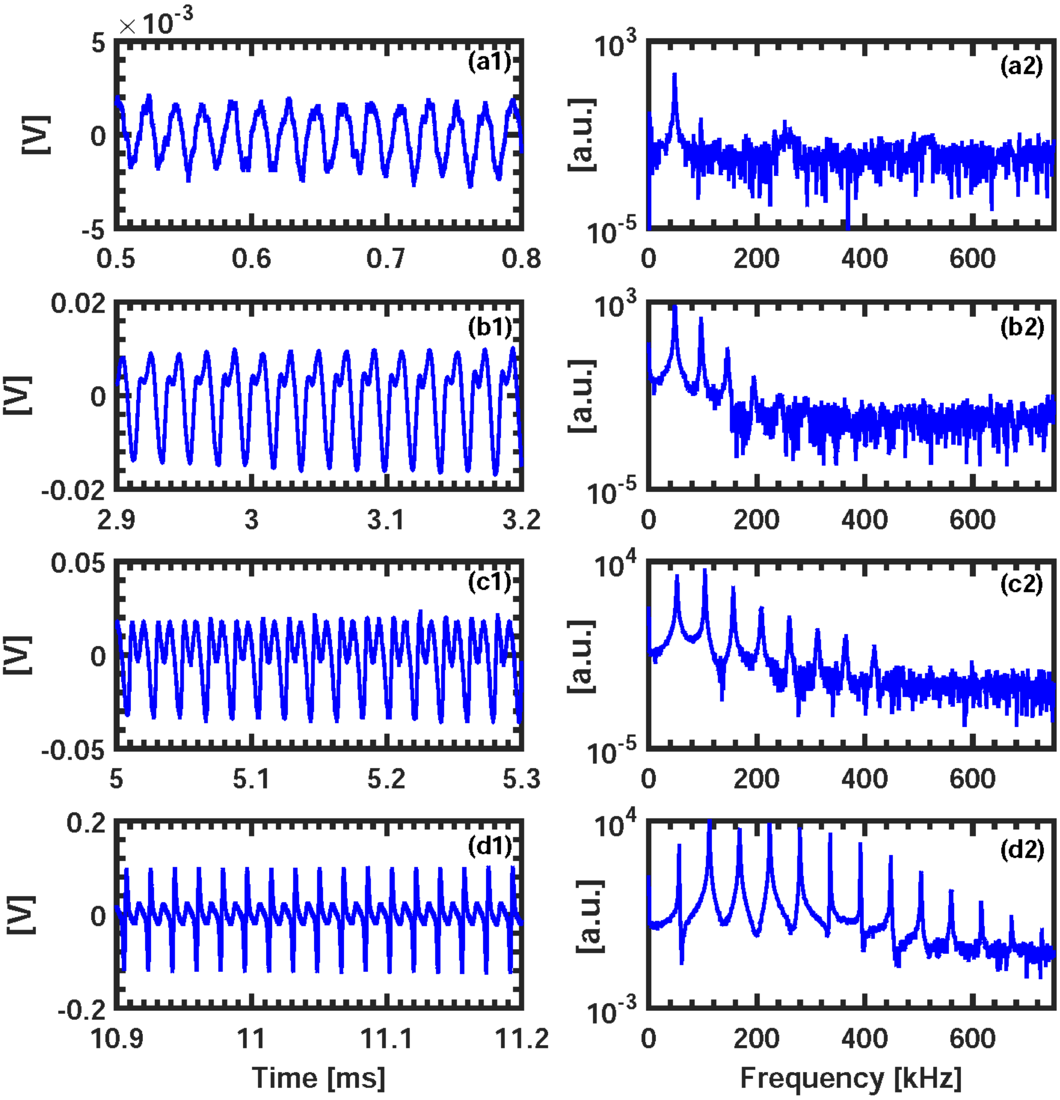

Figure 4.2: Time trace of capacitive probe signal at different instances of evolution. (a1-d1) 4 distinctive stages of evolution showing transition from small amplitude oscillation to large amplitude, double-peak oscillation during the trapped phase of the electron plasma. (a2-d2) Corresponding power spectra of each stage showing gradual appearance of multiple harmonics as the mode evolves with pre-dominant energy in $m = 2$.

nature of the oscillations. A single diocotron oscillation and the schematic of the plasma used to explain it has been reproduced from Ref. [63] in Fig. 4.3(a) and (b). The schematic assumes an elliptical trajectory of charge cloud, in the poloidal

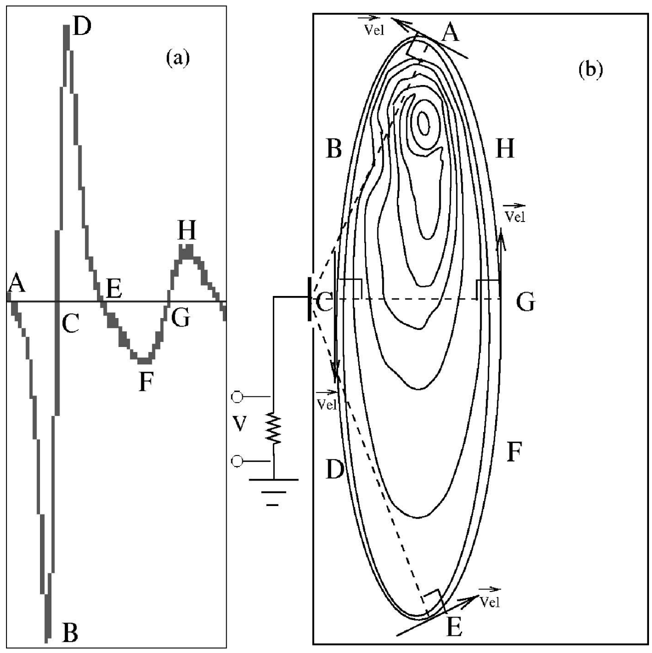

Figure 4.3: A schematic showing a possible orbit corresponding to a single period of oscillation resulting from one azimuthal drift. (a) A single period of oscillation from wall probe signal. (b) The plasma profile depicted in the poloidal cross section; also shown are velocity vectors at orbit positions that correspond to zero currents on the probe. “Reprinted with permission from Phys. Plasmas 13, 092111 (2006) Copyright 2006, AIP Publishing LLC"

plane, closely hugging the inboard wall. There are four locations in the D-shaped orbit where the distances from the probe to the point go through the extrema, giving rise to two maxima (and two minima) and hence appearance of a pair of alternating cycles in an oscillating period. There are locations when the velocity will be perpendicular to the electric field vector (line joining the probe to the point) and therefore $\vec{E} \cdot \vec{v}$ will be zero resulting in zero probe current. However, due to lack of charge density profile and its time evolution and/or a mathematical construct that substantiates this model, the above description had so far remained only a conjecture.

4.3 Image currents on Capacitive probes: Derivation and Numerical computation

In order to interpret the capacitive probe signal and obtain the charge cloud trajectory undergoing diocotron oscillations, the inverse problem is addressed. An expression for induced charge on the capacitive probes is derived for a test charge ‘q’ undergoing $E \times B$ excursions in a poloidal plane. Induced current on the wall probe is then computed numerically for any given input trajectory. A rectangular poloidal geometry consistent with that of SMARTEX-C has been assumed for all cases. The effect of toroidicity on the induced current is included later (by accounting for the unequal inner and outer-wall areas of a toroid.)

4.3.1 Derivation for Image Current using Green’s Reciprocation Theorem

Green’s reciprocation theorem can be illustrated as follows. Let a charge distribution ρ produce voltage distribution V (say, Scenario A) and charge distribution ρ' produce voltage distribution V' (Scenario B). These are different and independent scenarios. Applying the principle of Green’s reciprocity [70, 156], variables charge (ρ) and voltage(V) are interchangeable in the two scenarios, and can be expressed as

$$\int \rho V' d\tau = \int \rho' V d\tau \tag{4.1}$$

Scenario A has been envisaged in Fig. 4.4 (A) that shows a point charge ‘(-)q’ placed at a point X, in the poloidal cross section (rectangular) of the trap. Capacitive probe, (labelled as ‘Probe’) is grounded ($V_p = 0$) and develops an image charge ‘$(+)Q_p$’. Rest of the trap wall too is separately grounded ($V_{wall} = 0$) and develops an image charge ‘$(+)Q_{wall}$’. The potential at point X (excluding the self-field due to ‘q’) for given boundary conditions is V. Expression for induced image current on ‘Probe’ can be obtained by solving for the time evolution of image charge $(+)Q_p$.

To solve for ‘$(+)Q_p$’ we utilize Green’s Reciprocation Theorem, as realized in Ref. [70, 76]. A hypothetical scenario B is imagined and illustrated in Fig. 4.4

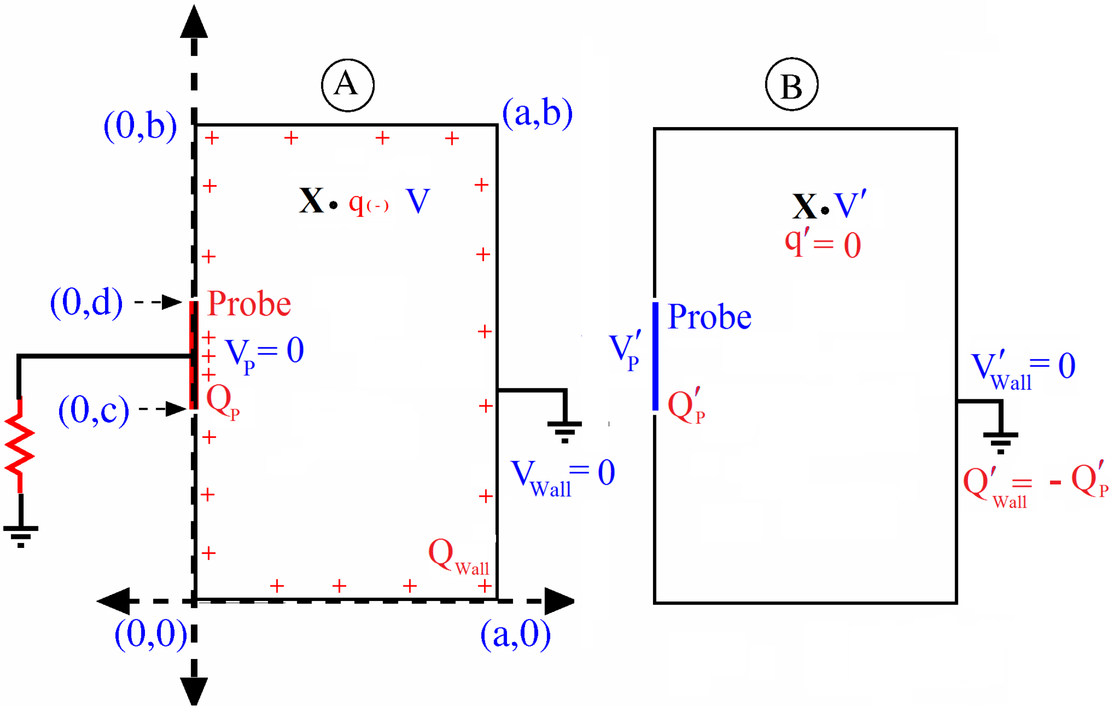

Figure 4.4: Green's reciprocity theorem: (A) Induced image charge $(+)Q_p$ to be found on capacitive probe 'P' corresponding to point charge '(-)q' at point X located in poloidal cross-section of trap. (B) (Re-modelled problem) Potential distribution at point 'X' is solved for a hypothetical bias voltage V'_p on 'Probe'. Chosen co-ordinate system is shown for reference.

(B). Charge q' in scenario B has been kept deliberately zero. Capacitive 'Probe' is biased at hypothetical potential V'_p having charge Q'_p. Rest of the grounded wall ($V'_{wall} = 0$) has image charges($Q'_{wall} = -Q'_P$) satisfying Gauss Law within the closed boundary (consistent with $q' = 0$. Now, the potential at point X is V'.

Applying Eq.(4.1) to scenarios in A and B leads to,

$$\underbrace{(-)qV'}_{Plasma} + \underbrace{Q_pV'_p}_{Probe} + \underbrace{Q_{wall}V'_{wall}}_{Wall} = \underbrace{(-)q'V}_{Plasma} + \underbrace{Q'_pV_p}_{Probe} + \underbrace{Q'_{wall}V_{wall}}_{Wall} \tag{4.2}$$

As $(-)q'$, V_p and V_{wall} are zero, RHS is zero. Also as the walls are grounded in scenario 'B', V'_{wall} (in LHS) is zero. Therefore, Eq.(4.2) reduces to:

$$qV' = Q_pV'_p \tag{4.3}$$

Induced image current on the probe can then be obtained by,

$$\begin{aligned}\frac{dQ_p}{dt} &= \frac{q}{V_p'}\frac{dV'}{dt} + \frac{V'}{V_p'}\frac{dq}{dt} + qV'\frac{d}{dt}\left(\frac{1}{V_p\prime}\right)\\ \frac{dQ_p}{dt} &= \frac{q}{V_p{}'}\frac{dV'}{d\vec{r}}\cdot\frac{d\vec{r}}{dt} + \frac{V'}{V_p{}'}\frac{dq}{dt} + qV'\frac{d}{dt}\left(\frac{1}{V_p\prime}\right)\end{aligned} \tag{4.4}$$

If charge q remains constant during the time interval of interest, second term may be neglected. Also, since $V_p{}'$ is a constant voltage applied on the probe, its time derivative (third term) is zero. Thus, the expression for image current i(t) simplifies to,

$$i(t) = -\frac{q}{V_p{}'}\vec{E}\cdot\vec{v} \tag{4.5}$$

Where, E is the electric field (due to applied potential $V_p{}'$) and v is the velocity of the point charge. To obtain E, we solve Laplace's equation for potential V', (using separation-of-variable method) for given boundary conditions and obtain its spatial derivatives. For 2-D Cartesian geometry, general solution to Laplace's equation can be written as,

$$\Phi(x, y) = \{A_\alpha \exp(\alpha x) + B_\alpha \exp(-\alpha x)\} \cdot \{C_\alpha \sin(\alpha y) + D_\alpha \cos(-\alpha y)\} \tag{4.6}$$

Applying appropriate boundary conditions, constants $A \dots D$ and α are obtained as follows.

1. For $y = 0$, and $0 \le x \le a$ (Bottom wall): $\Phi = 0 \Rightarrow D_\alpha = 0$.

2. For $y = b$, and $0 \le x \le a$ (Top wall) : $\Phi = 0 \Rightarrow \alpha = \frac{n\pi}{b}$, for $n = 1, 2, 3 \dots$

3. For $x = a$, $0 \le y \le b$ (Outboard side) : $\Phi = 0, \Rightarrow A_\alpha + B_\alpha = 0$ (for all α)

4. For $x = 0$, $0 \le y \le c$ and $d \le y \le b$, (Inboard side sans probe) : $\Phi = 0$,
   For $x = 0$, $c < y < d$ (Probe): $\Phi = V_p{}'$.

Substituting the above, in Eq. 4.6, we get

$$\Phi(x,y) = \sum_{n=1}^{\infty} \frac{2V_p{'}\{\cos(\alpha_n c) - \cos(\alpha_n d)\}}{\alpha_n\{1-\exp(2\alpha_n a)\}} \cdot \sin(\alpha_n y) \cdot [\exp(\alpha_n x) - \exp \alpha_n(2a - x)] \tag{4.7}$$

which can be simplified using hyperbolic functions as

$$\Phi(x,y) = -\sum_{n=1}^{\infty} \frac{2V_p{'}\{\cos(\alpha_n c) - \cos(\alpha_n d)\}}{\{n\pi \sinh(a\alpha_n)\}} \cdot \sin(\alpha_n y) \cdot \sinh\{\alpha_n(x-a)\} \tag{4.8}$$

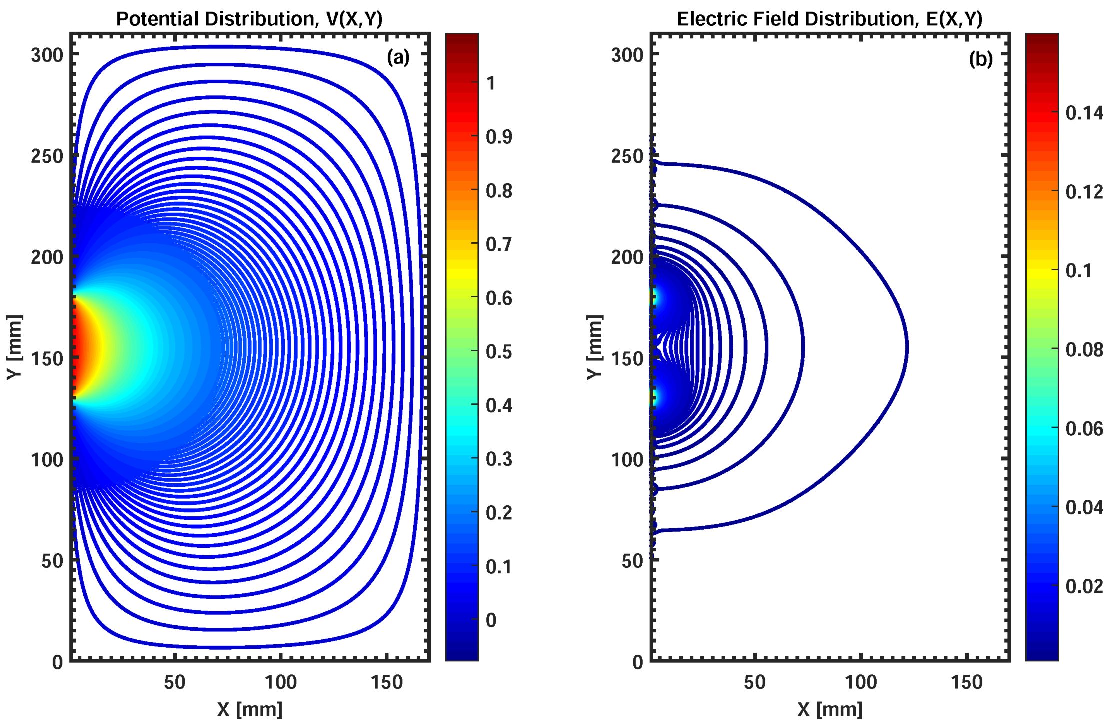

Figure 4.5: Solution of the hypothetical problem shown in schematic (B) of Fig. 4.4. (a) Potential and (b) Electric field distribution (numerically evaluated) in poloidal cross-section of SMARTEX-C due to applied potential $V_p{'}$ on capacitive probe.

To compute potential (Φ), a series sum of $n = 50$ terms is adequate as potential converges to an accuracy of 1×10^{-8} for electrically grounded boundary. Solution is obtained on entire 2-D geometry taking grid size as 0.1 mm. Potential contours for the trap geometry and probe dimensions of SMARTEX-C are plotted in Fig. 4.5 (a). The corresponding electric field ($E(x, y)$), computed by taking the spatial derivatives of Eq. 4.8, is plotted in Fig. 4.5 (b). The field at each grid point (x, y) is used to estimate the image current on the probe (from Eq. 4.5),

$$i(t) = \frac{-q}{V_p{}'}\{E_x \cdot v_x + E_y \cdot v_y\} \tag{4.9}$$

It may be noted that substituting the expression for E (obtained from $\Phi(x, y)$ in Eq. 4.7), makes the image current independent of the hypothetical probe bias $V_p{}'$ (introduced and applied on probe for reciprocity). Charge q and velocity v of the point-charge are however essential to compute the current and are obtained experimentally.

4.3.2 Capacitive probe signal for various poloidal trajectories

Numerical experiments are now conducted where the plasma is assumed to be a point-charge containing all of the charge and undergoing $\vec{E} \times \vec{B}$ rotation in the poloidal cross-section. Various trajectories are assumed and the respective probe current due to induced image charges are numerically computed for a wall probe at a specified location. (The poloidal cross-section is consistent with the geometry of SMARTEX-C; determination of charge and velocity of the point-charge from experiments are described later in section 4.4). Trajectories of a single vortex are computed using following equation:

$$\begin{aligned} x(t) &= x_0 + r_h \cos(2\pi f t) \\ y(t) &= y_0 + r_v \sin(2\pi f t) \end{aligned} \tag{4.10}$$

Here, x and y are co-ordinates of the trajectory at time instant t, x_0 and y_0 refers to the equilibrium position of the vortex (trap-center, initially), r_h and r_v corresponds to the horizontal and vertical dimension of the trajectory, (for circular trajectory $r_h = r_v = r$ =radius of the trajectory) and f the oscillation frequency. Wall probe signal corresponding to these parameters is computed from Eq. 4.9. To evolve the trajectory, one or more parameters of interest is changed in time. The rate of change is presently arbitrary.

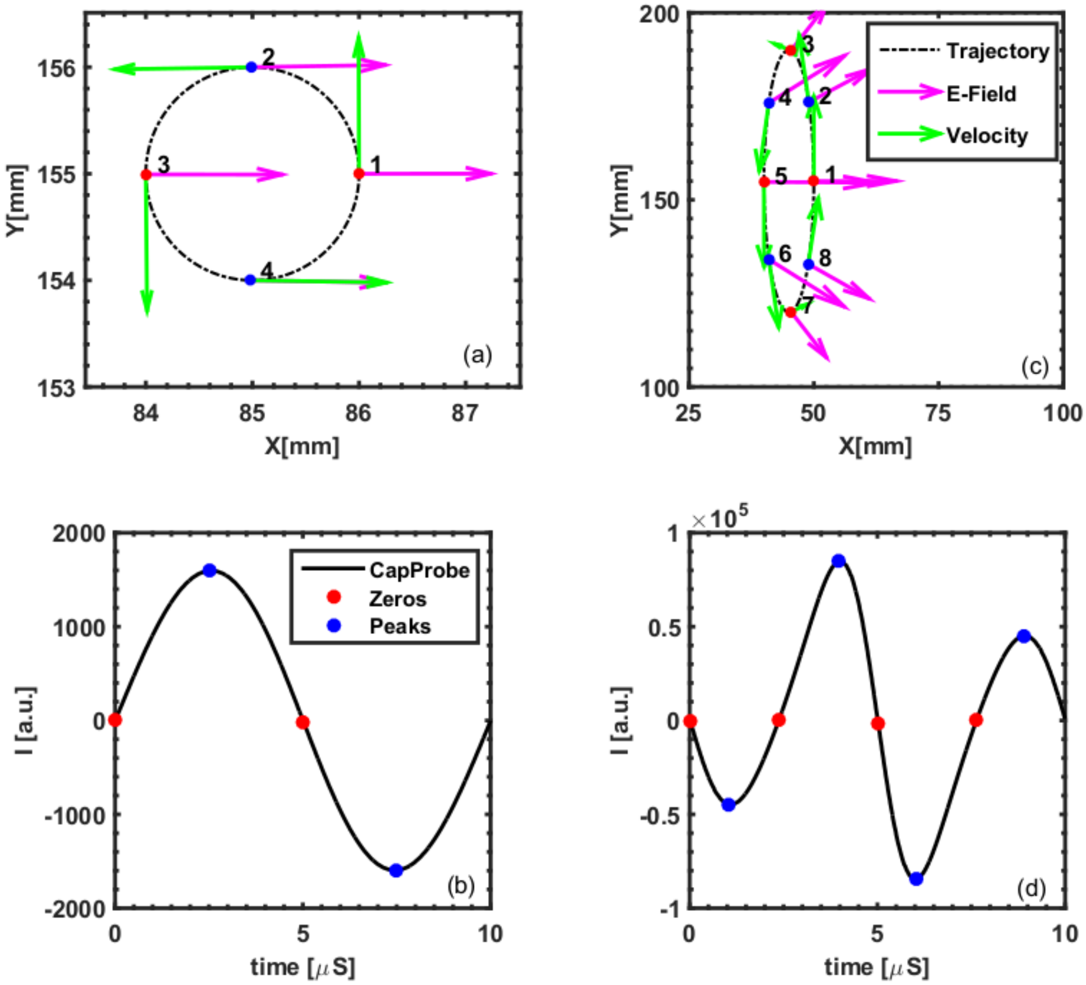

Figure 4.6: Numerically generated trajectories of charge vortex and wall probe signals. (a-b) Circular trajectory and corresponding signal on wall probe. (c-d) Elliptical trajectory and corresponding signal on wall probe. (Peaks and zeros of the signals are represented with blue and red dots respectively. Electric field and velocity vectors at corresponding locations are also shown.)

1. Circular trajectory: Time evolution of a wall-probe signal for the simplest case of a point charge undergoing small amplitude circular trajectory (Fig. 4.6 (a)), is shown in Fig. 4.6 (b). The resulting sinusoidal current has a single alternating cycle; it is zero (twice), when $\vec{E}$ and $\vec{v}$ are perpendicular to each

other and peaks when the vectors are parallel (or anti-parallel) to each other (Fig. 4.6 (a)).

Ratio of the peak amplitudes as well as the relative phase between the inboard-to-outboard and top-to-bottom wall probe signals give an estimate of the equilibrium position. It may be noted, that in a toroidal trap, a charge vortex placed mid-plane on the minor axis (equidistant from the outboard and inboard sides) will not induce equal charges on the probes placed inboard and outboard because of unequal surface areas of inner and outer walls, although signals will be out of phase by π. Ratio of the signal amplitudes on the two probes for any radially shifted equilibrium will have to be corrected for this toroidal effect. For, SMARTEX-C this correction factor is 2.5, obtained from the ratio of probe areas normalized to the respective wall-area on which it is mounted (corrections for area covered by vessel ports are included). Any vertical shift will however cause a phase difference less than π, in addition to unequal signal amplitudes on top and bottom wall probes.

2. Elliptical trajectory: If the charge moves in an elliptical trajectory instead of a regular circular path, (with the major axis perpendicular to the probe-normal), numerically computed signal shows (Fig. 4.6 (c) and (d)) *two* alternate cycles in a single period. The transit of the negative point charge on the inboard side is represented by the large oscillating signal: as it moves towards the probe positive charges flow into the probe from ground and a negative signal is induced. As it moves away, a positive current is produced. This repeats itself in the return path resulting in a second, weaker oscillating signal. The amplitude of the latter is smaller, as the transit occurs away from the probe reducing the electric field subtended normal to the probe. The appearance of these "double-peak" oscillations depends on the eccentricity of the trajectory. In our experiments, the two oscillating cycles in a period is typically discernible on the probe if the ratio of the amplitude of the two peaks in the signal is less than 200 (considering data is acquired with a 12-bit digitizer, having noise floor 20 times least-count of digitizer (0.5 mV), and the probe circuit is designed to give a peak amplitude of 100 mV). Numerical experiments have been carried out with above consideration to suggest a minimum (threshold) eccentricity of the trajectory for a detectable "double-

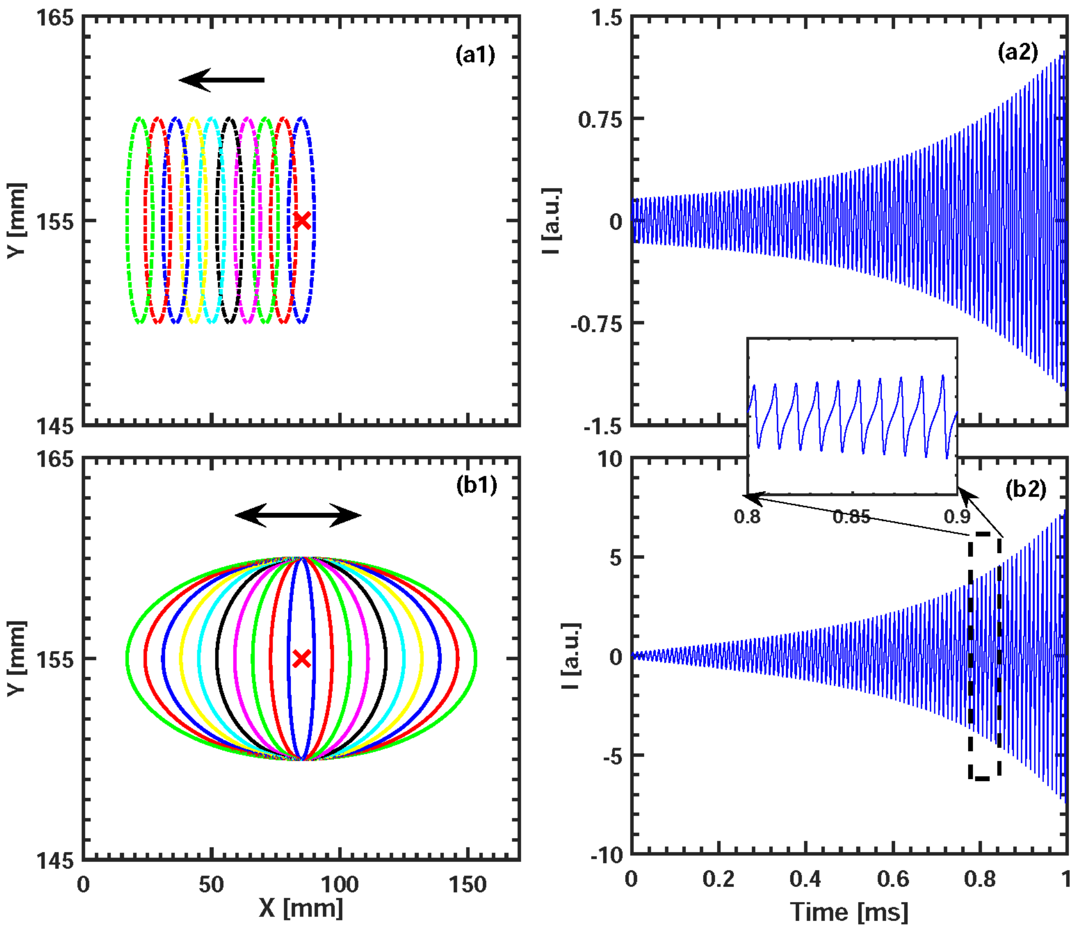

Figure 4.7: (a1) Circular trajectory drifting radially inwards.(b1) Circular trajectory undergoing radial elongation (parallel to probe-normal). (a2 - b2) Corresponding time evolving capacitive probe signals obtained numerically. (b2-inset) Signal oscillations (zoomed).

peak". Though weakly dependent on certain parameters viz., probe size, distance of trajectory from probe and cross-sectional (poloidal) aspect ratio, the threshold eccentricity of the orbits is always well above 0.98.

3. Time evolution of circular trajectories: If a circular trajectory (a) radially drifts inwards (0.5 mm per oscillation in Fig. 4.7(a1),) or (b) undergoes uniform radial expansion or (c) elongates along a direction parallel to the probe-normal (1.0 mm per oscillation in Fig. 4.7(b1)), oscillations will register a growth in amplitude but a poloidal sweep will still be marked by a

single alternating cycle on the wall probe. The growth rates will however be different as seen in Figs. 4.7 (a2) and (b2). It is further observed that if trajectories draw closer to the wall probe the oscillations get gradually distorted from sinusoidal to triangular pulses with rather sharp peaks.

On the other hand, if an initial circular trajectory turns elliptical by elongating perpendicular to probe-normal (Fig. 4.8(a1)), wall probe signal registers a growth in amplitude and a single alternating cycle (corresponding to a single poloidal rotation) gradually splits into two alternate cycles, as described earlier. Evolution of wall probe signals, for a growth rate of 1.6 mm per oscillation, is shown in Fig. 4.8(a2).

In order to distinguish among the various evolution of circular trajectories mentioned above, one may compare simultaneous pick-up on wall probes that are located at other poloidal locations, namely top/bottom and outboard walls. For example, any expansion along major radius, although symmetric for side wall probes, will appear as an elongating ellipse for the top and bottom probes and therefore, can be identified, by the easily distinguishable feature of "double-cycles" on these probes signals. Whereas, a symmetric radial expansion of the orbit, will show up as uniform and simultaneous growth in amplitude on all the probes. On the other hand, for a charge orbit drifting radially, say inwards, oscillation amplitude on outboard side probe will be gradually damped. In fact, the ratio of signal-amplitudes on outboard and inboard wall probes can be used to identify the amount of radial shift in time, during their evolution.

4. Time evolution of elliptical trajectories: Any elliptical trajectory, as described earlier, will be marked by double-oscillations on those wall probes whose probe-normal is perpendicular to the major axis of ellipse. Appearance of second oscillation is related to the eccentricity; threshold eccentricity depends on the probe dimensions relative to the trajectory size (major radius) and probe distance from the trajectory. As eccentricity of the trajectory increases, the ratio of two peaks is seen to decrease (see Fig. 4.8(a1) and (a2)). However, if the increasing ellipticity is also accompanied by an inward (radial) shift, ratio of the two peaks grows rapidly. Such an evolution is shown in Fig. 4.8(b1) and (b2), where the orbit is elongated vertically (at 1.6 mm

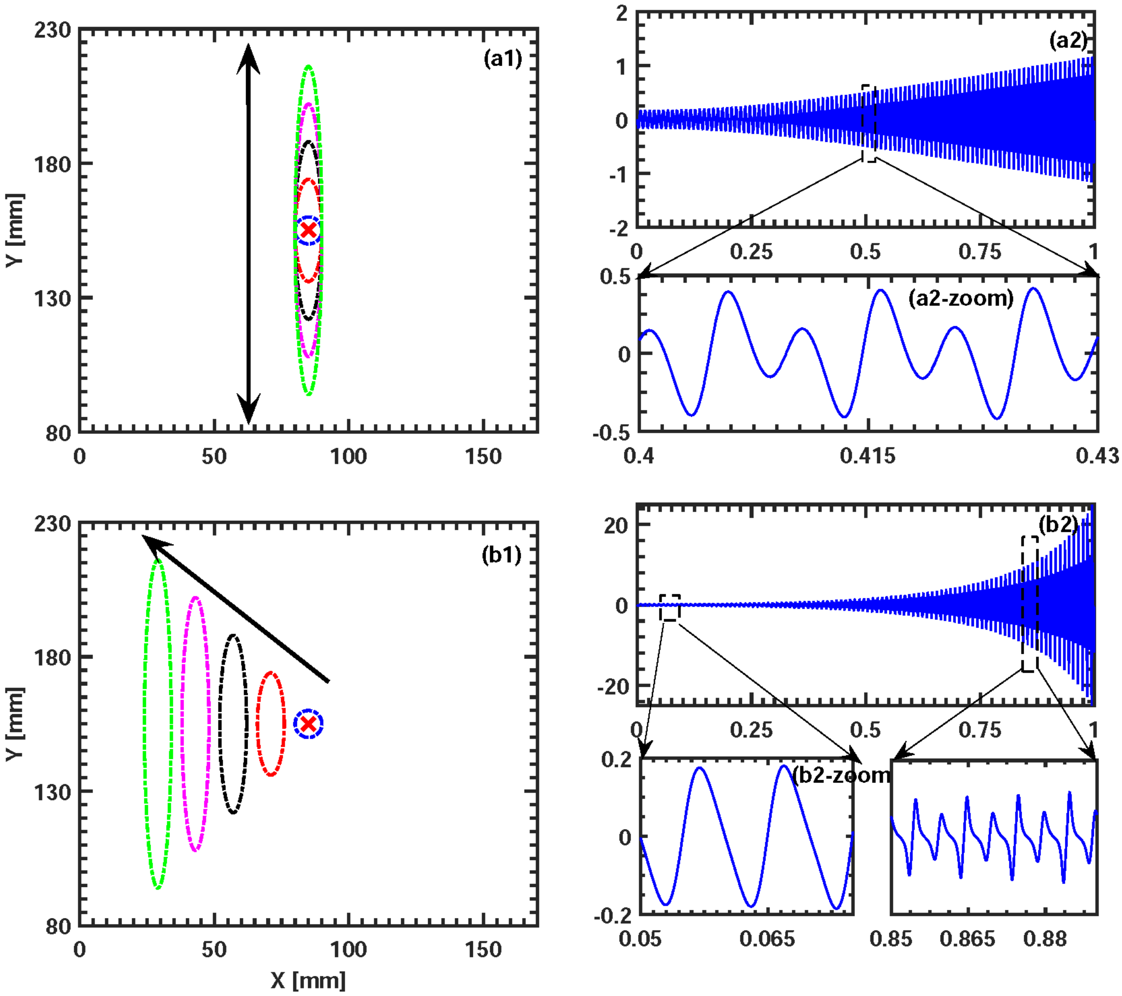

Figure 4.8: Circular trajectory undergoing (a1) vertical elongation. (b1) Vertical elongation accompanied by radial shift. (a2 - b2) Corresponding time evolving capacitive probe signals obtained numerically.

per oscillation) and shifted radially inward (at 0.4 mm per oscillation).

5. Trajectory evolution accompanied by a decay of charge: In addition to change in charge trajectory, any loss of charge can also affect the signal evolution. Eq. 4.4 in such cases is evolved, retaining the term reflecting the time-rate of change of charge.

   Oscillations in such cases are seen to damp. An interesting evolution is shown in Fig. 4.9 where a radially drifting (at 0.15 mm per oscillation) point-

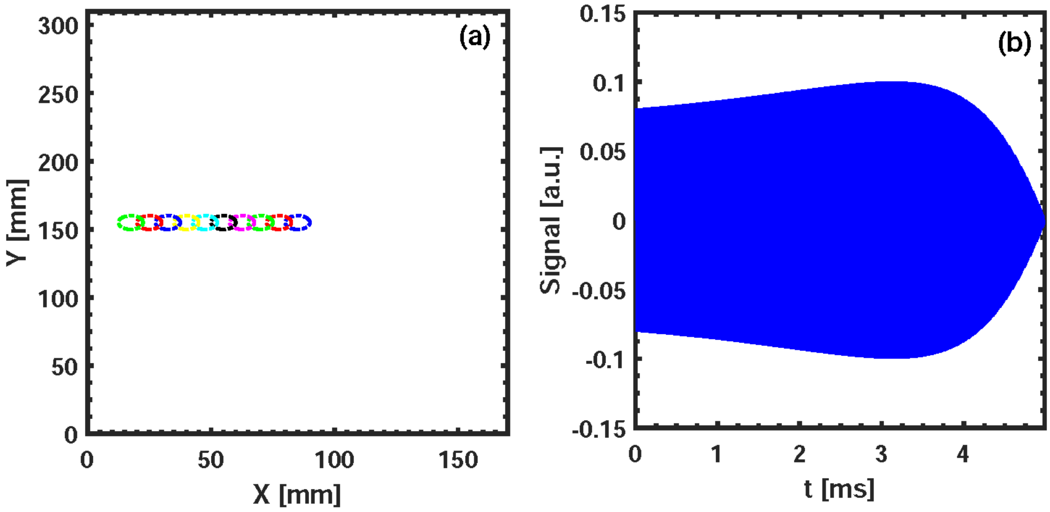

Figure 4.9: (a) Radially shifting circular trajectory accompanied by charge loss. (b) Evolution of corresponding capacitive probe signal.

charge is simultaneously losing charge (at the rate 0.2% of total charge per oscillation). The probe signal is seen to grow in amplitude, saturate and subsequently damp. The rate of growth and damping is obviously dependent on the rate of charge loss compared to radial drift.

4.4 Investigation of Charge Vortex Dynamics in SMARTEX-C

Signals generated from representative trajectories in our numerical experiments are used as reference and correlated with time evolving, oscillatory wall probe signals observed in SMARTEX-C. This helps to explain several distinctive features of the signals and suggests possible interesting dynamics of a charge vortex in the poloidal plane of SMARTEX-C as the diocotron mode gets destabilized.

As seen from Fig. 4.1 (a) diocotron oscillations appear soon after injection, grow to large amplitudes and non-linearly saturate before damping. Recent experiments [122] have allowed observation of transition of the mode oscillations from small amplitude, linear, near-sinusoidal to large amplitude and non-linear, "double-peaked" oscillations with many harmonics.

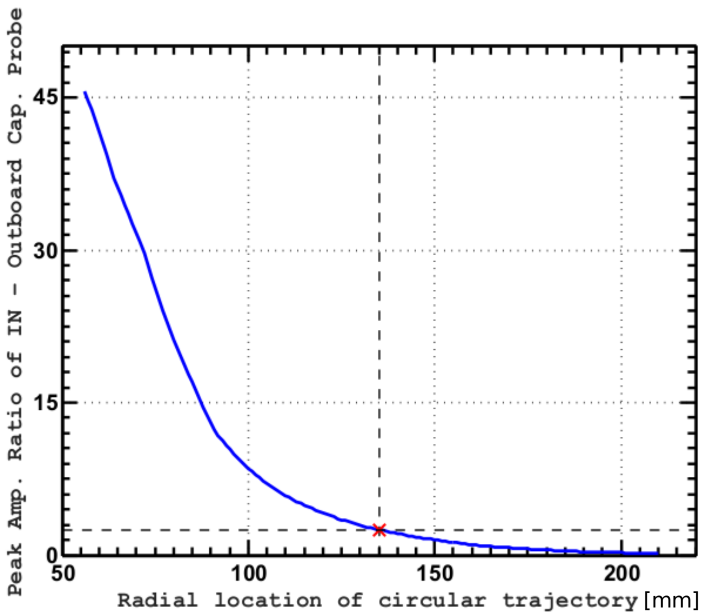

Figure 4.10: Ratio of peak-amplitudes of oscillating signals on inboard and outboard capacitive probes vs location of charge-vortex (with respect to the probes). In a 2-D Cartesian geometry, the ratio is 1 when charge is located equidistant from the probes. In a toroid (SMARTEX-C), ratio is 2.5 (marked with cross) when charge is placed on minor axis, (equidistant from the inner and outer wall) due to unequal surface areas on inboard and outboard.

To explore possible dynamics consistent with these observations, trajectories of a single vortex is computed from Eq. 4.10 and corresponding wall probe signals are obtained from Eq. 4.9. Here, all of the plasma is assumed to be concentrated in the single point vortex, whose orbit is given by the co-ordinates, x and y. The assumption of point charge vortex would be valid provided the charge cloud has dominant monopole component in the vortex and other higher order poles do not contribute significantly. The parameters essential to numerically compute the wall probe signals, namely, initial position x_0, y_0, total charge q in the point-vortex, and poloidal velocity v, are obtained from experimental data as follows.

The initial small-amplitude signal seen on the probe is assumed to represent the vortex oscillations around equilibrium position (x_0, y_0) of the plasma. Assuming a small, circular trajectory of radius r of the point charge vortex, capacitive probe signals are numerically generated (using Eq. 4.9, for experimentally known charge q, and poloidal velocity, v) for trajectories centered at various radial locations in the trap. The amplitude ratios on outboard and inboard probe-signals thus obtained are plotted for vortex located at different radial locations in Fig. 4.10. Comparison with experimentally observed ratios of peak-amplitudes of initial (small-amplitude) oscillations (from probes poloidally separated by 180^o) indicates the actual equilibrium position of the cloud in the trap for a given magnetic field. It may be noted that a ratio of 2.5 represents a location equidistant from the inboard and outboard walls in SMARTEX-C (discussed in Sec. III B).

The initial equilibrium position is dependent on magnetic field (B) as shown in Fig. 4.11(b). Shift in equilibrium with B has also been corroborated independently by assuming a diocotron like mode and applying $\frac{1}{B}$ scaling to the small-amplitude oscillation frequency obtained from the probe data. As shown in Fig. 4.11 (a) the fit rather applies well to $\frac{1}{(B+K)}$, where B is field at minor axis and K is a constant that represents a shift corresponding to 35 Gauss. The equilibrium location as suggested by $B + K$ compare well with those obtained from ratio of inboard and outboard probe signals. The inward shift (away from minor axis) ranges between 0.5 cm (350 Gauss) to 3 cm(130 Gauss).

To obtain the charge content, q, the "inject-hold-dump" sequence is repeated by varying the 'hold-time'. The charge collected on the collector grid, gives an estimate of total trapped charge [139] (Q-total) at the instant of dump. For our numerical experiments, the entire charge has been assumed to be concentrated in a point vortex and used to compute induced current. Also since charge-loss rate is slow compared to diocotron oscillation period, it is assumed constant during one poloidal trajectory. Alternately, vortex-charge (Q-vortex) can also be estimated from the measured diocotron frequency (as in cylindrical geometries, under assumption of infinite length), from,

$$f_{Dio} = \frac{Qe}{4\pi^2 \epsilon_0 B_\phi {R_w}^2 L} \tag{4.11}$$

where, L is the trapping length, R_w is wall radius, and B_ϕ is toroidal magnetic field. Comparison of Q-vortex and Q-total suggest that initially (soon after injection) the total charge could be more than that in the vortex by a factor of 2. The charge gradually concentrates into the vortex as the mode evolves. However, as

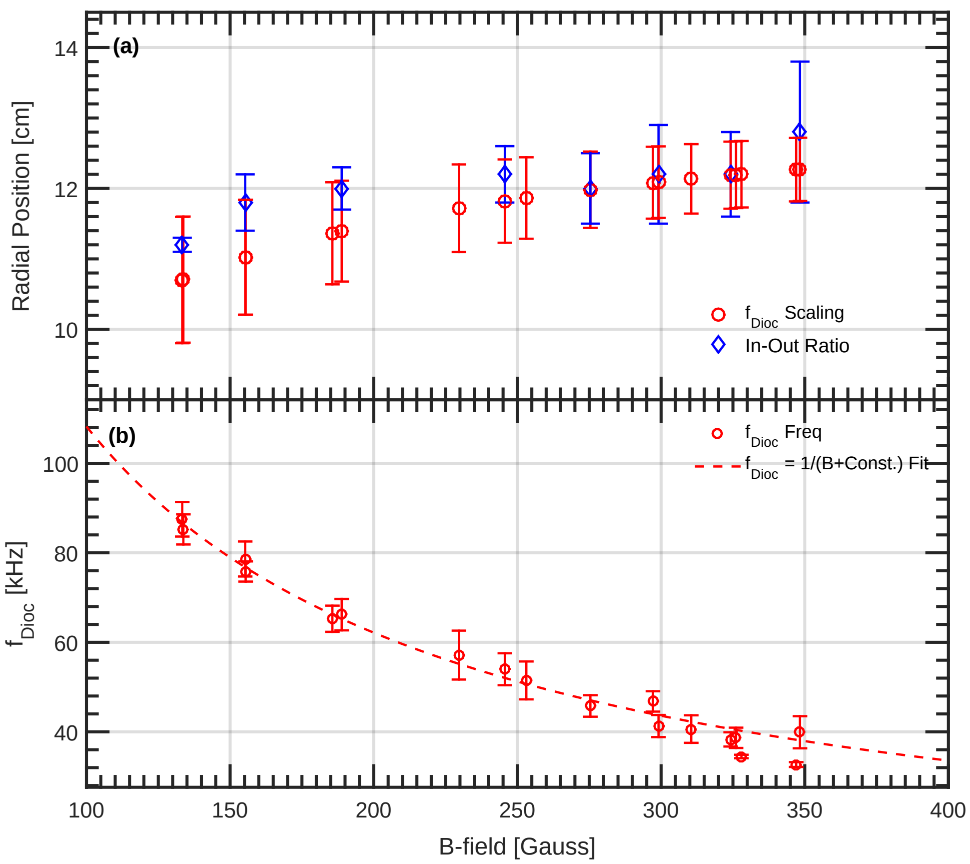

Figure 4.11: (a) Small amplitude oscillation frequency vs B field: Plotted frequencies $\alpha 1/(B+K)$ where B is estimated at the minor axis and K corresponds to ~ 35 Gauss. (b) Equilibrium position suggested by 1/(B+K) scaling (circle) compared with those obtained from ratio of wall probe signals (diamond), for different B fields.

the mode turns non-linear, such an estimation is presently fraught with errors as the measured frequency may be higher due to toroidal effects [48,56] (inward shift in equilibrium) in addition to finite length and kinetic effects [81]. Over-estimation of charge from Eq. 4.11, is therefore a likelihood.

Velocity of the charge cloud has a complex time evolution as may be seen from a single "double-peak" oscillation of Fig. 4.3 (inset), representative of a single poloidal rotation. It consists of two different time periods; signifying a fast motion ($5-7\,\mu$s) on the inboard side and a slower motion ($10-12\,\mu$s) on outboard side of the poloidal plane. Interestingly, velocity (E/B) is higher on the inboard side in spite of corresponding B field being ($\approx 200\%$) higher, suggesting a significant concentration of charges in the vortex and increase in electric field during inboard excursion. Instantaneous velocities, at least for a few locations, may be obtained by finding the time interval, say, between zero crossings or peak amplitudes, of two poloidal probes signals. However, for the present purpose, velocity of the charge cloud has been averaged over a few diocotron oscillations and estimated by finding time lag (τ) between signals from two poloidal probes using cross-correlation technique. Cross-correlation between 8192 points of two neighboring poloidal probes has been carried out, providing resolution in the range of 100 ns – 0.8192 ms in time-lag. Velocity, v, so obtained is also used to estimate the approximate dimension of the trajectory r from $v = 2\pi r f$, where, frequency f is obtained from FFT of the observed oscillations.

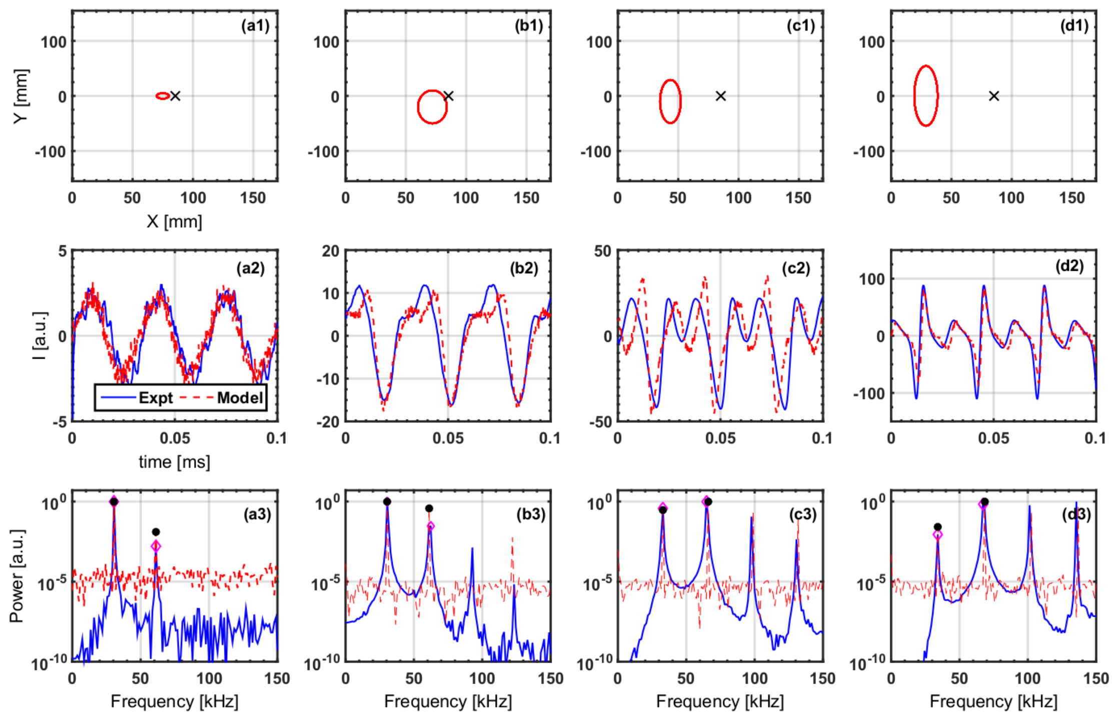

Figure 4.12: (a1-d1) Trajectory of charge vortex modelled to represent 4 distinct stages of evolution identified from probe signals. (a2-d2) Corresponding probe signals generated numerically and comparison with experimental signals (B - 210 Gauss). (a3-d3) Fourier transform of numerical and experimental signals.[Solid — Experimental and dashed - - - Model results.]

Having thus obtained, equilibrium position (x_0, y_0), charge q, poloidal velocity v, radius r and diocotron frequency f, the circular trajectory corresponding to the initial phase of small amplitude oscillations is plotted in Fig. 4.12 (a1). A vertical shift (also confirmed from amplitude ratio of top-to-bottom capacitive probe) and vertical elongation of the circular trajectory, in time, are responsible for the signal to become asymmetric (in amplitude). Trajectory gradually becomes elliptical; major radius of the ellipse has been tweaked appropriately in our numerical experiment to match the experimental signal. Signal shape and its Fourier transforms are compared and amplitude of the signal is rescaled to match with the experimental data which compensates for any error in the estimation of velocity and charge.

For a given B field, four distinct stages of time-evolution are seen in our experiments (Fig. 4.12 (a2 - d2) (solid line)). Modelled trajectory(Fig. 4.12 (a1 - d1)) and corresponding signal generated numerically has been compared with the experimental signal in Fig. 4.12(a2 - d2) (dashed line) respectively. Comparison of Fourier transforms of experimental (solid line) and numerically computed signals (dashed line) is also shown in Fig. 4.12 (a3 - d3).

Numerically computed signals and their harmonic content are consistent with experimental probe signal and its spectrum, suggesting a single vortex-like dynamics. As the initial small-amplitude circular trajectory evolves in time it shifts radially inward and gradually becomes elliptical. The probe signals distort from a near sinusoidal with a gradual appearance of double-peak. Growth in amplitude is accompanied with appearance of higher harmonics. Presence of a dominant second harmonic suggests that the vortex trajectory evolves from a center-of-charge motion ($m = 1$) to a non-linear state where the predominant energy is present in the elliptical shaping of the cloud ($m = 2$). *These experimental results, endorsed by numerical analysis and corresponding interpretation, establish a single vortex dynamics during diocotron instability in toroidal non-neutral plasma. It also suggests, complex dependency of the mode amplitude on vortex trajectory, shape and radial position of the plasma.*

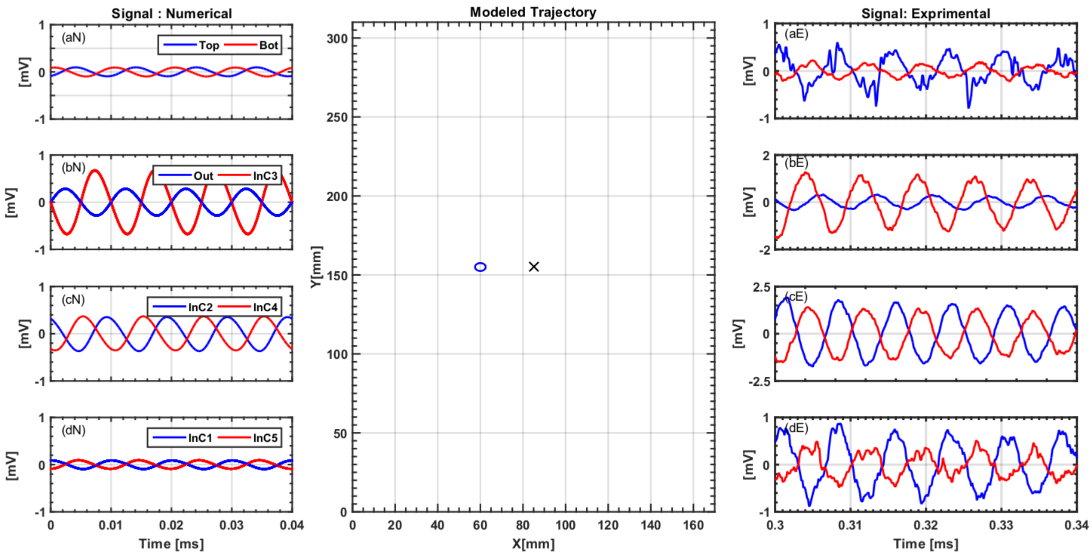

Figure 4.13: (aE - dE) Experimental signals observed on different capacitive probes, (Center) Modelled trajectory and trap center marked with label 'X' (aN - dN), Modelled signals calculated from derived image charge signals by solving Green's reciprocation theorem.

4.5 Uniqueness of Trajectory

It has been demonstrated in previous section (Figure 4.12) that capacitive probe signals can be simulated assuming charge vortex trajectories in a poloidal cross-section. By correlating with experimentally observed probe signals possible trajectories may be obtained. However such trajectories are, as understood, intuitive guesses and not evolved self-consistently. Also, the correlation of numerically obtained signal with experimental data has been carried out for a single probe only. The trajectory is therefore only one among the many possibilities whose uniqueness is yet to be established. Phase information obtained simultaneously from various other poloidal probes is therefore crucial in establishing the uniqueness and validating the suggested dynamics. In order to do so expression for image current signals have been derived for all capacitive probes installed in a poloidal plane (See Appendix A). As an exercise, numerical signals have been computed and correlated with experimental data from all the probes for Phase I of trajectory depicted in Figure 4.12(a1)-(a3). Figure 4.13(aE) to (dE) shows experimental signal from all eight capacitive probes; corresponding numerically generated signals are shown in Figure 4.13(aN) to (dN). Trajectory has been modelled for a single charge vortex as shown in Figure 4.13 center . Evidently while the numerically generated signal for the modelled trajectory is consistent with the experimental data from a mid-plane capacitive probe placed on inboard side, several discrepancies can be observed when signal from other probes are compared, notably,

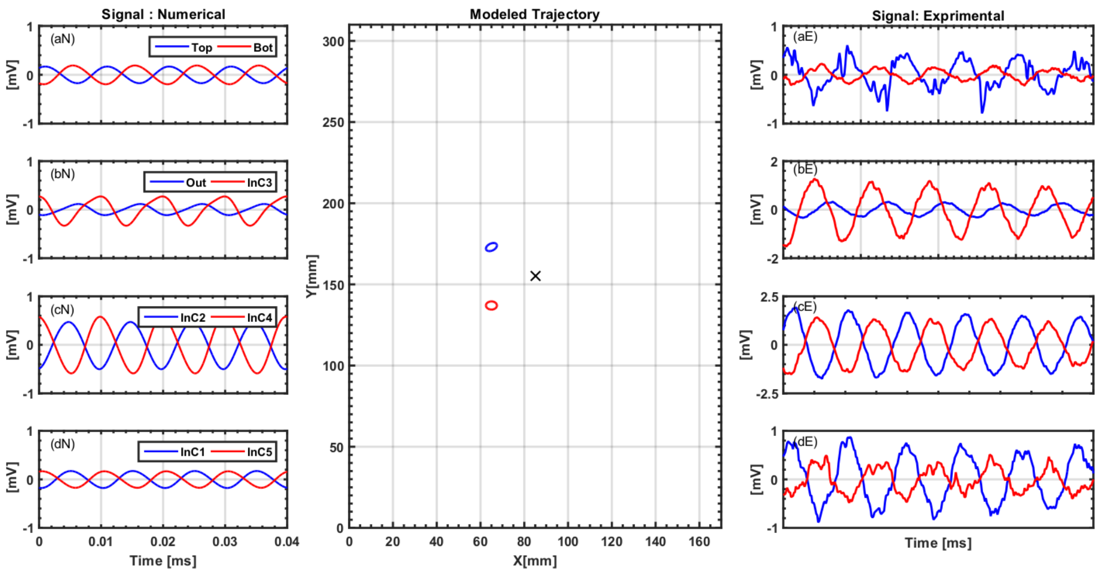

Figure 4.14: (aE - dE) Experimental signals observed on different capacitive probes at 0.3 ms instance of SMARTEX-C plasma shot 123, (Center) Modelled trajectory of two vortices undergoing diocotron oscillations and trap center marked with label 'X' (aN - dN), Modelled signals calculated from derived image charge signals by solving Green's reciprocation theorem for all capacitive probes.

- Phase relations between the probe signals is not consistent between experiments and simulations; For e.g. phase difference between Inboard and Outboard capacitive probe is expected to be π from our model, while experimentally it is $\sim \pi/2$.

- Observed ratio of peak amplitudes of probe signals has not been reproduced in our model. For e.g., Ratio of capacitive probe signals of Bottom to Top and InC1 to InC5 is expected to be ~ 1 from our model. Experimentally however the signal amplitudes are significantly different.

Since the observations from multiple probes could not be explained using any trajectory of single charge vortex, presence of more than one vortex was explored in our model. Existence of such equilibrium having two charge vortices in toroidal geometry has been theoretically established by Zaveri et al [54] by solving Levy-Daughery equation for specific case of potential profile. That this is a distinct possibility can also be seen from the work of several other authors in the past [42, 157].

Expression for image current for two charge vortices undergoing diocotron oscillations in a rectangular poloidal plane of the torus is given in Equation 4.12. This has been obtained by simply applying super-position principle for image currents for different mono-poles.

$$i(t) = \frac{-q_1}{V_p{}'}\{E_{1x} \cdot v_{1x} + E_{1y} \cdot v_{1y}\} + \frac{-q_2}{V_p{}''}\{E_{2x} \cdot v_{2x} + E_{2y} \cdot v_{2y}\} \tag{4.12}$$

Here, $V_p{}'$ and $V_p{}''$ are potentials applied on a capacitive probe to calculate the image charge current resulting due to mono-pole charges q_1 and q_2 respectively. v_{1x}, v_{1y}, v_{2x} and v_{2y} are velocity components of these mono-poles, and E_{1x}, E_{1y}, E_{2x}, and E_{2y} are electric field components due to $V_p{}'$ and $V_p{}''$ respectively in the poloidal plane of SMARTEX-C. x-psoitions of the vortex are assumed to be same and obtained from the experimental probe data. y_{01}, and y_{02} are approximately guessed from the amplitude on the inboard probe signals. Poloidal velocity is assumed to be same for both the charge vortices and charge is assumed to be distributed equally between them.

Numerically computed image charge signals 4.14(aN-dN) corresponding to the trajectory for such a pair of monopoles is shown in Figure 4.14. These results are quite consistent with experimentally observed signals from various capacitive probes 4.14(aE-dE) placed inboard and outboard; the slight difference in the amplitude ratio of top and bottom probes and also between InC1 and InC5 probes could be either due to unequal charge distribution between the two vortices or inaccuracies in our guess of their y-location.

During later phases of the evolution, however, the experimentally obtained probe signals are once again consistent with the trajectory obtained due to single vortex. It is our conjecture that the two vortices merge together and form single

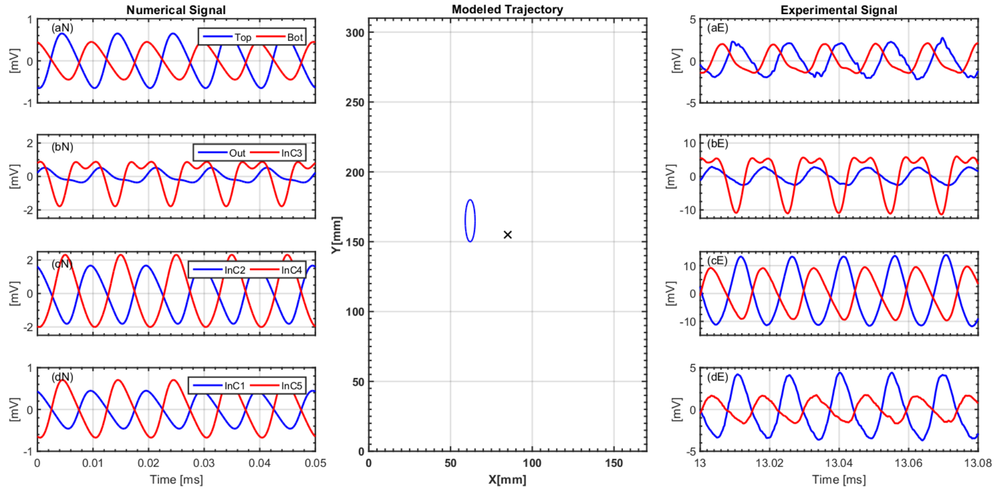

Figure 4.15: (aE - dE) Experimental signals observed on different capacitive probes at 13 ms instance of SMARTEX-C plasma shot 123, (Center) Modelled trajectory and trap center marked with label ‘X’ (aN - dN), Modelled signals calculated from derived image charge signals by solving Green’s reciprocation theorem for all capacitive probes.

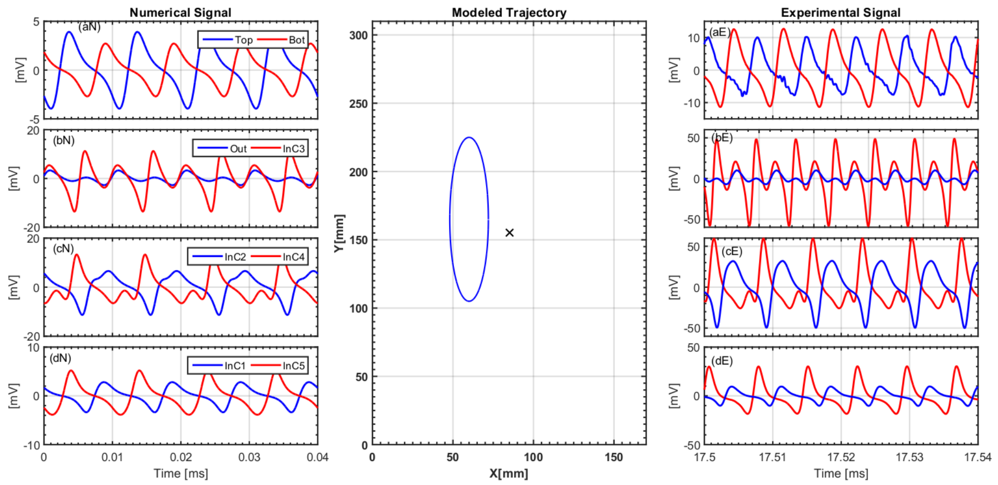

Figure 4.16: (aE - dE) Experimental signals observed on different capacitive probes at 17 ms instance of SMARTEX-C plasma shot 123, (Center) Modelled trajectory and trap center marked with label ‘X’ (aN - dN), Modelled signals calculated from derived image charge signals by solving Green’s reciprocation theorem for all capacitive probes.

vortex, time of merger being of the order of few ms. The single vortex shifts inward undergoing $E \times B$ drift in an elliptical trajectory: once again, close match with experimental signals is shown in Figure 4.15 and Figure 4.16.

Numerically generated signals for a pair of charge vortex trajectories are therefore consistent with data obtained from multiple capacitive probes in SMARTEX-C suggesting a vortex merger dynamics hitherto unreported from toroidal machines. However, further validation of the dynamics using either a space resolved charge collector or via imaging of plasma is awaited.

4.6 Discussion and Conclusion

The analytical approach developed [70] by Kapentokes et al has been adopted for a toroidal geometry and utilized to interpret experimentally observed capacitive probe signals in a small aspect ratio toroidal trap used to confine electron plasma. An expression is derived for the induced current on capacitive probes due to oscillating charges, trapped in a toroidal geometry with rectangular cross-section, consistent with SMARTEX-C. Assuming that charges are all concentrated in a point vortex, wall probe signals that would result from various simple trajectories of the charge, in the poloidal plane, have been numerically obtained.

Small amplitude circular trajectories result in sinusoidal signals and large amplitude circular trajectories give rise to sharp, saw-tooth (triangular) oscillations. Orbits that are elliptical (with respect to probe-normal) will give rise to two oscillating signals ("double-peak") in a single period of oscillation. It is also evident from our simulations that elliptical trajectories can be identified and resolved accurately in our experiments only if the eccentricity of the trajectory exceeds the threshold value compared to a probe size. The growth in amplitude of oscillations may result from the time evolution of the trajectory in one or more of the following ways: radial shift towards the probe, increase in orbit size and horizontal and/or vertical elongation of the trajectory. To distinguish between these evolving trajectories, one will need to compare signal from various probe locations. The growth rate in each case is different too. Charge loss, if included in the evolution, can cause saturation and damping of the mode oscillations.

Next, interpretation of the single probe data from SMARTEX-C in terms of vortex-like dynamics has been attempted. With reference to a probe located at the mid-plane of SMARTEX-C, four different stages of the experimentally obtained time evolving oscillatory wall probe signal, are identified based on distinctive features. These features are reproduced in numerical experiments by assuming a single vortex and an intuitive guess of the trajectory. Frequency of oscillation, poloidal velocity and initial equilibrium position of the vortex, required to ascertain the trajectory are all obtained from the wall probe data while the total charge in the cloud is obtained from charge collector. The trajectory after an initial guess is numerically evolved and tweaked so that the simulated signal matches well with the experimentally observed signal on the probe.

Suggested dynamics is largely that of a single vortex executing small amplitude diocotron motion. The motion is initially around an equilibrium position that is located inwards. The initial shift in the position from minor axis is inversely proportional to the B field. Diocotron mode frequency is inversely proportional to the B-field + *Constant*, where the *Constant* reflects the shift in position. This shift has been quantified using our non-destructive method. Initial evolution of the vortex is in the presence of a background vorticity. Due to destabilization of the diocotron mode, it evolves in time and the vortex moves radially inward with a gradual concentration of charge in the vortex. The trajectory also gradually turns elliptical. A slight shift in the vertical position of the trajectory is observed and may be due to asymmetries in the trap. The fully evolved diocotron instability is consistent with a highly elliptical trajectory closely hugging the inboard wall. The overall evolution of vortex trajectory from a center-of-charge motion to a non-linear state with the gradual shaping of the trajectory is accompanied by appearance of a large number of coupled harmonics with dominant power in the second harmonic. The power spectrum of the evolving trajectory obtained numerically is also consistent with our experimental observations.

Such a correlation may be considered over-simplified for several reasons. The simulated trajectories were, after all, only an intuitive guess and not evolved self-consistently. The correlation initially carried out with experimental data from a single probe is consistent during the later stages of evolution. But the same is shown to be erroneous when multiple probe data is included, at least during the early evolution of the mode. When data from multiple probes are correlated, presence of more than one vortex followed by a vortex merger appears a distinct possibility as has been suggested by several authors in the past [42, 54, 157]. In other words, accurate phase information obtained simultaneously from many other poloidal probes needs to be utilised consistently in validating the trajectory and hence the suggested dynamics. Certain other limitations are as follows. The charge is assumed to be concentrated in a point like vortices and the presence of a shaped charge cloud around the vortex is discounted for trajectory evaluation. Second, the present probe-size and inter probe distance (58 mm) limits the resolution of the trajectory. Velocity of the charge vortex obtained using phase information from poloidal probes is approximate; inaccuracy is more especially for small amplitude oscillations as inter probe distance is, in all likelihood, larger than the actual displacement of the cloud. For large amplitude oscillations on the other hand, the poloidal velocity is non-uniform and instantaneous velocities at several poloidal locations should be ideally used to define the trajectory more accurately. Third, only the initial evolution of the wall probe signal has been correlated in our simulations. The saturation and the damping of oscillations are, as yet, unexplained. Finally and most importantly, the derivation and hence the modelling of the trajectory has been limited to explore the possibility of monopoles undergoing $E \times B$ drift, higher order (dipole, quadrupole etc.) contributions should also be taken into account.

In spite of the above limitations, the exercise demonstrates that it is possible to ascertain the charge cloud dynamics of trapped electrons in a toroidal magnetic field in a non-perturbative method using wall probes. Inclusion of higher order components of charge cloud (dipole, quadruple etc.), higher resolution with smaller probe size and confirmation with the aid of imaging diagnostic will be a part of future work in SMARTEX-C that will help us to fully establish the vortex dynamics and role of non-uniform magnetic field in it. The insight into the charge vortex dynamics dictated by the instability was important to characterise and control the instability and achieve long-time confinement of electron plasma in SMARTEX-C, as described in subsequent chapters.

5

Investigation and Control of Instabilities in SMARTEX-C

5.1 Introduction

To achieve long time confinement of electron plasma in SMARTEX-C, investigation and control of the observed diocotron instability plays a crucial role. The observed oscillations on capacitive probes, gradually grow in amplitude before saturating and decaying and represent a typical unstable diocotron mode. The mode being negative energy mode may be driven unstable due to various collisional and non-collisional dissipative processes that draw energy from the mode and in turn cause the mode to grow. Role of the background neutrals, magnetic field strength, presence of ions, their molecular weight, electron energy, effect of wall resistance are some of the causes that have been investigated in some detail. Parameters affecting the growth rates of the instability have been identified. Primary cause has been identified as resonance of the electron cloud with ions present in the trap. Delineating the causes of the instability and mitigating measures have led to its control and a quiescent electron plasma in equilibrium.

Section 5.2 discusses the various possible causes and compares the observed growth rate with theoretical growth rates of instabilities driven by resistive wall and electron-neutral collisions and ions. Instability is identified as driven by the presence of ions and experimental growth rates are compared with theoretically estimated growth rates of classical ion resonance and transient ion resonance instability. Section 5.3 characterizes the growth rate, period of quiescence and resonance width as a function of various experimental parameters. Summary of the results and conclusion is presented in Section 5.4.

5.2 Identification of the Instability

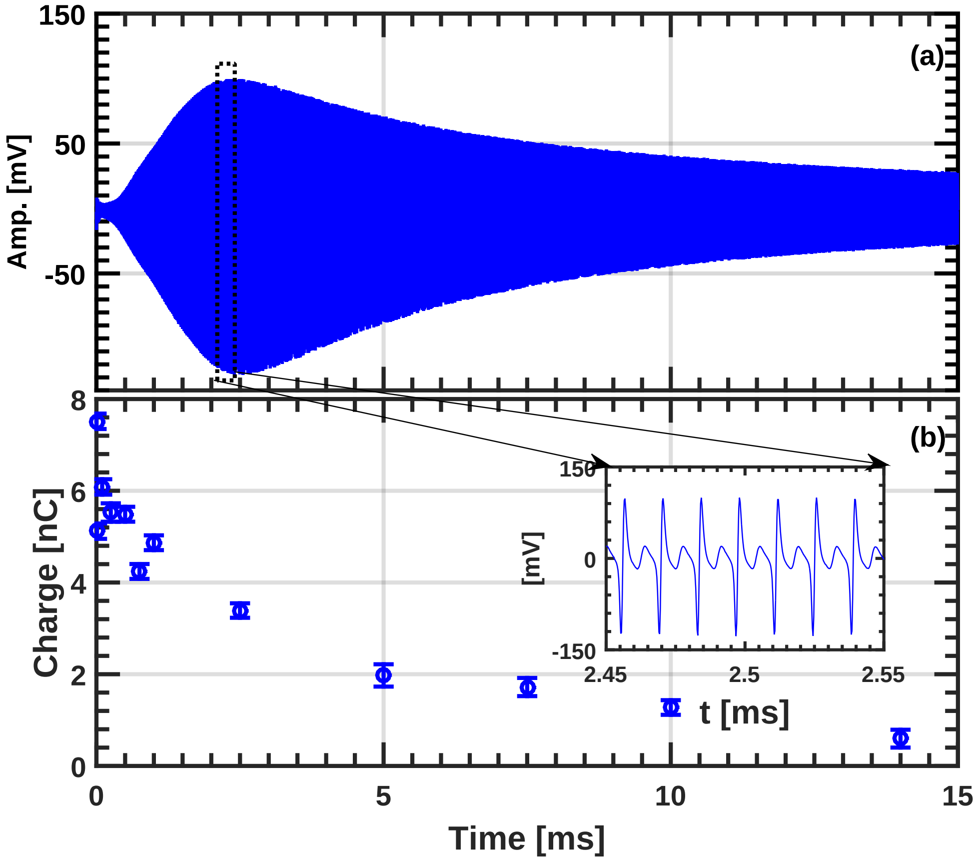

Figure 5.1: Capacitive probe signal evolution at pressure of 4.0×10^{-8} mbar and magnetic field of 200 Gauss (Inset figure shows zoomed oscillations.) (b) Time evolution of total stored charge.

Typically a trapped electron plasma held at neutral pressure of 4×10^{-8} mbar, and 200 Gauss, in SMARTEX-C, can be identified through various diagnostics as shown in Figure 5.1. Capacitive probe signal is shown in Figure 5.1(a). Injection is for 60 μs. Soon after, it evolves from coherent small amplitude nearly sinusoidal signal to large amplitude “double-peaked" oscillations. A closer look at the oscillations are shown in the inset plot. These oscillations are seen to grow in amplitude with time. As analysed in Chapter 4, this is an indication of a destabilized mode. The trap is operated in an “Inject-hold-dump" mode and the loss of the charge in time has been estimated by varying the *hold* duration and dumping the confined charge onto a charge collector. Temporal evolution of the total stored charge is shown in Figure 5.1(b). The duration of electrostatic activity observed with capacitive probes gives us a lower limit of confinement and evolution of the total charge indicates the upper limit. Both diagnostics indicate a confinement time of $\sim 5 - 10\,\mathrm{ms}$. The limited confinement time can be attributed to the transport that accompanies the rapid destabilization the diocotron mode.

The mechanism of the diocotron mode becoming unstable and leading to charge-loss can be understood as follows. While the toroidal equilibria of pure electron plasmas are well established to be a maximum energy state, the stability of the equilibrium is ensured only under certain controlled conditions. The total plasma kinetic energy is locked up in the adiabatic invariants; any perturbation from equilibrium therefore leads to release of potential energy which dissipate through well-known mechanisms. An unstable diocotron mode therefore signifies a reduction of the potential well-depth and gradual radial expansion (transport) of the plasma and eventual loss of confinement. Growth of the instability and associated charge-loss can be seen in Figure 5.1(a) and (b). The typical growth rate of an observed instability at B = 200 Gauss, $V = -300\,\mathrm{V}$ and $P = 4.0 \times 10^{-8}\,\mathrm{mbar}$ is seen to be of the order of $400 \pm 20\,\mathrm{s}^{-1}$. The growth rate is founds as follows. As already discussed in Chapter 4 amplitude of mode oscillation seen on a wall probe is a complex non-linear function of charge, position and size of the cloud. If charge loss rate is negligible enough, peak amplitde (A_{peak}) would indicate maximum displacement of the charge cloud. The inverse of the time required to reach this destabilised state is referred to as growth rate. The statistical variance of the growth rate observed for 3 - 5 plasma shots (cycles of inject-hold) is defined as the error bar. Although absolute nature of the instability growth(exponential/linear) during the evolution remains unknown, the growth rate estimation in this way would be fairly correct. Mechanisms that can drive the diocotron mode unstable, namely resistive dissipation [11], electron-neutral collisions [84, 158] and resonance with trapped [51] or transit ions [20, 90] are investigated in the following section. Each probable cause is investigated independently and ruled out based on the observed experimental growth of the instability and comparison with the theoretical estimates.

5.2.1 Resistive Wall Instability

One of the basic mechanism of the dissipation of energy and mode destabilization can occur typically due to the rearrangement of image charges on resistive boundary walls of the trap. Growth rate of such a resistive wall instability has been theoretically estimated for cylindrical geometry by White et al [11]. The same may be re-derived for toroidal geometry [121] and is given in Eq. 5.1

$$\gamma_{RWD} = \frac{\omega_D^2 A_s^2 \epsilon_o \sin^2 \Delta/2}{\pi H_s (r_{out}^2 - r_{in}^2)} \cdot \frac{R}{1 + (\omega_D RC)^2} \tag{5.1}$$

where A_s, Δ and H_s are area, toroidal angular size and height of the resistive sector respectively (inner wall or capacitive probe as the case may be), and r_{in} and r_{out} are inboard and outboard radius of the toroidal walls. ω_D is diocotron mode frequency and R & C are the resistance and capacitance of the circuit. Experiments have been carried out to identify the effect on growth rates if the trap boundaries are made resistive. In a typical experiment, outer-wall is grounded, inner-wall is grounded separately and all the capacitive probes, insulated from the rest of the trap walls, are grounded through 1 kΩ resistance as discussed in Chapter 3. For our investigations, a wall-probe has been grounded through different resistances in a set of experiment. Figure 5.2 shows the temporal evolution of the oscillation amplitude obtained from the peaks of the double-peak oscillations as seen in Figure 5.1(a). These amplitude envelopes can be used to compare the duration of electrostatic activity, peak amplitude (proportional to the maximum displacement of the charge cloud D_{max}) and growth rate of the mode. Fundamental mode frequency of the diocotron mode and its temporal evolution can also be obtained from the oscillations.

If we calculate the theoretically predicted growth rate for a typical capacitive probe (using Eq. 5.1) that is grounded through resistances ranging from 100 Ω to 10 MΩ, the growth rate is seen to vary from $1 \times 10^{-2} - \sim 2$ as shown in Figure 5.3 with dotted line. Theoretical growth rate is significantly smaller than that observed experimentally; this also implies that even if we make the capacitive

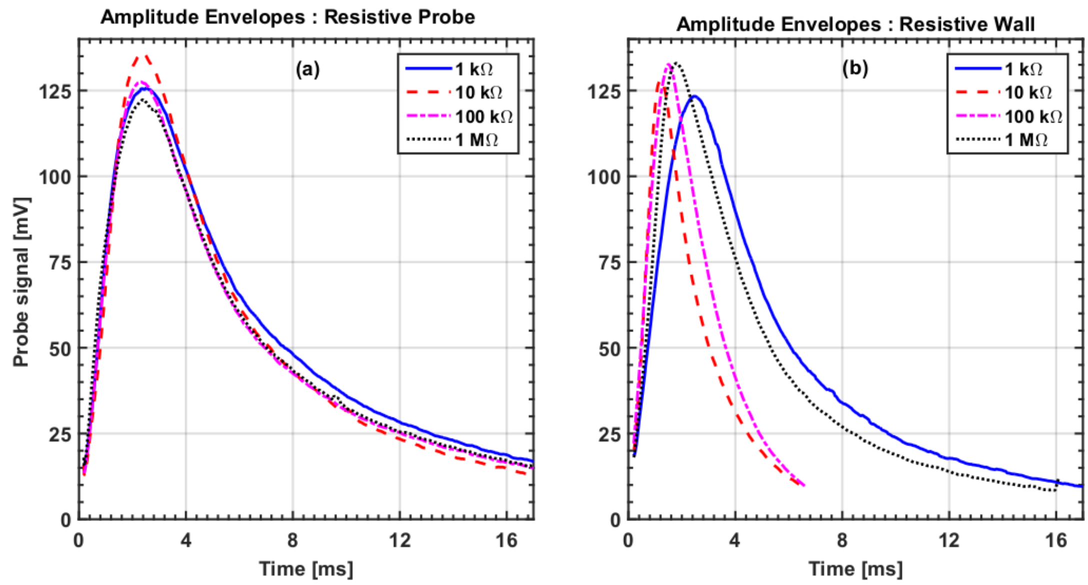

Figure 5.2: Amplitude envelopes of the capacitive probe oscillations when (a) Probe (b) Inner wall is connected to ground with different resistances.

probe increasingly resistive, its effect on growth rate shall be negligibly small and barely discernible. This can be seen in Figure 5.2 (a), where capacitive probe is terminated with a resistance varying between $1\,\mathrm{k\Omega}$ to $1\,\mathrm{M\Omega}$ and no change is observed in the growth rate of the oscillations as well as in the duration of observed electrostatic activity. This also justifies the use of $1\,\mathrm{k\Omega}$ resistance as a terminating resistor for capacitive probes, growth rate corresponding to $1\,\mathrm{k\Omega}$ resistance is shown in the Figure 5.3 with square symbol.

Any resistive electrode with large surface area can also significantly affect the growth rate. Investigation are therefore carried out by making the entire Inner-Wall (IW) grounded through different resistances. Theoretically predicted growth when the Inner-Wall is made resistive (from $5\,\Omega$ to $3\,\mathrm{M\Omega}$) is shown with a dashed line in Figure 5.3 (for assumed trap capacitance of 160 pF). Experimental growth rates (estimated from the time evolution of the amplitude envelopes) is shown in Figure 5.2(b). The growth rate increases and period of electrostatic activity decreases suggesting a decay of the plasma when the resistance connected to IW is increased from $1\,\mathrm{k\Omega}$ (solid blue) to $10\,\mathrm{k\Omega}$ (dashed red). However, beyond this the growth rate saturates and then decreases and confinement time increases again. Observed rate of growth do follow the theoretical trend although the actual values

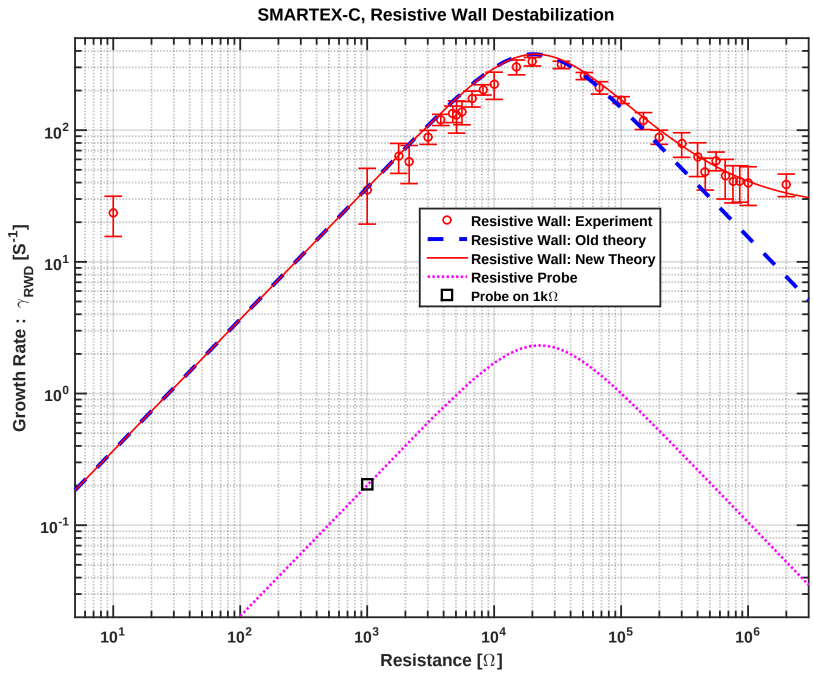

Figure 5.3: Experimental growth rate of an instability when inner wall is grounded through a resistance(circles), theoretical growth rates for toroidal resistive wall instability(dashed line) , modified theoretical growth rate (solid line) taking into account the parallel resistive path between Inner Wall and vessel. Theoretical growth rate for resistive capacitive probe is also shown(dotted line), square point shows the growth rate corresponding to capacitive probe terminated with 1 kΩ.

in these experiments were higher than the predicted values by few factors ($400\,\mathrm{s}^{-1}$ to $850\,\mathrm{s}^{-1}$). Experimental values are not shown in the figure.

These observations suggest that resistive wall (IW) definitely destabilizes the mode but when two or more driving factors (viz., background neutral density, presence of ions etc) simultaneously exist the observed growth rates can be significantly different. To delineate the effects of resistive wall from that of neutrals/ions and to minimize the effects of other concomitant mechanisms, experiments have been carried out at lower base pressure of 4×10^{-9} mbar. Now the observed experimental growth rates as a function of resistance is shown in Figure 5.3 with circles. The errorbar is obtained after carrying each experiment for 4 - 5 times. The theoretical growth rates for various resistances connecting the entire inner wall to the ground are plotted (dashed line) in Fig. 5.3 where trap capacitance of $C \sim 160\,\mathrm{pF}$ is used as a fit parameter. The experimental growth rates of the resulting diocotron instability now compare well with theoretical estimation as shown in Figure 5.3 for resistances ranging from $1\,\mathrm{k\Omega}$ to few $100\,\mathrm{k\Omega}$. For resistances lower than $1\,\mathrm{k\Omega}$, there is a finite but slow growth, which could still dictated by other destabilizing mechanism such as neutrals/ions. At higher values of resistances ($1\,\mathrm{M\Omega}$ and beyond) the growth rate deviates from theoretical predictions; this is due to the parallel path of the IW with vacuum vessel due to insulators placed to isolate it from the rest of the system. If one takes into account this parallel resistance in the path then the expression for growth rates will get modified as follows [159]:

$$\gamma_{RWD}^{New} = \frac{\omega_D^2 A_s^2 \epsilon_o \sin^2 \Delta/2}{\pi H_s (r_{out}^2 - r_{in}^2)} \cdot \frac{R\big(1 + \frac{R}{R_{Ins}}\big)}{\Big(1 + \frac{R}{R_{Ins}}\Big)^2 + (\omega_D RC)^2} \tag{5.2}$$

For $R_{Ins} \sim 500\,\mathrm{k\Omega}$, theoretical growth rate agrees very well with experimental data as shown in Figure 5.3 with solid line.

As the trap capacitance plays an important role, an additional external capacitor was connected with the Inner-Wall. This too destabilized the mode. Similar trends in the growth rate were observed. Frequency shift associated with resistive wall destabilization was not discernible due to other dominating frequency shifts. We finally conclude, that as walls of the vacuum chamber in SMARTEX-C (including inner wall) are grounded and the observed growth rate of instability is at least two orders of magnitude higher than the maximum growth predicted by resistive wall-probes, it may be safely ruled out as the driving mechanism for diocotron instability in SMARTEX-C.

5.2.2 Ion Resonance Instability

With resistive wall instability ruled out, the effect of background neutrals on the growth of instability and charge loss has been investigated. Transport can be envisaged due to electron-neutral (e-n) collisions. Theoretically predicted growth rates of diocotron instability due to e-n collisions [84] are of the order of $\approx 6 \times 10^{-3}\,\mathrm{s}^{-1}$ (for $P = 1 \times 10^{-8}\,\mathrm{mbar}$, $B = 200$ Gauss and $f_{Dioc} = 50\,\mathrm{kHz}$) as estimated from $\gamma_{e-n} = \frac{\nu_{e-n}}{\omega_{ce}} \omega_{Dioc}$. Estimate of growth rate of instability due to e-n collisions therefore appears orders of magnitude slower than that observed in SMARTEX-C ($\sim 400 \pm 20\,\mathrm{s}^{-1}$) and hence it can be safely presumed that collisions with neutrals are not responsible for driving the mode unstable in this case.

However, presence of neutrals, can also lead to rapid ion formation due to electron-impact ionization mechanism. As postulated by Levy et. al [48] when the trapped ion population (in the electron potential well) oscillates with a frequency close to that of the off-axis diocotron oscillation of the electron column, ions draw energy from the mode; this resonance drives the mode unstable and degrades the plasma confinement. Ion driven instabilities have been widely reported from cylindrical [20, 160] as well as recent toroidal traps [61] and stellarators [161]. While classsical ion resonance instability as postulated by Levy et. al requires a set of ions trapped permanently in the electron cloud, what has been reported from some cylindrical traps are more likely due to transient ions that are continuously formed and leave the trap due to the negative electrostatic potentials on the end plugs [20,89]. Possible role of background ions in the rapid growth of the instability in SMARTEX-C therefore merits due consideration.

Energetic electrons ($\sim 300\,\mathrm{eV}$) emitted thermionically from filament can cause ionization of background gas via electron-impact ionization. Wall emissions are also expected to add to the neutral population. Ionization rate (ν^+) at these electron energies and at typical pressures of $1 \times 10^{-8}\,\mathrm{mbar}$ is $\sim 40\,\mathrm{s}^{-1}$ (ionization cross-section N_2 (σ_N) $\sim 2 \times 10^{-20}\,\mathrm{m}^2$). The ion oscillation frequency trapped in the electron plasma potential well is $\approx 56\,\mathrm{kHz}$ (for $n_e \sim 1 \times 10^6\,\mathrm{cm}^{-3}$) which closely resonates with the diocotron frequency $50 - 60$kHz observed in SMARTEX-C, making conditions suitable for the onset of the ion resonance instability [51, 87].

To investigate the role of ions, experiments were performed at different neutral pressures. Temporal evolution of mode oscillations, as seen from wall probes, for representative set of experiment is shown in Figure 5.4 (a-e). Low initial background pressure in the trap helps in delaying the onset of instability and also arrests the growth rate.

Observed growth rates of instability are plotted in Figure 5.5. For a gas like Nitrogen it increases with pressure (shown with circles). Fractional ionization was reduced by introducing He neutrals in place of N_2 in the trap. With ionization cross-section of He nearly an order-of-magnitude less ($\sigma_{He} \sim 0.3 \times 10^{-20}\,\mathrm{m}^{-2}$) the rate of ionization of He ($\nu_+ \sim 6\,\mathrm{s}^{-1}$) is reduced by a factor of $6 - 7$ (for $\sim 300\,\mathrm{eV}$ electrons at $1 \times 10^{-8}\,\mathrm{mbar}$). Growth rates with He neutrals are evidently lower than that with N_2 for equivalent pressures, and is plotted with square symbols.

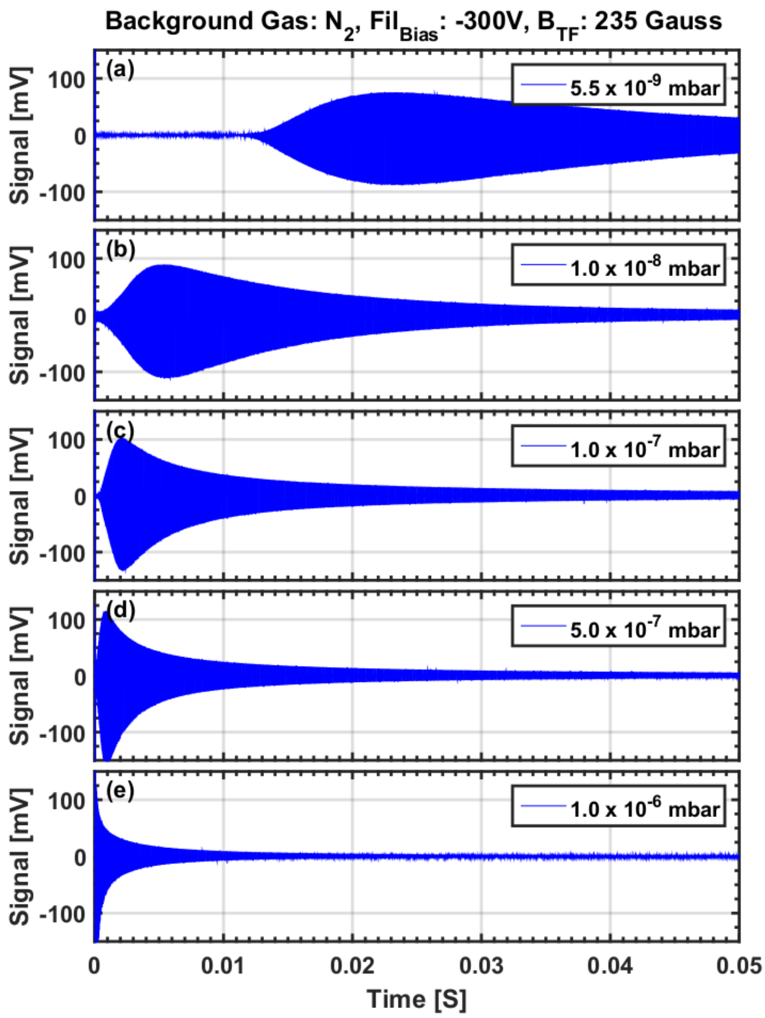

Figure 5.4: (a)-(e) Time evolution of capacitive probe oscillations at different background neutral pressure of Nitrogen gas.

For comparison, theoretically estimated growth rates for collision driven diocotron instability (for Nitrogen neutrals) is also plotted (dashed-dot) and is seen to be much less.

So ions unambiguously affect the instability. However, experimental growth rates with say, Nitrogen, do not seem to match those estimated from Levy's theory (dashed line in Figure 5.5). Surprisingly, experimental growth rates are much less even though ion build up in the trap is expected to be very fast. Say, in a span of 2.5 ms $\sim$ 100% ionisation would be expected when background pressures in the

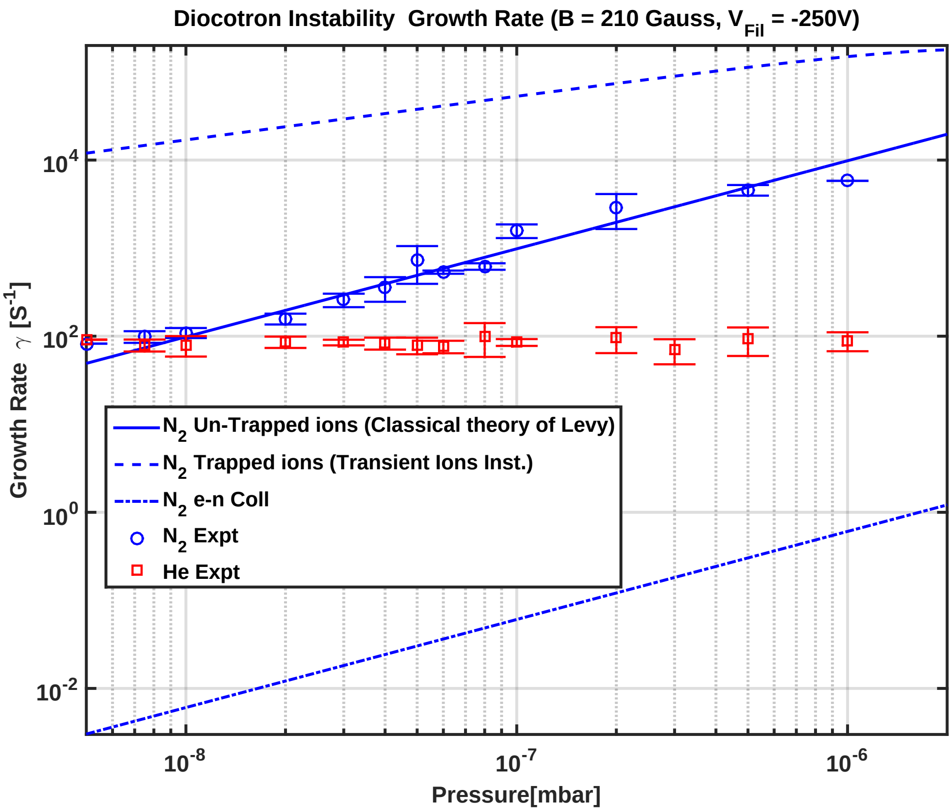

Figure 5.5: Experimental growth rate of the diocotron instability with neutral pressure of Nitrogen (circles) and Helium (squares). Theoretical growth rate of diocotron instability driven by electron-neutral collision (dash-dot), transient ion resonance(solid) and trapped ion resonance instability(dashed) for Nitrogen.

trap is 1×10^{-7} mbar. Evidently the build up of ions is countered by a sink that dampens the growth.

As stated before, SMARTEX-C has negatively biased end-grids; ionisation of background neutrals will therefore be concomitant to steady loss of ions to the grids. Ions born at room temperature (0.03 eV) can stay in the trap length of 75 cm for $\sim$ 500 µs before getting lost via the end grid. Simultaneously, new ions can be formed even while the plasma is held in the trap as the trapped electrons bounce axially between grids with a $T_{\parallel}(max) = 300\,\text{eV}$ and collide with the residual neutrals. So, to attempt a possible explanation for the above noted discrepancies, we explore the possibility of a transient ion population driving the mode unstable [20, 89, 90]. as opposed to a trapped ion population. The relevant growth rates for comparison are therefore given as

$$\gamma_{th} = \frac{\nu^+ r_p^4}{\lambda(1 - r_p^4)} \tag{5.3}$$

where, $\lambda (= \frac{2\epsilon_0 B^2}{m_i n_e})$ is ion magnetization parameter, r_p is normalized plasma radius and ν^+ is ionization rate. If now the theoretical growth rates are to compare well with the observed growth rates (see Figure 5.5 solid line) best fit is obatined for r_p assumed to be of the order or $0.75 - 0.9$ (normalized by wall radius of 8.5 cm). This suggests a plasma radius of $6.4 - 7.6$ cm which is reasonable. However, in the absence of any direct measurement of the plasma radius, we are unable to comment any further on the actual nature of the growth.

5.3 Characterization of the Instability

Soon after injection, the complete evolution of the plasma may be divided into three distinct phases. a) Quiescent phase : A period when no-electrostatic mode or activity can be detected in the plasma. During this period, the plasma may be undergoing small amplitude stable diocotron oscillations around the equilibrium position or maybe weakly unstable such that it is not detectable on the capacitive probe (signal below the noise floor). We also believe continuous production and loss of ions is on-going at this stage leading to a gradual ion-build up (b) Growth phase : Once a sufficient number of ions are present in the trapped electron-plasma and if the conditions for resonance prevail, the diocotron mode will become unstable and grow. The growth in oscillation amplitude is a complex function of the total charge, displacement of the charge cloud from equilibrium (displacement - D), size of the charge cloud, electric-field and magnetic field. For simplified analysis only normalized growth rates are calculated. Normalization process is carried out with respect to peak diocotron oscillation amplitude. Peak diocotron mode amplitude may be interpreted in terms of the maximum displacement of the charge cloud from its equilibrium position, and has resulted due to competitive processes that determine the growth and damping of the mode. (c) Damping phase : Various possible mechanisms like rotational pumping, magnetic pumping, Landau damping or resonant particle driven processes may be damping the mode. In present studies, damping mechanism of the mode is not in the scope of investigation.

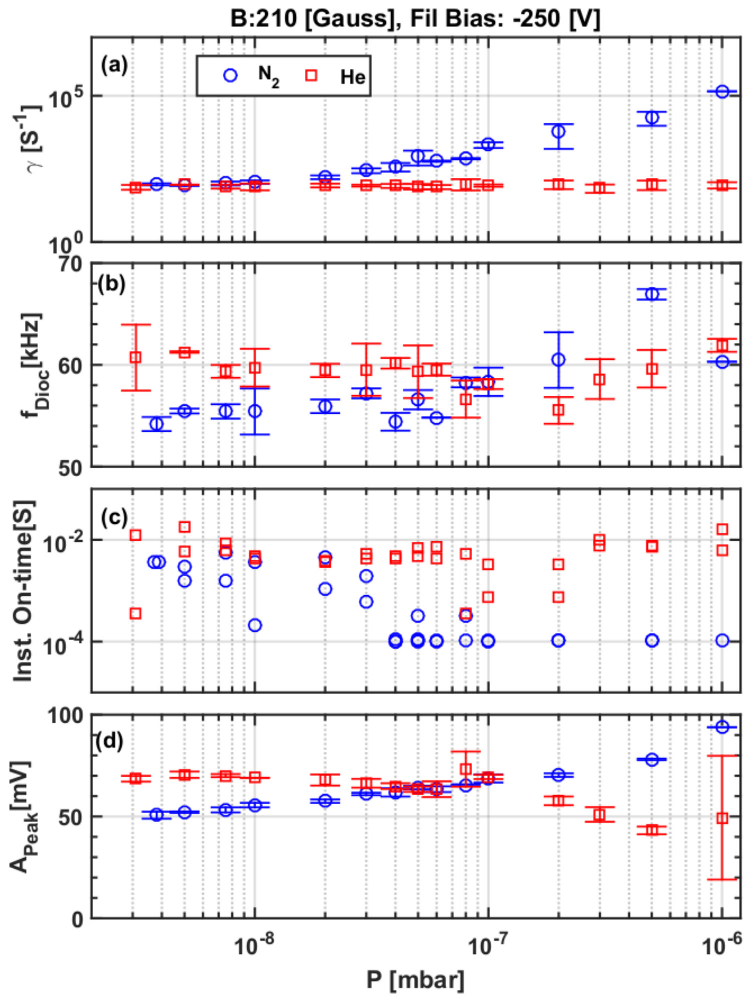

Figure 5.6: (a)Growth rate of the instability (b)linear diocotron mode frequency (c)instability onset time (d) peak diocotron mode amplitude versus pressure for Nitrogen (circle) and Helium (square).

Figure 5.6(a)-(d) shows growth rate, small-amplitude diocotron mode frequency, instability onset time (quiescent time) and peak amplitude of diocotron oscillations as a function of neutral pressure for Nitrogen and Helium gases. It may be remembered that He has lower ionisation cross-section. Instability grows by three orders of magnitude for pressure rise of two orders in case of Nitrogen whereas Helium shows almost negligible growth over the same pressure range.

Mode frequency for N_2 increases with pressure due to increase in electron density caused by electron impact ionization; in contrast with He there is no such trend. Period of quiescence increases as pressure is lowered for N_2 but with He the effect is negligible. Peak oscillation amplitude is higher at higher pressures in case of N_2 owing to faster growth rate (rapid destabilization) whereas with He it actually reduces. With reduced ionisation, He neutrals could be leading to damping through electron-neutral collisions.

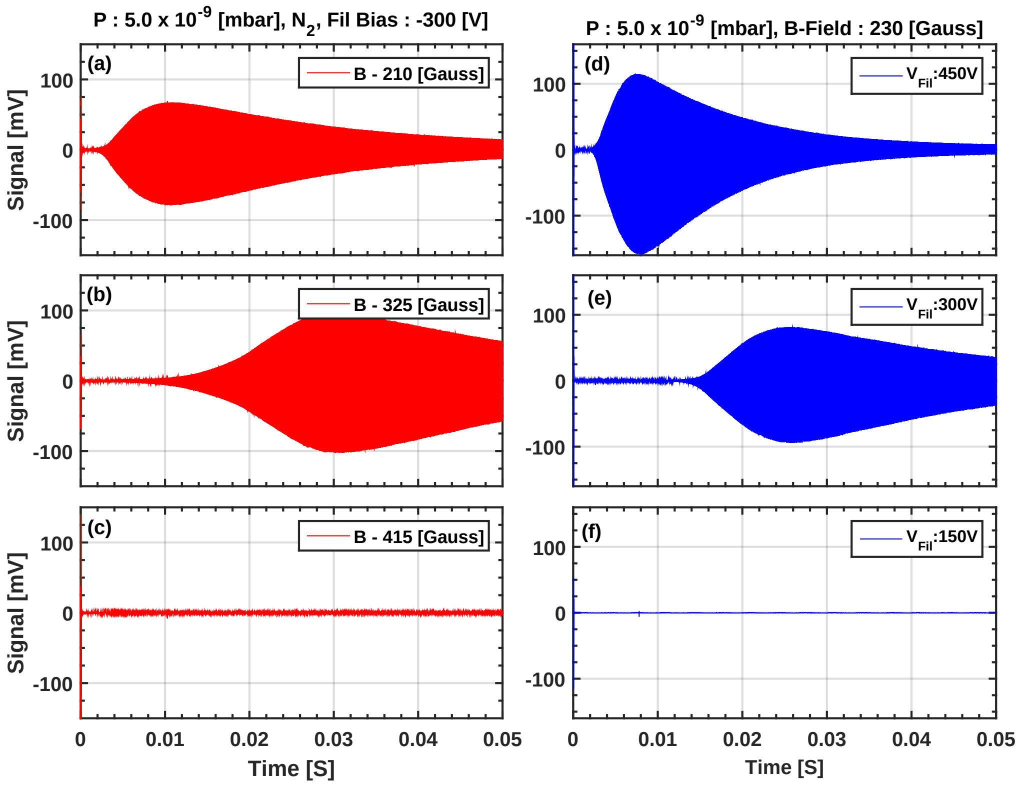

Figure 5.7: (a) - (c) Time evolution of capacitive probe oscillations at different magnetic field (d) - (f) different injection energy.

In addition to neutral pressures in the trap, toroidal magnetic field and electron injection energy are other parameters that affect the instability. A sufficiently strong toroidal B field helps in inhibiting the growth of instability triggered by any build-up of ion population. In Figure 5.7(a-c), for background pressures 5×10^{-9} mbar ($\nu^+ \sim 20\,\mathrm{s}^{-1}$), the transition to large amplitude non-linear oscillations is shown to be successfully delayed and damped by raising the B field from 210 Gauss to 415 Gauss. At similar background pressure, when one reduces the electron injection energy from 450 eV to 150 eV, appearance of the mode can be delayed and the control over growth rate can also be achieved as shown in Figure 5.7(d)-(f).

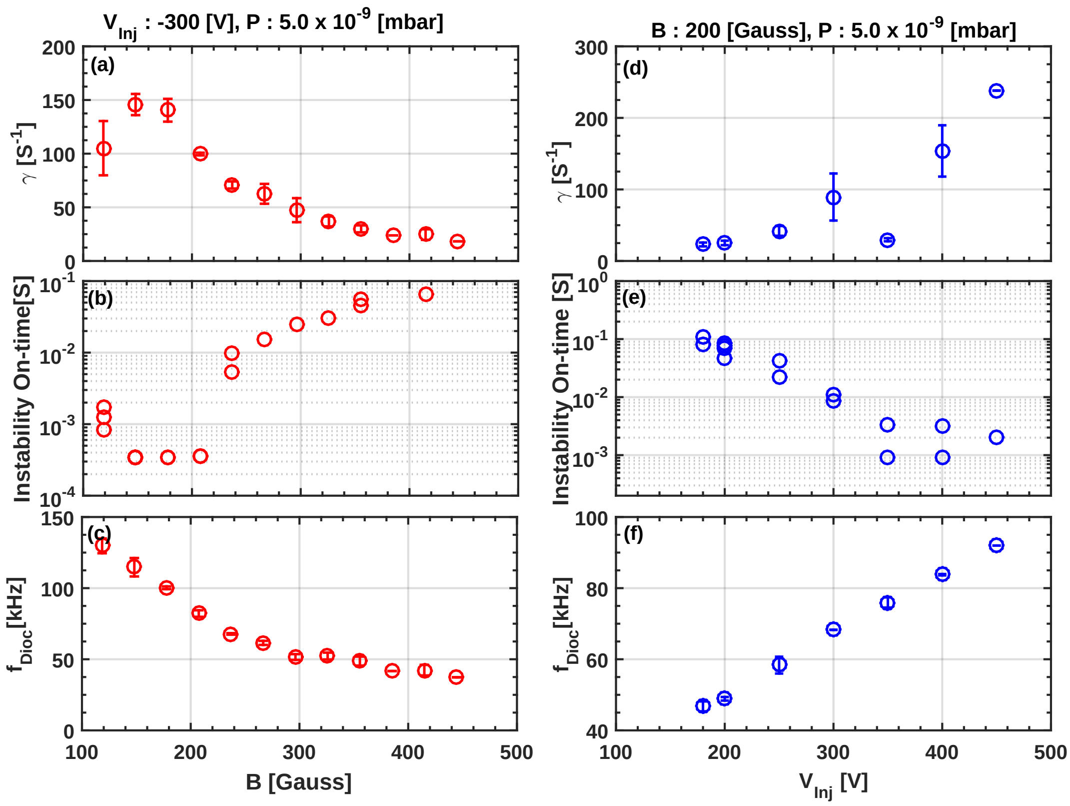

Figure 5.8: Characterization of instability (a)growth rate and (b)onset time and (c) diocotron mode frequency as a function of magnetic field and (d) - (f) as function of electron injection energy.

The effect of B on growth rates, instability onset time (period of quiescence) and linear diocotron mode frequency are plotted in Figure 5.8(a)-(c). The increase in B reduces the mode frequency (~ 40 kHz) and it is likely that it shifts away from the resonant ion oscillation frequency (~ 75 kHz). This arrests the instability. The shift from resonance also happens when we reduce the B field and the resonance curve is a tell-tale signature of ion resonance instability. Observed growth rate has a $\frac{1}{B^{2.5 \pm 0.15}}$ dependency on magnetic field, which closely matches with theoretical dependency of B^2 (for r_p assumed to be in the range of $0.7 - 0.8$). Other than the obvious effect on frequency, B field also affects the ion-build up rate in the trap. When ion production rate is kept constant by keeping the pressure and electron injection energy constant, any increase in B-field reduces the path length at constant perpendicular velocity and thus increases the loss rate. This slows down the rate at which ions build up and onset of the instability gets delayed as seen in Figure 5.8(b).

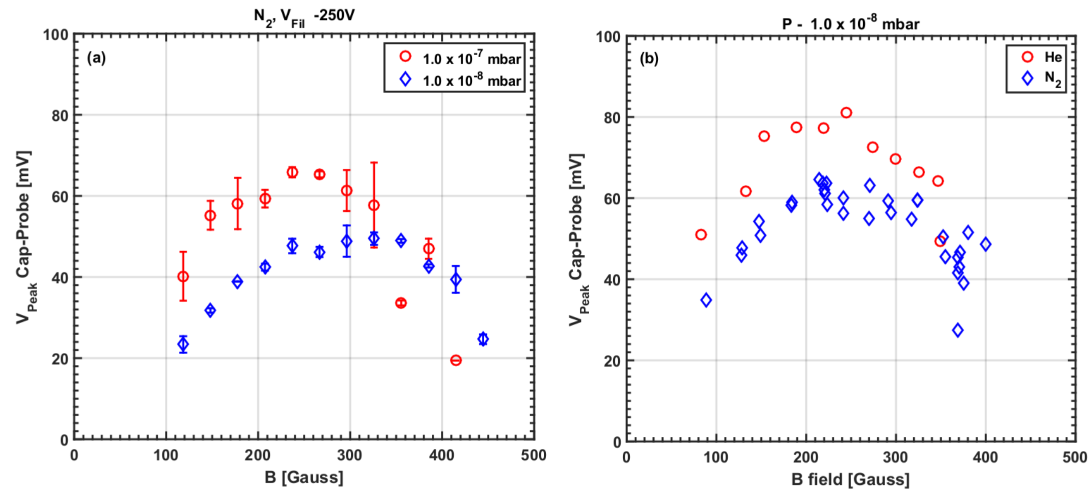

Figure 5.9: Resonance curves in magnetic field parameter space at (a) different pressures and (b) with different gases.

The effect of electron injection energy on mode oscillations seen in Figure 5.7(d)-(f) has been analysed in terms of growth rate, instability onset time and linear diocotron mode frequency in Figure 5.8(d)-(f). Observed increase in growth rate with electron injection energy is due to higher ion production rate ($\nu^+ = n_n \sigma v$) as electron impact velocity, $v \propto V_{Inj}^{0.5}$. Although the impact ionization cross-section reduces with increase in energy the dependency is weak as seen in Figure 5.8(d). As the production rate increases, onset time also becomes shorter. Increase in linear diocotron mode frequency with V_{Inj} is a clear signature of increased electron plasma density. It should be noted that period of quiescence is very sensitive to various parameters and its poor reproducibility can be observed in Figure 5.8(b) in which instability onset time $\sim 300\,\mu$s is frequently observed.

In addition to this, if one investigates the dependency of the peak mode-amplitude on magnetic field for various experimental parameters i.e. background neutral pressure, different gas and injection energy, one finds very broad resonance curve as shown in Figure 5.9(a) and (b). If we assume A_{Peak} to be the maximum displacement D_{max}, it represents the value of magnetic field for which maximum destabilization of electron plasma occurs. For a given experimental parameters, the A_{Peak} has resulted due to competing processes that drive the growth and damping, resulting in a saturation of amplitude (A_{Peak}). As the exact damping process and its dependency on other experimental parameters have not been investigated, there would be some reservations in calling these curves as the typical resonance curves in spite of the fact that they are observed across all experimental conditions.

5.4 Discussion and Conclusion

Observed instability in the SMARTEX-C trap has been delineated from other instabilities by comparing their theoretical growth rates with experimental ones. Instabilities driven by electron-neutral collisions and resistive walls have been thereby ruled out. The observed growth rates and effect of different experimental parameters suggest that instability is largely driven by ions and akins to the ion-resonance instability seen in cylindrical and toroidal traps. The experimental growth rates though do not quite match the theoretical estimates predicted by classical theory which envisages trapped ions with growth rates being two orders of magnitude smaller. This has been ascribed to transient ions where ions are continuously formed and also lost towards negatively biased end-grids in SMARTEX-C. Ion population in the trap is a function of source (energetic electrons driven electron impact ionization of background neutrals) and sink (negatively biased end-grids) parameters. The qualitative behavior and growth rates are in good agreement with theoretically predicted growth rates of transient ion resonance instability for weakly resonant ions and within the uncertainties in determination of experimental parameters such as τ, n_0 and spatial density profile and assuming a plasma radius in the range of $\sim 6 - 7\,\text{cm}$.

Width of the observed resonance curve is broad in nature as is observed for transient ion-resonance instability. In SMARTEX-C this is possibly due to two reasons: a) More than one ion species might be participating in destabilizing the plasma which would result in broader resonance curve; such a possibility is endorsed by the RGA spectrum. b) Inhomogeneous toroidal B-field would cause the ion cyclotron frequency to have a wide range of ions spread over the entire plasma column, and cause the resonance to occur over a broad range of diocotron frequencies.

Growth rate depends on the ion density but dependency couldn't be determined due to difficulties in measurement of very feeble ion current. Most strikingly, threshold ion density required to trigger the instability was observed to have a broad range. Below this threshold ion density, the quiescent phase of electron plasma is observed and this might simply be that ions are shielded by electron column and do not get accelerated towards the end grids. In this situation, classical ion resonance instability for trapped ions shall govern the stability.In cylindrical traps the displacement of the plasma can be accurately measured and defines the growth rate of the instability. In SMARTEX-C, the nature of instability growth(linear or exponential) cannot be ascertained from the wall probe signal oscillation amplitude due to its complex dependency on charge content, displacement of plasma, size of the plasma and temperature of the plasma; time dependency of these parameters further complicates the interpretation. Measurement of ion current along with estimation of plasma displacement with time and role of 3-D effects coming due to toroidicity shall explain the exact nature of growth etc and remains in the scope of future work.

Inspite of this shortcomings, the instability has been characterised over a wide range of parameters that govern it and the growth has been controlled by series of measures leading to a vast improvement in confinement time. Appropriate parameter regime has been found where instability gets suppressed and completely quiescent electron plasma for entire B-field pulse length can be produced. With instabilities arrested, charge loss reduces and the plasma is seen to last for a time of the order of B-field pulse length $> 1\,\mathrm{s}$, as discussed in next chapter.

6

Long-time Confinement of Electron Plasma in SMARTEX-C

Toroidal traps historically plagued by poor confinement had a turnaround in the late 90's and early 2000. Two of these traps with purely toroidal magnetic field, were converted into partial torus in order to combine the technique and advantages of cylindrical traps with toroidal geometry. Successful trapping of non-neutral plasma was thus realised in such partial toroids, namely in LNT-I [61] which was a large aspect ratio device and in SMARTEX-C [63], a small aspect ratio trap. In intial experiments significant improvement in confinement were reported but was primarily limited due to non-toroidal effects, such as presence of instabilities (mostly driven by ions). With improved operating scenarios like enhanced vacuum, higher magnetic field and a higher degree of symmetry LNT-II successfully confined toroidal electron plasma in a steady state confinement for 3 s [60,64,162]. Reported confinement time approached the limit set by Magnetic Pumping Transport (MPT) [59] (for the trap major radius of 17.4 cm and assumed temperature of 1 eV), which has been presumed to be the theoretical limit of confinement in toroidal traps. Direct experimental evidence of MPT in toroidal devices is however still awaited.

Around the same time, SMARTEX-C, had reported confinement that lasted for the entire duration (4 ms) of its pulsed magnetic field. While extending the magnetic field was essential for long time confinement, our experiments also proved that doing so alone would not extend the lifetime due to the strong presence of instabilities. This led us to undertake a major upgrade of SMARTEX-C on two fronts. The Pulsed Power Supply was replaced by a DC power supply that allowed us to carry out trapping in the presence of a steady state B field of 9×10^2 Gauss for several seconds. Redesigned TF coil allowed the operation of TF coil at low magnetic field for as long as 60 s and for several seconds at high magnetic field of 9×10^2 Gauss. The vacuum system was also upgraded to allow experiments over a range of pressures where various instabilities can be delineated, identified and controlled. Additional diagnostics like externally launched diocotron modes were instrumented to estimate the confinement time in a quiescent plasma. All of these measures have been discussed in detail in Chapter 3.

An upgraded SMARTEX-C helped us in identification and characterisation of the instabilities as discussed in Chapter 5. Having identified the dominant instability to be one driven by trapped ions, the growth of instability was arrested by de-tuning the driving parameters. A quiescent electron plasma at equilibrium is thus produced. By launching the $m = 1$ diocotron mode, the total stored charge (a function of the fundamental diocotron frequency) is estimated as a function of the time; e-folding time of decay of the initially injected charge is defined as confinement time. All of these have successfully helped us to demonstrate an improvement in the confinement of electron plasma by 5 orders of magnitude, where plasma remains in a steady state equilibrium for $\sim 100 \pm 10$ s. Taking advantage of the improved confinement, existing transport theories and estimated time scales have been reworked for our small aspect ratio geometry and discussed vis-a-vis our confinement times .

6.1 Effect of Control of Instability on Confinement Time

As discussed in Chapter 5, the control of the diocotron instability has been demonstrated at higher B fields and/or lower background pressure. The effect on charge loss is showed in Figure 6.1(a) and (b). Trapped charge present at different instances following injection is measured by dumping the charge onto a charge collector. The rate of charge loss reduces and confinement vastly improves from 15 ms to more than 60 ms as pressures are appropriately lowered and B field is increased.

Under these conditions the instability though is not fully suppressed. As pressure is further lowered to 2.5×10^{-8} mbar, very low amplitude diocotron oscilla-

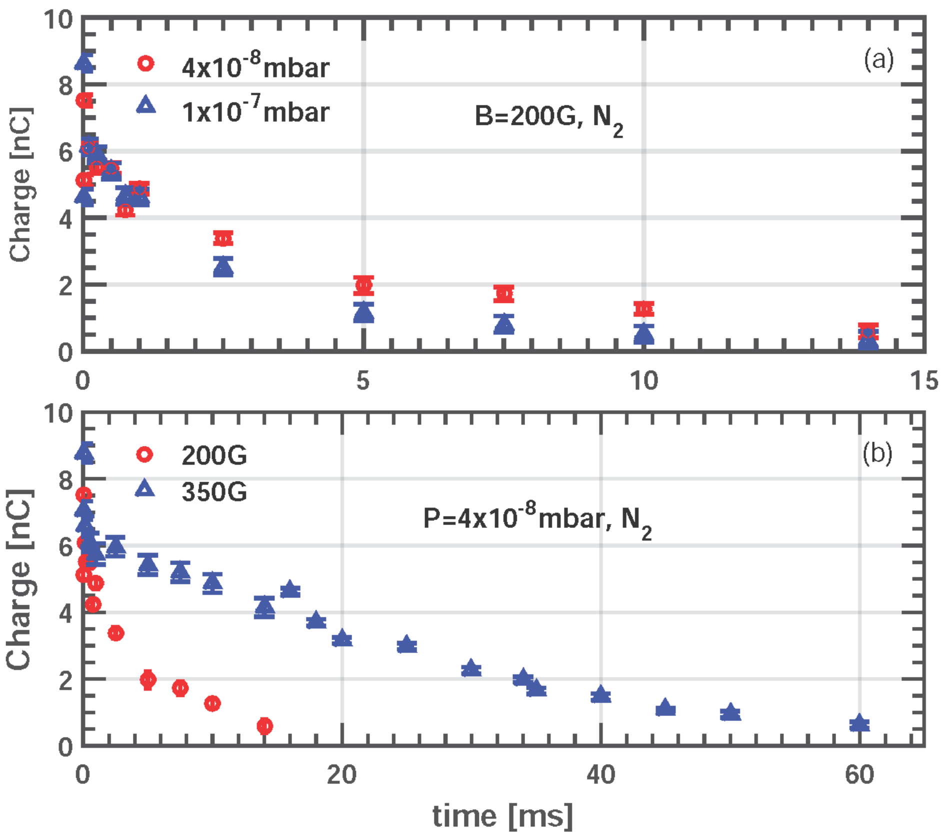

Figure 6.1: Time evolution of trapped charge at two different (a) pressure and (b) magnetic field.

tions are observed at very small growth rate in the initial phase of the evolution. However the instability is triggered once again and the mode oscillations gradually grow to non-linear amplitudes(See Figure 6.2 (a)). However, the charge loss rate is almost absent till 30 ms and picks up only after the oscillations have grown to a fairly large amplitudes. The confinement then degrades as seen from Figure 6.2 (b).

The temporal evolution of diocotron mode frequency during this period is interesting and is shown in Figure 6.2 (c). If the frequency is considered to be a measure of the line density and is related to the total charge, the initial evolution may suggest a rearrangement of the density profile. However, what complicates the inference is a nearly 12% drop in B field observed to happen in ~ 25 ms. The

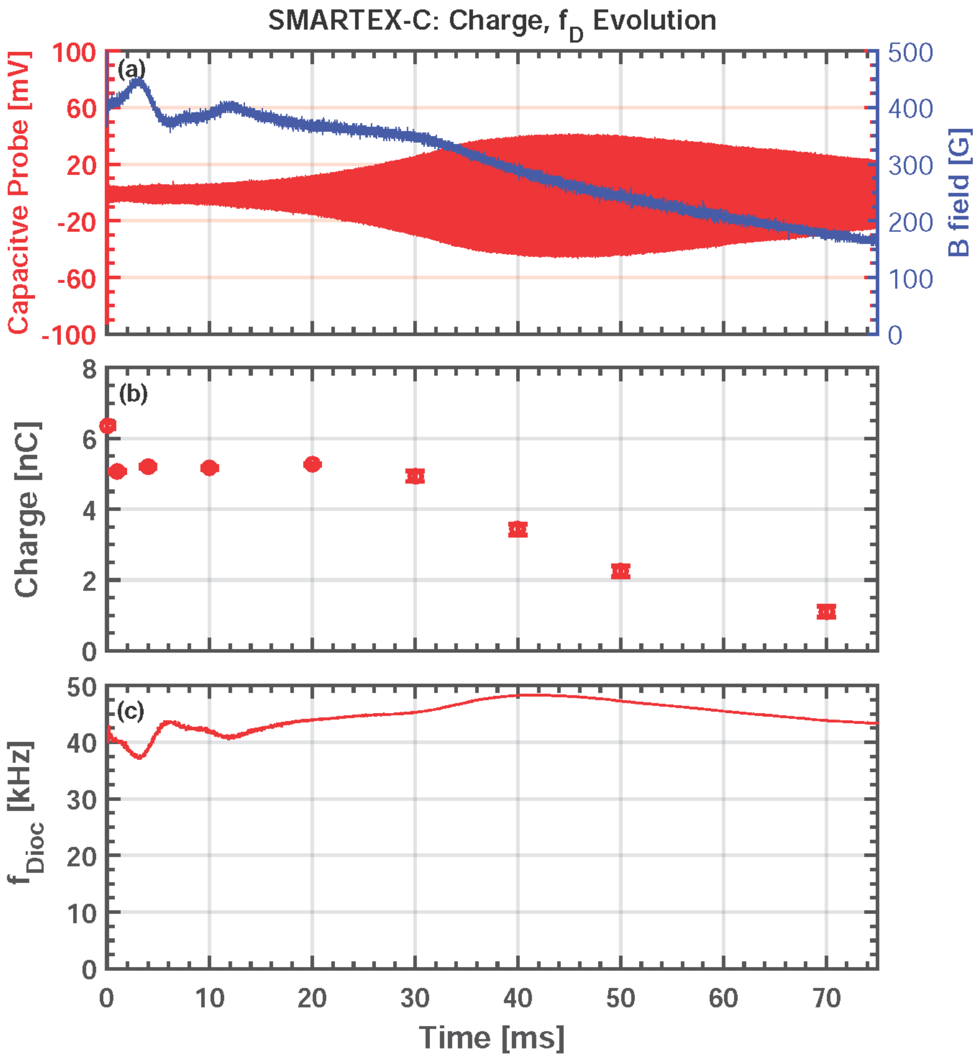

Figure 6.2: Time evolution of (a) Capacitive probe data (b)Evolution of total stored charge in SMARTEX-C obtained using charge collector diagnostics for electron plasma produced at 2.5×10^{-8} mbar and 400 Gauss (c) Diocotron mode frequency from capacitive probe data.

drop in current is largely due to a resistive toroidal field coil. The resulting drop in B also shows up in the frequency evolution. These results suggest the requirement of steady state magnetic field with a minimum droop. Only then can the evolution of the frequency be related to the charge evolution and an externally launched diocotron mode and its frequency evolution be of any help in diagnosing the confinement time especially in those cases where the plasma is quiescent and naturally occurring diocotron mode is absent.

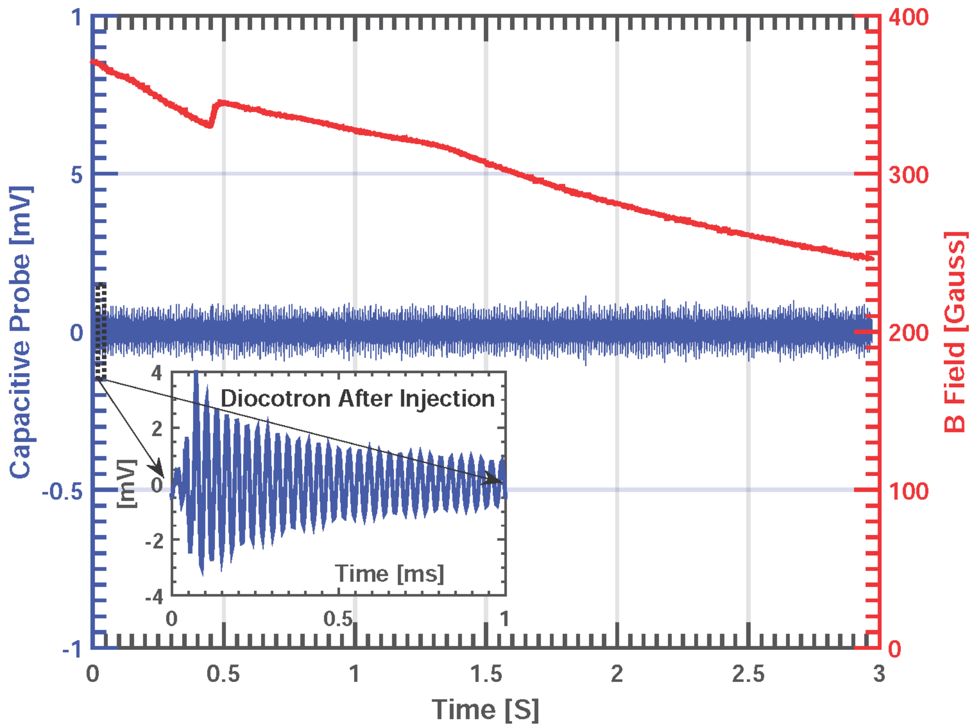

Figure 6.3: Quiescent capacitive probe signal for 3 s along with drooping magnetic field. Inset plot shows damping of diocotron instability soon after injection is over.

When pressures are lowered to less than 1×10^{-8} mbar, the instability is seen to remain suppressed for as long as 3 s at 380 Gauss. The wall probe signal resulting from such a quiescent plasma is shown in Figure 6.3. Except for the initial diocotron oscillations which quickly damp within few hundred oscillations after injection, there is no detectable electrostatic activity.

To obtain the lifetime in the absence of any observable naturally occurring diocotron oscillations, the presence of the plasma had to be established by launching the diocotron mode externally (as has been the practice in cylindrical machines). Wall probes, placed on inner and outer walls, has been used as exciter electrodes. A frequency burst with 180^o phase difference is applied on poloidally opposite inboard and outboard electrodes (toroidally located 120^o away from the filament).

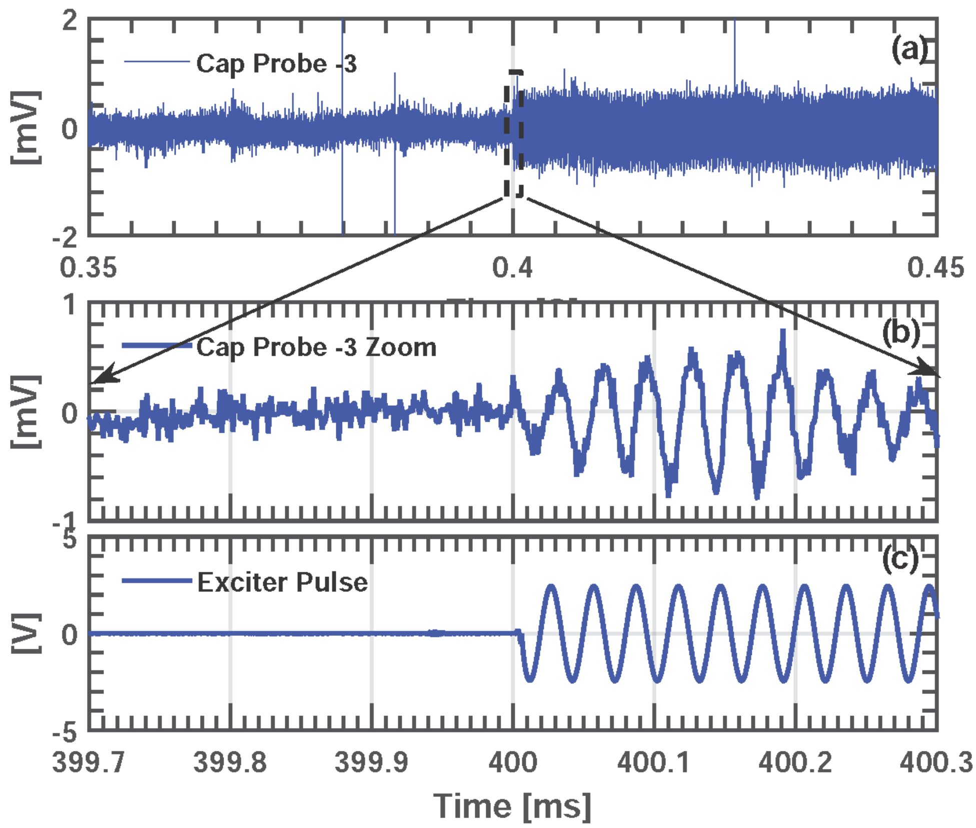

Figure 6.4: (a) Diocotron mode (b) Zoom diocotron mode (c) Exciter pulse.

In order to identify the resonance frequency at any particular instant every launch is preceded by a test shot. A frequency chirp of 10 oscillations with $\Delta f = 2\,\mathrm{kHz}$ is applied to the exciter electrode for about 1 ms. The mode gets launched at the resonance frequency but the sweep of frequency results in additional perturbations. The frequency of the initial small amplitude oscillations in the test shot is chosen now as the resonant frequency, and instead of a sweep, a burst of 10 oscillations at resonance (fixed) frequency is then applied to launch the mode. Amplitude of perturbation is controlled to less then $5\,\mathrm{V_{p-p}}$ to prevent the linear mode from getting destabilised. A typical launch of the linear diocotron mode is shown in Figure 6.4. The wall probe signal due to the launched mode is shown in Figure 6.4(a), the initial small amplitude oscillations representing the linear diocotron mode is shown in Figure 6.4 (b) and the corresponding exciter pulse applied on inboard capacitive probe is shown in Figure 6.4(c). Launched mode for a few selected instances are shown in Figure 6.5(a)-(c). The observed linear diocotron frequency (at $B = 380$ Gauss) is plotted with time in Figure 6.5(d).

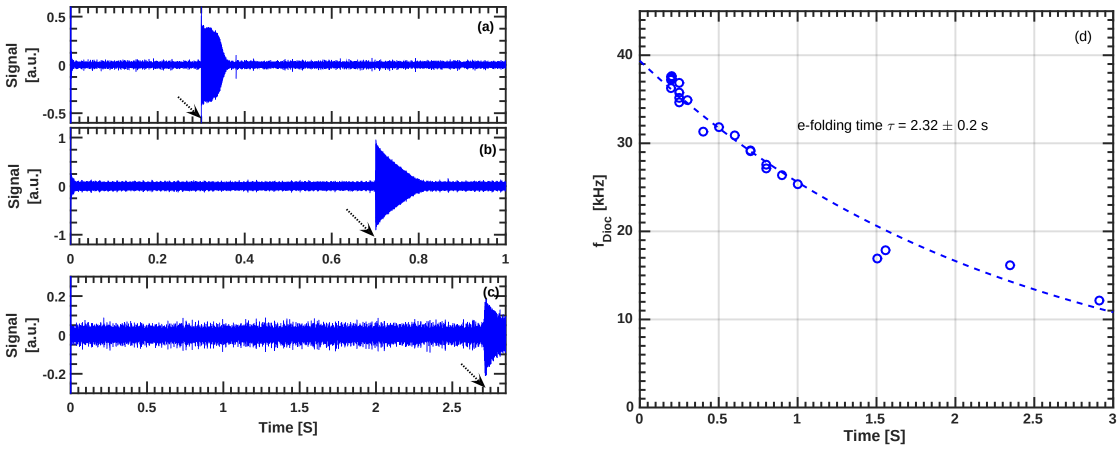

Figure 6.5: Time trace of capacitive probe oscillations after launching diocotron mode externally. Arrow indicates the time of diocotron launch at (a) 0.3 s (b) 0.7 s and (c) 2.7 s. (d) Observed diocotron mode frequency on capacitive probe along with exponential fit.

Following a linear theory, frequency of the launched $m = 1$ mode, is assumed to be related to the total charge(Q) trapped in the device [1]. This is well established for cylindrical traps [10, 163]. In absence of any established theory for toroidal diocotron modes, this theory has also been extended in recent times to large aspect ratio toroidal traps [64]. However its applicability especially in the limit of small aspect ratio merits discussion and due diligence. As observed in SMARTEX-C, the toroidal diocotron mode, with a trajectory evolving close to the inner wall in a small aspect ratio machine like SMARTEX-C, is highly non linear and coupled. It may be argued that the charge cloud, at least in case of small $E \times B$ excursions, does not experience the gradient in B and therefore can be explained within the ambit of linear theory. Another concern may be the aspect ratio dependent frequency shift in toroids as reported in simulation by Ha et. al [162]. But this shouldn't affect the diocotron mode frequency scaling with magnetic field as it would only result in a constant multiplier in the scaling. However, a shift in equilibrium position of the charge is ubiquitous in a small aspect ratio toroidal trap. Solution of Levy-Daugherty equation in toroidal geometries suggests such a shift [113] and the same has also been in earlier experiments by Purvi et al [55]. In fact, we find that its important to account for this shift if the mode frequency is to scale inversely with B field. In other words B has to be re-scaled appropriately accounting for the shifted plasma position. The shift has been established independently and quantified for different B fields in SMARTEX-C using inboard and outboard probes. At 380 Gauss the equilibrium positions is at 12.2 cm.

The frequency scaling with time, shown in Figure 6.5(d), gives us an estimate of the charge confinement. The e-folding time of the charge evolution, suggesting a confinement time, has been obtained through a linear least square fit to a natural log of the measured frequencies and error in confinement time is obtained from goodness of fit. An exponential decay is seen with a characteristic decay time of 2.32 ± 0.2 s. It may be remembered that this evolution is still in the presence of a drooping (12 %/s) toroidal magnetic field and adjustment for the same will only give us a larger estimate of decay time.

The improvement in confinement of electron plasmas in SMARTEX-C reported above, though not ultimate, is indicative of the fact that confinement in toroidal devices can run into seconds if instabilities can be adequately suppressed. The question therefore to ask at this stage is : *Can the confinement be extended indefinitely or is there a theoretical limit?* The scope in improvement of observed confinement, its scaling with magnetic field, existing theoretical limits of toroidal confinement and comparisons with experiments in SMARTEX-C are discussed in the next few sections.

6.1.1 Confinement "Limits" in Toroidal Devices

The confinement time-scales in SMARTEX-C reported in previous section needs to be assessed in the light of existing theories that caps the trapping time due to various transport mechanisms. It is particularly interesting to examine if transport results from one or more toroidal factors and is in any way augmented by the small aspect ratio of the trap. In this context, the Magnetic Pumping Transport (MPT) theory proposed by O'Neil et al [59] has been reviewed in somewhat detail and partly revised to compare with the results from SMARTEX-C.

MPT theory indicates that the toroidal curvature of the magnetic field, via electron-electron collisions drive the slow cross field transport of electron plasma [59] in a torus with purely toroidal magnetic field. For the assumed frequency ordering $\omega_{ce} \gg \omega_{bounce} \gg \omega_{E\times B} \gg \nu_{e-e} \gg \tau_{MPT}^{-1}$, the transport mechanism may be understood by considering a single flux-tube inside the toroidal electron plasma. As the plasma undergoes poloidal $E \times B$ drift (rotation due to self E-field) around the plasma center, the length of the flux tube as well as the magnetic field strength oscillates. Two adiabatic invariants $\mu = \frac{mv_\perp^2}{2B}$ and $J_\parallel = (2\pi)^{-1} \oint mv_\parallel dl$ demand the cyclic variations of $T_\parallel$ and $T_\perp$. This oscillating variation of the quantities being unequal due to $\tilde{v_\perp} \neq \tilde{v_\parallel}$ relaxation between the two causes the slow heating of the plasma. The transport is called magnetic pumping transport. Heating draws the energy from the electrostatic potential well and plasma radius expands.

Adiabatic invariants $J_\parallel$, $\mu_\perp$ and rate of energy transfer are related to the characteristic time scales, namely cyclotron frequency(ω_{ce}), parallel bounce frequency(ω_{bounce}), $E \times B$ time period($\omega_{E\times B}$) and electron-electron collision time period (ν_{e-e}). For SMARTEX-C, the frequency ordering is seen to satisfy $\omega_{ce} \gg \omega_{bounce} \gg \omega_{E\times B} \gg \nu_{e-e}$ with typical scales being 2.8 GHz $\gg$ 10 MHz $\gg$ 100 kHz $\gg$ 10 Hz (in time-scales 400 ps << 100 ns << 10 μs << 100 ms). Therefore, in spite of the strong toroidicity and existing gradients in B field, assumption of adiabatic invariance is still valid in SMARTEX-C and magnetic pumping transport may be considered as a distinct possibility. However, flux rates for transport as suggested by Crooks et al [59], has been proposed in the limit of large aspect ratio. In order to incorporate the effect of strong toroidicity the flux rate has been re-derived in the followed section 6.1.2) for arbitrary aspect ratio.

6.1.2 Magnetic Pumping Transport for Arbitrary Aspect Ratio Torus

Co-ordinate system chosen for the toroidal system (R,Φ,Z) and (r,θ) for the derivation is shown in the Figure 6.6. Flux tube with cross-section δA is also shown in the schematic.

Here I derive an expression for the radial particle flux by considering a single flux tube of plasma having length $L(r,\theta) = 2\pi R_o(r,\theta)$ or cross-sectional area δA, containing constant δN particles undergoing dominant motion of $E \times B$ drift with

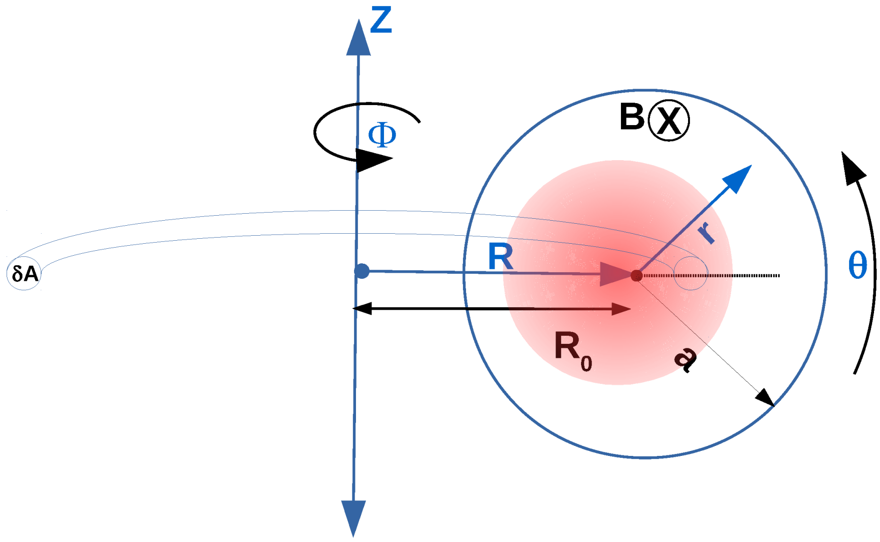

Figure 6.6: Schematic representation of flux tube in toroidal geometry of electron plasma where R, Φ and Z are the toroidal co-ordinates and r and θ are cylindrical co-ordinates.

a frequency of ω_E.

$$\omega_E = \frac{1}{4\pi\epsilon_o Br}\frac{\partial\Phi}{\partial r} \tag{6.1}$$

As the flux tube drifts towards the inside of the torus its length decreases and the magnetic field inside the flux tube increases, this can be expressed as,

$$L(t) = 2\pi R_o + 2\pi r cos(\omega_E t) \tag{6.2}$$

$$B(t) = \frac{B_o}{1 + (r/R_o)cos(\omega_E t)} \tag{6.3}$$

Conservation of first adiabatic invariant μ and second adiabatic invariant $J_{\parallel}$ leads to evolution of temperature,

$$\frac{\partial T_\perp}{\partial t} = \frac{1}{B}\frac{\partial B}{\partial t}T_\perp \tag{6.4}$$

$$\frac{\partial T_\parallel}{\partial t} = -\frac{2T_\parallel}{L}\frac{\partial L}{\partial t} \tag{6.5}$$

The parallel and perpendicular temperatures couple through collisionality so that full temperature evolution is more accurately described by

$$\frac{\partial T_\perp}{\partial t} = \frac{1}{B}\frac{\partial B}{\partial t}T_\perp - \nu_{\perp,\parallel}(T_\perp - T_\parallel) \tag{6.6}$$

$$\frac{\partial T_\parallel}{\partial t} = -\frac{2T_\parallel}{L}\frac{\partial L}{\partial t} + 2\nu_{\perp,\parallel}(T_\perp - T_\parallel) \tag{6.7}$$

where $\nu_{\perp,\parallel}$ is electron-electron collisional equi-partition rate. The factor of two difference in the collisional term reflects the fact that there are two perpendicular degrees of freedom and one parallel. Using Equations 6.2 and after some algebra this becomes,

$$\frac{\partial T_\perp}{\partial t} = \frac{\omega_E sin(\omega_E t)}{1+(\frac{r}{R_o})cos(\omega_E t)}(\frac{r}{R_o})T_\perp \tag{6.8}$$

$$\frac{\partial T_\parallel}{\partial t} = \frac{2\omega_E sin(\omega_E t)}{1+(\frac{r}{R_o})cos(\omega_E t)}(\frac{r}{R_o})T_\parallel \tag{6.9}$$

A two time scale analysis of these equations based on the frequency ordering $\omega_E \gg \nu$ yields the result

$$\frac{d[\frac{1}{2}\langle T_\parallel\rangle + \langle T_\perp\rangle]}{dt} = \frac{1}{2}T\nu_{\perp,\parallel}[(r/R_0)^2 + \frac{1}{2}(r/R_o)^4 + \ldots] \tag{6.10}$$

where $< \cdot >$ indicates an average over the fast time scale, that is, over a poloidal $E \times B$ drift time. The heating of the plasma arises because the parallel and perpendicular temperature fluctuations are unequal. Collisions cause a small phase shift in the fluctuations and there is a net heating in the plasma of second and higher even orders in r/R_o .

Since the confinement potentials are time independent, the total energy in the plasma is conserved and the increase in the thermal energy must be balanced by a corresponding decrease in the electrostatic energy. The particle flux is found by equating the increase in thermal energy to local Joule heating

$$n\frac{d}{dt}(\frac{1}{2}\langle T_\parallel\rangle + \langle T_\perp\rangle) = -e\frac{\partial \Phi}{\partial r}\Gamma_r \tag{6.11}$$

Where Γ_r is is the radial particle flux and n is the density. The right hand side of this equation is the Joule heating per unit volume. Above two equations 6.10

and 6.11 are solved for the flux and yield

$$\Gamma_{arb} = \frac{1}{2}\nu_{\perp,\parallel} n(r) \frac{2T}{-e\partial\Phi/\partial r}[(r/R_o)^2 + \frac{1}{2}(r/R_o)^4 + \ldots] \qquad (6.12)$$

This equation for particle flux depends on temperature, major radius as well as minor radius of the plasma, whereas the flux derived for large aspect ratio approximation contains inverse aspect ratio dependency, which cancels when transport time scale is obtained after dimensional analysis. The dependency of the particle flux with inverse aspect ratio is plotted in Figure 6.7 for both the cases and it's evident from graph that both the fluxes are equal in large aspect ratio approximation and gives rise to significant difference in flux when calculated for large inverse aspect ratios (i.e. small aspect ratio).

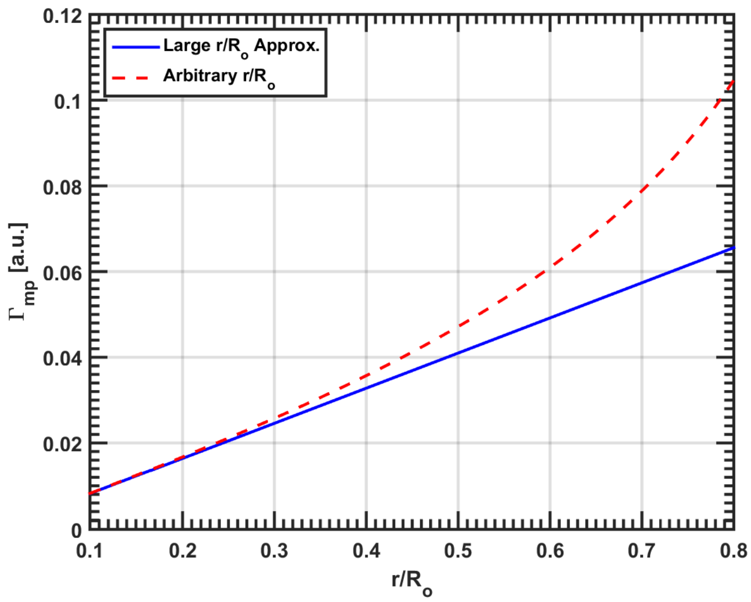

Figure 6.7: Magnetic pumping transport flux versus inverse aspect ratio for arbitrary aspect ratio MPT theory and large aspect ratio approximation.

6.1.3 Confinement time Limit set by Arbitrary Aspect Ratio

The transport time scale for arbitrary aspect ratio can be obtained by performing scaling (dimensional) analysis following Stoneking's procedure [60] by dividing particle inventory with surface integral of the flux equation as follows. The Γ_{arb}, so derived, is multiplied by the total surface area of the trap $(4\pi^2 rR_o)$ and $e\frac{\partial\Phi}{\partial r}$ is approximated as $\sim ner$ to arrive at the rate of particle loss. The total particle inventory is then divided by the particle loss rate to arrive at the confinement time scale τ_{arb}, given as,

$$\tau_{arb} = \frac{n_{av}2\pi^2 a^2 R_o}{\Gamma_r \pi^2 a R_o} \tag{6.13}$$

Here, n_{av} is volume averaged electron density, and using $\nu_{\parallel,\perp} \sim n/T^{3/2}$ and $\partial\Phi/\partial r \sim nea$, transport time scale can be written as

$$\tau_{arb} = 0.02[\frac{1}{R_0^2[\mathrm{cm}]} + \frac{2r^2}{(R_0[\mathrm{cm}])^4} + \ldots]^{-1}\sqrt{T_e[eV]} \tag{6.14}$$

This makes the transport time scale dependent on major radius, electron temperature and minor radius also. Contributions coming from minor radius to flux becomes significant at small aspect ratio and equation merges to Stoneking's formula for large aspect ratio approximation. τ_{arb}, which has a functional dependence on minor radius r, major radius R_0 and temperature T_e is plotted as a function of inverse aspect ratio (r/R_o) in Figure 6.8 for two different temperatures. Plasma radius r has been varied while R_0 is assumed to be 12.2 cm, as estimated from the inward shift of the plasma at 380 Gauss [48, 56]. A minimum plasma radius of 1.22 cm (maximum aspect ratio) suggests a confinement time of the order of 3 s, similar to that predicted by the large aspect ratio theory of O'Neil and Crook. However, in the limit of small aspect ratio, where the plasma radius is of the order of maximum allowable trap dimensions (7.2 cm), the confinement expected is of the order of 2.2 s for $T_e - 1$ eV.

In our experiments the plasma radius may well be in the range of 7.2 cm as discussed in Sec. 5.2.2 of Chapter 5. In that case, experimentally obtained e-folding time in SMARTEX-C $(2.32 \pm 0.2\,\mathrm{s})$, as reported in Sec 6.1 is therefore very close to the theoretically predicted time scale. However the effect of the droop in magnetic field leaves scope for debate and uncertainty. For a fair comparison with the theory therefore, the droop in B field had to be reduced and the lifetime more accurately ascertained.

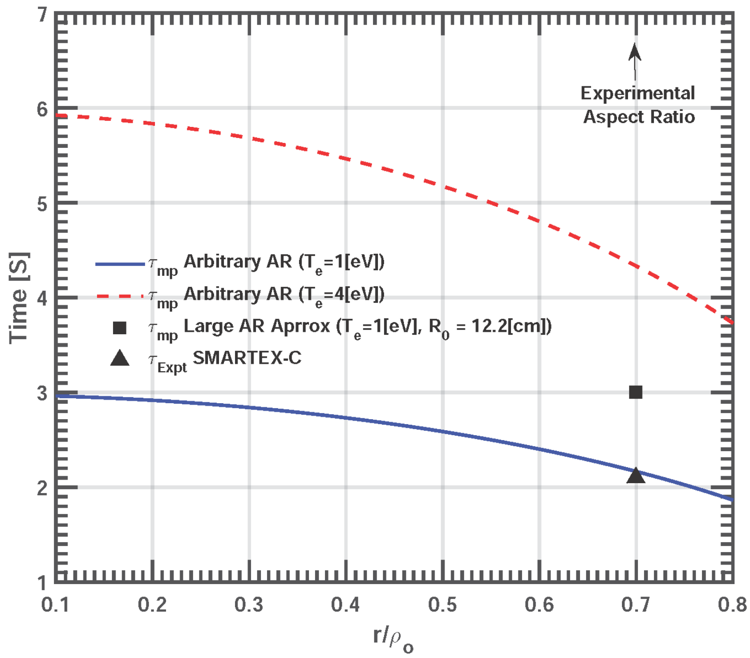

Figure 6.8: Magnetic pumping transport time scale versus inverse aspect ratio for arbitrary aspect ratio MPT theory for two different temperatures. Square symbol shows prediction made by large aspect ratio approximated theory and triangle experimentally observed confinement time.

6.2 Long Confinement Time Experiments

In order to ascertain the lifetime of electron plasma in SMARTEX-C more accurately, the TF coils were re-designed to overcome the existing droop. The product of current(I) and time period(τ) is a constant for the TF power supply and allows a range of magnetic fields with corresponding steady state duration. Experiments with a fairly constant ($< 5\%$) and average magnetic field of 9×10^2 Gauss for $\sim 2.4\,$s duration have been carried out successfully. For lower fields (~ 200 Gauss) the steady state is obviously longer and extends upto 60 s.

Experiments were repeated at steady state magnetic fields of 500 Gauss and the resulting capacitive probe oscillations are shown in Figure 6.9 (a) to (d) along with magnetic field pulse shown with dashed line in Figure 6.9(a). To avoid the intermediate corrections in drooping current during the TF coil pulse, integration time of the feedback circuit has been kept longer and hence the rise-time of the

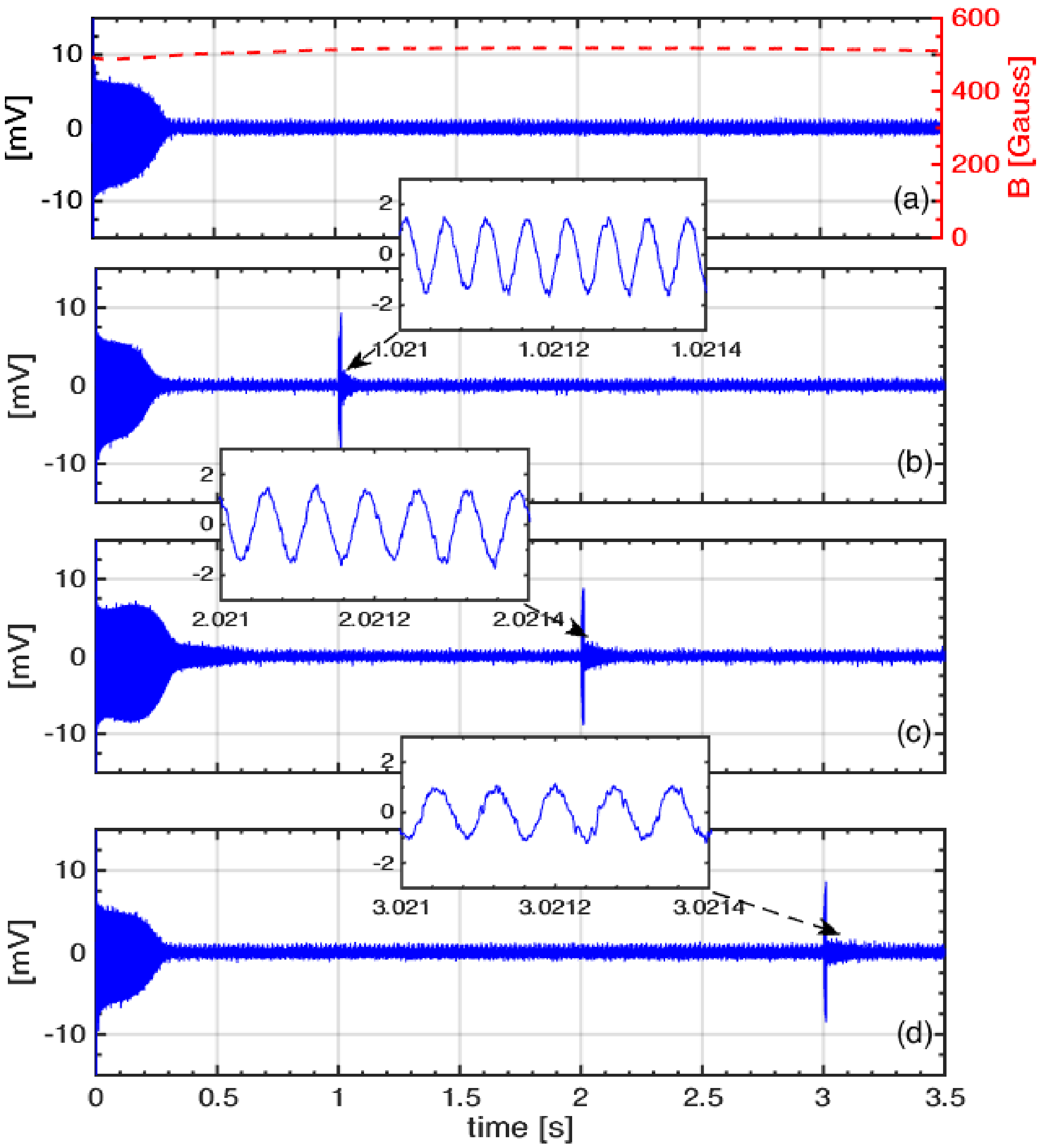

Figure 6.9: Time trace of capacitive probe oscillations (a) before launching and (b) after launching diocotron mode externally at (b) 1.02 s, (c) 2.02 s, and (d) 3.02 s for magnetic field of 525 Gauss.

B-field is slow for higher B-fields, this has resulted in uniform pulse for ~ 2.5 s at 9×10^2 Gauss and have a droop of $< 3\%$ at 500 Gauss.

Diocotron mode is externally launched as described before and is shown in the figure 6.9. Frequency of the linear $m = 1$ mode is utilised to obtain the total charge stored in the plasma at different instance of time. The e-folding time of the charge evolution is then obtained through a linear least square fit applied on natural log of f_D as explained in previous section 6.1. Multiple shots are acquired at each instant of time and error in confinement time is obtained from goodness of fit. The confinement time obtained at 500 Gauss magnetic field is $\sim 5.2 \pm 0.5$ s and at 9×10^2 Gauss is $\sim 6.2 \pm 0.7$ s at a pressure of $1.5 \pm 0.5 \times 10^{-8}$ mbar in trapping region.

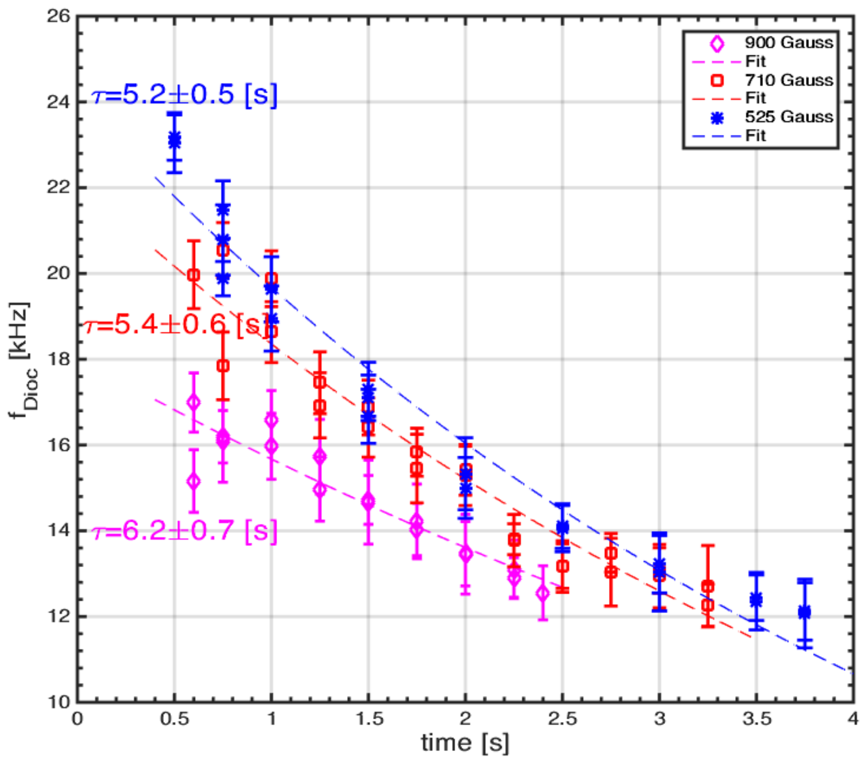

Figure 6.10: Observed dioctron mode frequency on capacitive probe along with exponential fit for different magnetic fields.

The confinement time, although showed marginal improvement ($\sim 5.2 - 6.2$ s), is interestingly, independent of B field. Currents are therefore lowered and experiments are conducted at reduced magnetic field of 100 and 200 Gauss. The droop in B field could therefore be further reduced to $< 0.1\%$. More importantly, due to less Joule heating of TF coils, the duration of B field could be increased to 40 s. Further, to push the limits of confinement, pressures in the trapping region were lowered by a factor of ~ 4 ($5.0 \pm 1.0 \times 10^{-9}$ mbar) by turning on the NEG pump. The significant improvement in confinement is visible from Fig. 6.11. At 100 Gauss the confinement time is 109.4 ± 9.3 s and at 200 Gauss it is 102.8 ± 18.9 s, with goodness of fit $\sim 95\%$. In addition to this being the highest confinement time with a purely toroidal B field, the independence of the lifetime with respect to B is being observed for the first time.

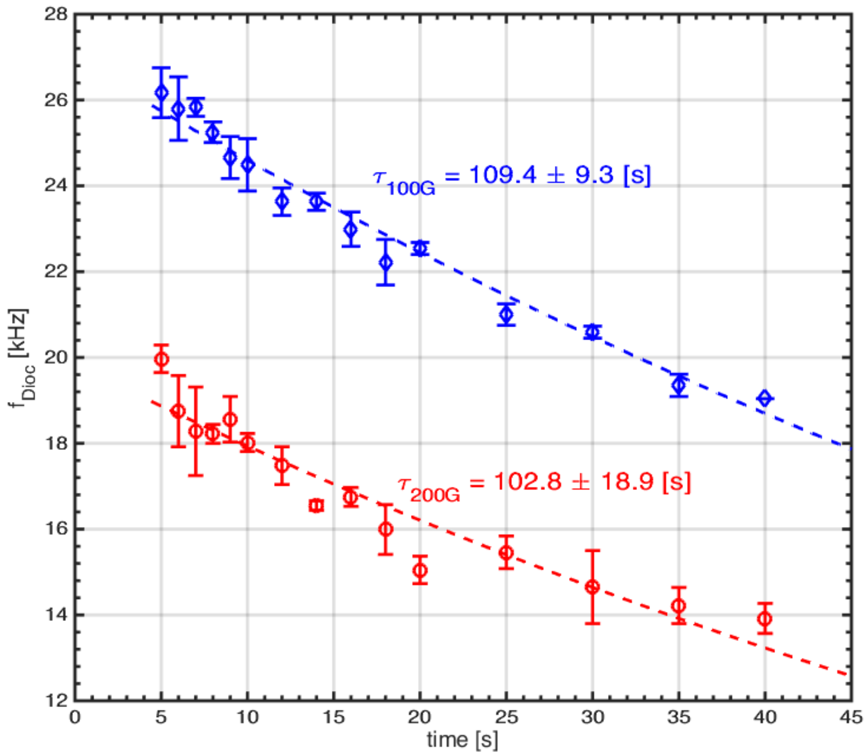

Figure 6.11: Confinement time for low magnetic field of 100 and 200 Gauss at 5.0×10^{-9} mbar pressure.

The difference in initial frequencies at different B fields merits discussion. Soon after injection, the frequency of the spontaneously triggered diocotron mode is observed to follow the $1/B$ scaling (see Figure 6.12), suggesting that initially injected charge is nearly same for all B fields. This has been shown for three reproducible discharges for both the magnetic fields. However, the damping of the mode and the rearrangement of the cloud that follows injection seem to be dependent on B field, involving different time scales. The charge left in the quiescent plasma is also different for different B fields. Admittedly, the dynamics and charge loss during the rearrangement is presently not well understood. However, after the initial dynamics, as the plasma becomes stable and quiescent, the loss of charge appears exponential in nature.

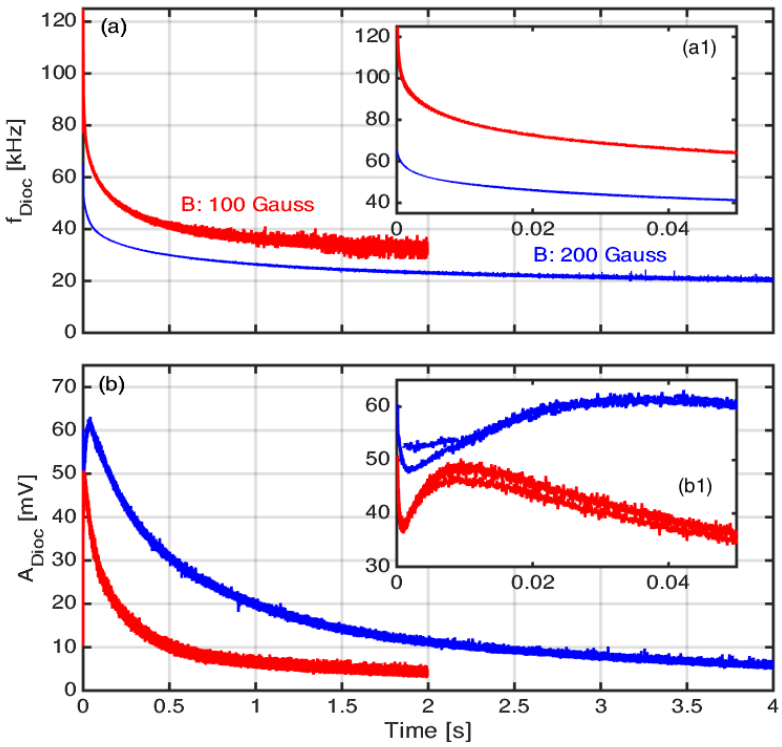

Figure 6.12: Frequency analysis of three plasma shots at 100 and 200 Gauss for (a) and (b) respectively. Inset plot (a1) and (b1) shows the zoom view for 50 ms.

In both cases the time scales evidently exceeds those predicted theoretically (2.2 s) presuming magnetic pumping transport. Herein, we are assuming the temperature to be of the order of 1 eV (The validity of such an assumption is discussed in the next Section). In other words, magnetic pumping transport do not seem to set an upper limit of confinement in SMARTEX-C as has been theoretically predicted for toroidal traps. Another interesting observation has been the in-dependency of confinement time of B field.

This suggests that the observed transport is probably due to magnetic pumping like transport. Other (but slightly unrelated) observation is the occurrence of an (injection induced diocotron modes [25,67]) linear diocotron mode that eventually damps, the damping time being proportional to the toroidal B field.

6.3 Conclusion and Discussion

With instabilities arrested, charge loss rate reduces and the confinement time extends to $100 \pm 10\,\mathrm{s}$ at B field 1×10^2&200 Gauss and operating pressure of $1.5 \pm 0.5 \times 10^{-9}$ mbar. This is estimated by launching a small amplitude diocotron mode and assuming, under certain approximations, that the frequency of the mode scales with total charge as suggested by the linearised theory of diocotron modes. The shift in equilibrium position of the electron plasma for a given B field can be taken into account while estimating total charge from the launched diocotron mode frequency. Estimation of lifetime however is unaffected by this shift as it only changes the multiplying factor of an exponential function. Confinement in such toroidal traps have been thought to be fundamentally limited by the magnetic pumping transport occurring in an in-homogeneous B field, that leads to gradual radial expansion of the plasma. However, rate of particle flux loss as proposed by O'Neil and Crook is in the large aspect ratio limit. The same has been re-derived for the arbitrary aspect ratio, suggesting a slightly lower limit of confinement in the regime of strong toroidicity. Observed confinement times in SMARTEX-C appear to surpass the theoretical estimates for a temperature assumed to be between 1 eV and 5 eV.

Observation of confinement time well beyond that predicted by MPT theory suggest that the transport presently observed in SMARTEX-C may not be due to magnetic pumping phenomena. However such an inference needs to be qualified. Theoretical confinement time τ as seen from Eq.(6.12) transport time scales are now dependent on minor radius r in addition to major radius R_o and electron temperature T_e and suggest an even lower limit of confinement. If the present transport is governed by MPT then what range of r and T_e would be possible?

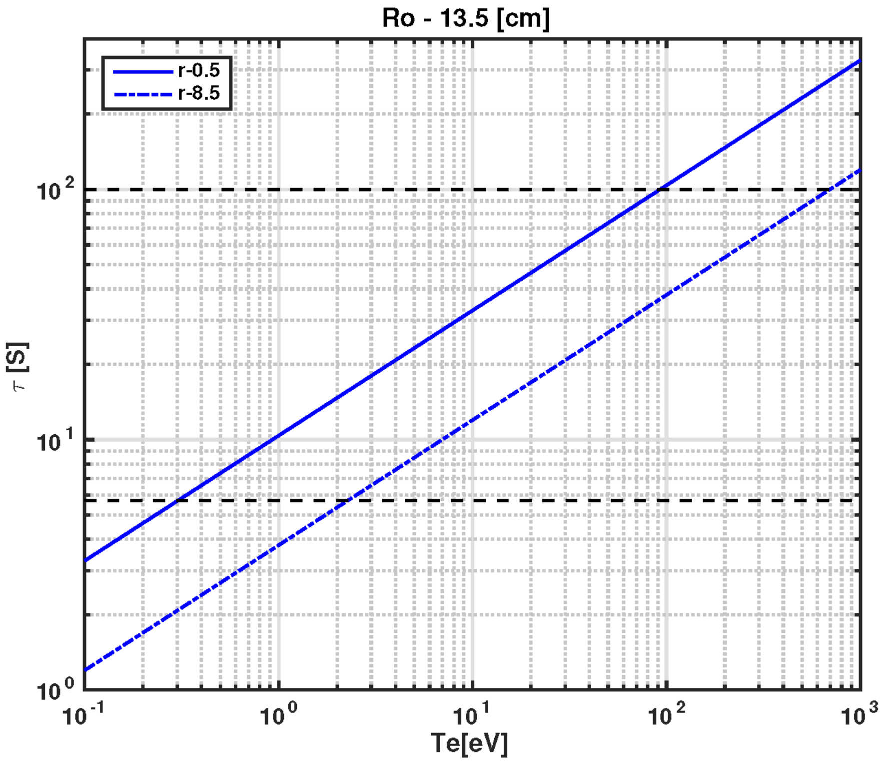

Figure 6.13: Limit of predicted confinement time by magnetic pumping transport theory as a function of temperature for different plasma radius.

In Fig 6.13 we have plotted the theoretically predicted lifetime for small aspect ratio traps (as derived by us in [122]) for two extreme plasma radius and electron temperatures (for a plasma located at minor axis $R_0 = 13.5\,\text{cm}$). Confinement time achieved at pressures 1.5×10^{-8} mbar and 2×10^{-9} mbar are also plotted as black dashed line. It suggests that, if confinement time (5.7 s) in SMARTEX-C were to be dictated by MPT, the temperature,(T_e) of the plasma would range between 2 to 3 eV for plasma radius (r) between 0.5 to 8.5 cm where the upper limit being the minor radius of the trap.

Although both temperature and radius of the plasma has not been accurately measured in SMARTEX-C, reasonable limits can be arrived at from our experiments. The r of the plasma has been earlier estimated to be $6.5 - 7\,\text{cm}$(Chapter 5 Section 5.3). Any measurement of T_e is challenging in such traps. However, pure confined electron plasmas are typically assumed to be one to few eV. In

SMARTEX-C, electrons may be initially accelerated in the trap with a parallel energy of 250 eV, but injection is soon cut off due to build up of space charge. Not surprisingly, plasma potential, measured with a high-impedance wire probe suggests a well-depth of not more than 40 eV. Charge collector also detects a measurable current only after the negative stopping potential is raised by a few 10's of volts, which preliminary estimates of temperature is $\sim 5 - 6$ eV (Chapter 3 Section 3.5). Though the measured temperature may be inaccurate due to conversion of potential energy to kinetic energy while plasma is dumped onto the grids, any correction would only reduce the temperature further. If we therefore assume the temperature T_e to be few eV, then all of these would suggest that at least at higher pressures 1.5×10^{-8} mbar confinement achieved in SMARTEX-C, is certainly close to those prescribed theoretically. However for lower pressures, as seen from Fig. 6.13, experimentally achieved confinement time of ~ 100 s would suggest a temperature of $90 - 700$ eV which is an impossible scenario for such confined electron plasmas. On the other hand, for few eV temperatures, as is typical for such plasmas, the unprecedented confinement time at lower pressures breaches the theoretical limits estimated from Eq. 6.14, fairly convincingly. However as can be seen from Figures 6.10 and 6.11, the confinement times are found to be independent of B-field, which is consistent with MPT predictions. It thus warrants a closer scrutiny of the transport time scales derived from MPT in Eq. 6.14.

In other words MPT does not seem to explain our present observations, importantly, hitherto MPT was presumed to limit confinement in toroidal traps. But our confinement times far exceeds it.

Herein one may contend that there is possibly a need to revisit the MPT theory in view of the peculiarities of a partial torus like SMARTEX-C. While the theory has been appropriately generalised for trap aspect ratio, there may be further scope of improvement. Basic mechanism underlying the magnetic pumping transport involves the rotation of the flux tube in a complete torus resulting in the fluctuation of $v_{\|}$ as it moves from inboard to outboard. In a partial torus, the additional end plugs results in the flux tube bouncing off non-uniform electric fields and this, some may contend, may result in additional fluctuations. In other words, the confinement times observed in SMARTEX-C should rather be compared with an appropriately modified theory and not the presently existing theories that apply for full torus.

We are also presently unable to answer the question as to what is the transport mechanism responsible for the observed confinement time in SMARTEX-C. Drawing from the experiments in cylindrical traps, electron-neutral collision driven transport at such low-pressures would predict very long confinement time. However, as stated above, rotational pumping transport [98] due to end-potential asymmetries may result in additional fluctuations in the flux tube and modify the transport time scales estimated from magnetic pumping transport. Also, just as in cylindrical traps transport attributed to trap assymetries [164, 165] that scales with magnetic field ($\sim B^2$) is a distinct possibility in SMARTEX-C arising due to fabrication errors, misaligned electrodes or magnets. Such transport also strongly depends on length as $\tau \propto L^{-2}$, and is presumed to be the reason for loss of confinement in large aspect ratio partial torus LNT-II [134].

Confinement time and its scaling with various experimental parameters, including trap aspect ratio are among the interesting aspects to be investigate in future. This would also throw more light on the kind of transport of charged particles that eventually affect the lifetime of the plasma in such partial torus.

7

Discussion and Future Scope

Experimental study of confinement and transport of electron plasma in tight aspect ratio partial toroidal trap, SMARTEX-C, has been carried out. The prime objective of identifying and removing the road-blocks towards long time confinement has been achieved and confinement time as long as $\sim$ 100 s has been obtained. This has allowed us to investigate the existing transport theories. All new and significant results obtained in thesis work are summarized below. Scope of future research work has been outlined and discussed in the following section.

7.1 Summary of Experimental Results

- In order to perform long-time confinement experiments transport driven by electron-neutral collisions should be minimized and hence trap has been upgraded to achieve better vacuum. Base pressure of $6.0 \pm 1.0 \times 10^{-10}$ mbar and operating pressure with filament 'ON' condition, vacuum of the order of $1.5 \pm 0.5 \times 10^{-9}$ mbar has been achieved. This has been achieved by addition of Cryo-pump which helped primarily in removal of water-vapor, Non-Evaporable Getter pump for removal of light gases such as H_2 and He, electro-polishing of the vacuum vessel, controlled baking of vacuum vessel and improving pumping port conductance. Magnetic field plays an important role in the confinement of electron plasma. Magnetic field strength of the system has also been upgraded. SMARTEX-C can be operated in B-field range of 200 Gauss to 1×10^3 Gauss, and pulse duration can be varied from 100 ms to 60 s. Trap components have been re-designed for minimum asymmetries in the mechanical arrangement to minimize the asymmetry induced transport. Spatial resolution of capacitive probes have been enhanced by reducing the size and quantity.

- Simple yet powerful way of interpreting the capacitive probe signal to ascertain the charge cloud dynamics has been developed. Expression for image current for point-like charge cloud making orbital motions has been derived using Green's reciprocation theorem. Numerical computation of signals for point charge trajectory has been carried out. It allows to infer the position of the charge cloud, shape and extent of the trajectory with the aid of capacitive probe signal and experimentally obtained total charge and velocity. Though the technique is presently rather heuristic, this has primarily helped us to establish that the dynamics of the trapped charges akin to an unstable diocotron mode. The technique if suitably extended presents us with an opportunity to investigate the vortex dynamics in SMARTEX-C in a non-destructive way.

- Instabilities are investigated and destabilizing mechanism has been identified in SMARTEX-C. Delineation from resistive wall instability and electron neutral collision driven instability has been carried out by comparing the growth rates. Destabilized electron plasma observed in SMARTEX-C is identified as transient ion resonance instability where ions are continuously formed due to electron impact ionisation and also leave the trap due to axial fields. Characterization of the instability onset time, growth rate, and peak diocotron mode amplitude have revealed many interesting features. Some of these are in good agreement with the theoretical predictions of transient ion resonance instability, while others represent classical ion resonance instability where ions are permanently trapped. Complete control over the observed instability has been achieved by tweaking the governing parameters and a very quiescent electron plasma in equilibrium has been obtained.

- To diagnose the quiescent electron plasma, externally launched diocotron waves have been used as a diagnostic tool. Capacitive probes are used as the launch electrodes and linear $m = 1$ mode is launched. As the linear $m = 1$ diocotron mode frequency is proportional to electron plasma density, the launched diocotron mode frequency gives the density of electron plasma. Technique has been perfected such that only small amplitude linear diocotron oscillations are launched. Launching of diocotron modes at different time instances give the temporal evolution of electron plasma density and this has been used to obtained the confinement time.

- Achievement of quiescent electron plasma at equilibrium has led towards the long-time confinement and provides an opportunity to investigate the transport properties of the electron plasma in the partial toroidal trap. Temporal evolution of electron plasma density is obtained using diocotron launch technique and time required to reach the $1/e^{th}$ of the initial electron plasma density is defined as confinement time. Confinement time has been scaled with magnetic field and is observed to be independent of B field.

- Observed confinement time has been compared with loss rate due to magnetic pumping transport for toroidal electron plasma. It may be noted that existing theory is applicable for large aspect ratio geometries. The theory of magnetic pumping transport has been generalised for arbitrary aspect ratio torus and new results predict even lower confinement time of electron plasma in SMARTEX-C (for an assumed temperature of 1 eV). Observed confinement time exceeds this theoretically predicted confinement time. In other words, present experimental results on confinement suggests that MPT does not really define the theoretical limit for confinement at least in partial toroidal traps.

7.2 Future Scope of Work

- Temperature Diagnostics : Plasma density and temperature are the fundamental parameters of any plasma that are necessary to characterize the plasma and also govern the collective properties. It is firmly believed that electrostatic potential energy is the dominant energy component in NNP and consequently kinetic energy of the plasma would be fairly low implying T_e to be few eV. Temperature diagnostics with good accuracy is very crucial in accurately defining the theoretical limit of confinement time and confirm the role of temperature in MPT and also for validation of the transport theory. Measurement of temperature $T_{\parallel}$ and $T_{\perp}$ will also establish the fact whether well trapped toroidal electron plasmas can approach thermal equilibrium like their cylindrical counterparts.

- Charge density profile measurement: To firmly establish the transport mechanism of partial toroidal trap like SMARTEX-C, it is important to obtain the temporal evolution of spatial density profile. One can design the vertical strips of charge collector or 2-D charge collector assembly behind the collector grid to obtain the line integrated radial density profile by dumping the charge cloud on these strips. The major concern could be the signal to noise ratio of the diagnostics as the total charge itself being very tenuous. Charge integrating capacitor or use of I to V converter with very high gain at high bandwidth might be a solution worth attempting. Imaging of entire poloidal cross-section of the trap with the help of phosphor screen aided by a Micro Channel Plate (MCP) would be the ideal solution, but it requires a careful design and suitable choice of phosphor material.

- Investigation of charge cloud/vortex dynamics: As discussed in Chapter 4, the single point-charge cloud trajectory is unable to explain the data from multiple capacitive probe. The amplitude as well as phase information for initial turbulent phase is left unexplained. This has been intuitively solved by taking two point charges and signatures consistent with multiple capacitive probes have been obtained. The analysis therefore needs to be extended to complex charge configurations. Further, including data from all the probes in our analysis can be of help to infer the complete dynamics and shall be validated in future using phosphor screen based imaging diagnostics. Formation of single vortex from hollow circular charge profile through turbulent inverse cascade is an interesting phenomena and can be understood using imaging diagnostics.

- Detailed characterization of Ion Resonance Instability : Clear signatures and trends of ion-resonance instabilities are observed and it has been shown in the Chapter 5 that the normalized peak growth rates follow the trend of transient ion resonance instability with many of the observed features in good agreement with theory. Some of the observed features (finite onset-time of instability) though are in agreement with that of classical ion-resonance instability. A threshold ion density appears to trigger the instability in accordance with the classical theory of ion-resonance. However, measurement of ion current (the ions leaving along the magnetic field to collector grid) shall confirm the amount of trapped/untrapped ions and define the threshold. Direct estimation of displacement 'D' either from capacitive probe data or from destructive charge collection diagnostics shall confirm the kind of growth of the instability (exponential/linear). Temperature diagnostics shall help in determining the electron impact ionization cross section with accuracy and identify whether temperature remains constant as pressure is varied and growth rates are estimated. Peak growth rate and its dependency on temperature, broadness of the resonance curve (Q-factor) with B-field are some of the important features that shall be further investigated.

- Toroidal arc length variation : It has been experimentally observed that partial toroidal traps are able to trap electron plasmas for confinement times longer than the ones predicted by magnetic pumping transport theory. Can the violation of theoretical prediction be due to the 'partial' nature of the trap? End grids can introduce the asymmetric electric fields at the edges and oscillate the electron plasma length. The length of the flux tube may also change significantly during poloidal rotation due to the small aspect ratio. All of this may trigger the rotational pumping transport. To establish the effect of end grids and confirm with the theory one can change the coarseness of the end grids or change the grid to rectangular hollow electrode and compare the observed confinement time with theory. In addition to this, to investigate the role of rotational pumping transport and observe the plasma length effects on confinement time, toroidal arc length can be varied and scaling of confinement time with toroidal arc length should be investigated. Experiments of confinement in full-torus with retractable filament shall also be of interest to investigate the MPT theory in full torus and role of trapped ions in complete torus on confinement of electron plasma.

- Aspect ratio variation : It is a well known fact that, cylindrical traps can confine the electron plasma for very long confinement time extending up to few days. To connect the physics of toroidal electron plasma to that of cylindrical trap, one can vary the aspect ratio of the trap by incrementally increasing the radius of inner-wall (or, alternately reducing the radius of outer-wall).

Homi Bhabha National Institute
Training School Complex, 2nd Floor, Anushaktinagar, Mumbai 400 094

Ref: HBNI/Ph.D./2015/ 1319. August 11th, 2015

Subject: Changes in Doctoral Committee of Shri Lavkesh T. Lachhvani (Enrolment No. PHYS06201404001), IPR, Gandhinagar.

The Competent Authority has approved the doctoral committee for Shri Lavkesh T. Lachhvani (Enrollment no.: PHYS06201404001) enrolled in the year 2014 under Physical Sciences Discipline at Institute of Plasma Research, Gandhinagar as under:

Name of the Student	**Doctoral Committee (*Chairman, +Guide)**
Shri Lavkesh T. Lachhvani (Enrollment no.: PHYS06201404001)	*Prof. Dhiraj Bora +Dr. Prabal Kumar Chattopadhyay Dr. Sudip Sengupta Dr. Joydeep Ghosh Dr. R. Ganesh **Dr. Sambaran Pahari - (Tech. Advisor)**

The Chairman of the Committee may intimate the student separately.

Lata B. 6/8/2015
(Smt. Lata B.)
A.O. - III

Dr. Subroto Mukherjee,
Dean-Academic,
Institute of Plasma Research,
Gandhinagar – 382 428

CC: Chairman and Guide of the student

Thesis Highlight

Name of the Student: Lavkesh T. Lachhvani

Name of the CI/OCC: Institute for Plasma Research **Enrolment No.: PHYS06201404001**

Thesis Title: Long-time Confinement of Toroidal Electron Plasma in SMARTEX-C

Discipline: Physical Sciences **Sub-Area of Discipline:** Plasma Physics

Date of viva voce: 14/01/2020

Nearly 100 sec confinement of electron plasma in a tight aspect ratio partial torus with a purely toroidal magnetic field is reported in this PhD thesis. This is nearly two orders higher than previously reported confinement time in similar devices elsewhere. Moreover, weak dependence of confinement on magnetic field, a distinguishing feature of Magnetic Pumping Transport, proposed theoretically is shown experimentally for the first time.

So far, it has been well-known that single component plasmas (a collection of pure electrons or ions), can simultaneously remain well-confined and be in thermodynamic equilibrium when trapped with a homogenous B field. Precise manipulation, control and reproducible experiments were therefore possible in linear traps which made such plasmas a potent tool for investigating a large number of basic phenomena, impacting a diverse range of fields such as fluid dynamics, condensed matter, astrophysics, atomic physics and antimatter-physics.

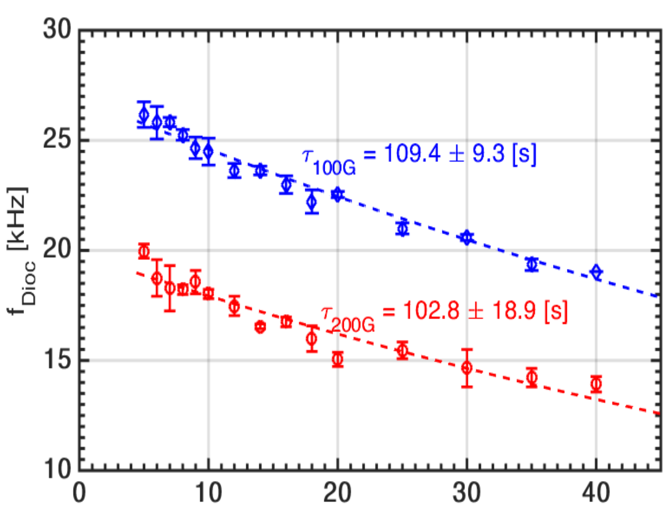

Figure 1 Observed diocotron mode frequency on capacitive probe along with exponential fit showing confinement time of 100 ± 10 s for low magnetic fields of 100 and 200 Gauss, at low pressure of 5.0 x 10^{-9} ± 1.0 x 10^{-9} mbar and injection energy VInj = 250 V.

Even though equilibrium and stability of charged clouds are theoretically ensured with a purely toroidal B field, confinement has remained, notoriously elusive. All efforts so far to tame a cloud of electrons in such traps, had resulted in a maximum life-time of 1-3 seconds. The challenges can be gauged from the fact that the last result was reported almost a decade ago. The biggest impediment, as has been suggested, is the magnetic pumping transport that is unavoidable due to the inhomogeneity in B field, though direct evidence of such transport had never been reported. In this context, the unprecedented confinement along with unmistakable evidence of magnetic pumping transport reported in this letter leads to interesting comparisons with existing transport theory and lifetime predicted thereof.

Such plasma in a tight aspect ratio device can become a test-bed for many fundamental studies such as, hydrodynamic behavior with compressible effects, transport of charged particles under arbitrary degree of neutrality in toroidal geometry (relevant to fusion community), formation of electron-positron pair plasmas of relevance to astrophysical community.